TECHNISCHE UNIVERSITÄT WIEN
Vienna | Austria

TU WIEN

MASTER THESIS

Oxygen nonstoichiometry in undoped and iron-doped strontium titanate

Author:

Emil **ELLMEYER**

Supervisors:

Dipl.-Ing. Alexander **VIERNSTEIN**

Univ.-Prof. Dipl.-Phys. Dr. Jürgen **FLEIG**

A thesis submitted in fulfilment of the requirements for the degree of Master of Science at the

Institute of Chemical Technologies and Analytics

Abstract

The aim of the present master thesis was to investigate the influence of UV irradiation on oxygen nonstoichiometry in undoped ($SrTiO_{3-\delta}$) and iron-doped ($SrTi_{0.98}Fe_{0.02}O_{3-\delta}$) strontium titanate. Moreover, the impact of changes in the oxygen content on materials' properties was examined. Due to their applicability in chemical sensors and solid oxide fuel cells (SOFCs), this mixed ionic and electronic conducting oxide material plays a crucial role in establishing emission-free technologies for power generation. Oxygen (non-) stoichiometry defines their ionic and electronic conductivity, since their defect concentration changes with the oxygen partial pressure $p(O_2)$, temperature and, as recently shown, with UV light illumination. In this thesis, three approaches have been chosen to quantify said effect of non-stoichiometry.

In the first part, the influence of UV light irradiation on the incorporation of oxygen into strontium titanate, and thus on the stoichiometric change of the material is discussed. Therefore, the in-plane conductivity and its change by UV light was investigated. The measurements were carried out in a temperature range from 340 to 410 °C and different atmospheres. The oxygen partial pressure ranged between 10^{-4} and 1 bar. In addition, the influence of different deposited ceramic top layers, such as yttria-stabilized zirconia and strontium-doped lanthanum chromite, on the UV-enhanced oxygen incorporation was examined.

The second part deals with strontium titanate thin film-based electrochemical cells, the so-called photoelectrochemical solid oxide cells (SOPEC), and the influence of UV light illumination on their open-circuit voltage. In such cells, UV light not only creates a photovoltaic, but also an electrochemical effect caused by the change in oxygen nonstoichiometry. Measurements of the open-circuit voltage were performed as a function of time and oxygen partial pressure while UV light was switched on and off. Characteristic photovoltaic and battery voltages whose magnitude is defined by measurement parameters (such as temperature and oxygen partial pressure) were quantified.

For the third main topic, $GaPO_4$ microbalances capable of detecting mass changes in the ng range were used to monitor directly the mass change of ceramic thin films during changes of the atmosphere and UV light illumination. Firstly, the measurement setup and the measurement parameters were optimized. Subsequently, the mass change of strontium-doped lanthanum cobaltate ($La_{0.6}Sr_{0.4}CoO_{3-\delta}$), undoped and iron-doped $SrTiO_3$ during $p(O_2)$ changes were examined. The impact of UV irradiation of iron-doped strontium titanate on the oxygen content could not be quantified yet and is subject to further investigations.

Kurzfassung

Das Ziel der vorliegenden Masterarbeit war, den Einfluss von UV –Licht auf die Sauerstoff-Nichtstöchiometrie und deren Auswirkung auf die elektrochemischen Eigenschaften von undotierten ($SrTiO_{3-\delta}$) und Fe-dotierten ($SrTi_{0.98}Fe_{0.02}O_{3-\delta}$) Strontiumtitanat zu untersuchen. Diese gemischtleitenden Oxide spielen aufgrund ihrer Anwendbarkeit in chemischen Sensoren und Festoxid-Brennstoffzellen (SOFC) eine entscheidende Rolle bei der Herstellung emissionsfreier Technologien zur Stromerzeugung. Die Sauerstoff-Stöchiometrie definiert dabei ihre ionische und elektronische Leitfähigkeit, da sich ihre Defektkonzentration mit dem Sauerstoffpartialdruck $p(O_2)$, der Temperatur und, wie kürzlich gezeigt, unter UV-Licht ändern. In dieser Arbeit wurden drei Ansätze gewählt, besagten Effekt der Nichtstöchiometrie zu beschreiben und zu quantifizieren.

Der erste Teil der Arbeit befasst sich mit dem Einfluss von UV-Belichtung auf den Einbau von Sauferstoff in Strontiumtitanat. Dieser wurde mit elektrochemischer Impedanzspektroskopie untersucht. Hierbei kamen Strontiumtitanat-Einkristalle zum Einsatz, deren Impedanz vor, während und nach UV-Lichtbestrahlung gemessen wurde. Die Messungen wurden in unterschiedlicher Atmosphäre durchgeführt, wobei der Sauerstoffpartialdruck zwischen 10^{-4} und 1 bar lag. Neben unbehandelten Einkristallen wurde zusätzlich der Einfluss von der beleuchteten Seite abgeschiedener Keramikdünnfilme, wie Yttrium-stabilisiertes Zirkonoxid und Strontium-dotiertes Lanthanchromit, auf den UV-gesteuerten, verstärkten Sauerstoffeinbau bei solchen Messungen untersucht.

Das zweite Hauptthema dieser Arbeit handelt von elektrochemischen Zellen auf Strontiumtitanat-Dünnschichtbasis, die sogenannten photoelektrochemischen Festoxidzellen (SOPEC), und der Einfluss der UV-Lichtbeleuchtung auf deren Leerlaufspannung. UV-Licht sorgt bei solchen Zellen nicht nur für einen photovoltaischen, sondern auch für einen elektrochemischen Effekt, der durch die Änderung der Sauerstoff-Nichtstöchiometrie hervorgerufen wird. Die Messungen der Leerlaufspannung wurden als Funktion der Zeit und des Sauerstoffpartialdrucks durchgeführt, während UV-Licht ein- und ausgeschaltet wurde. Dabei wurden charakteristische Spannungen gemessen, deren Größe durch Temperatur und Sauerstoffpartialdruck beeinflusst wurden.

Im dritten Teil wurden $GaPO_4$-Mikrowaagen, die imstande sind, Massenänderungen im ng-Bereich zu detektieren, herangezogen, um die Masseänderung keramischer Dünnschichter während Sauerstoffpartialdruckänderungen und UV-Beleuchtung zu überwachen. Zu Beginn wurden Messparameter (Druck, Temperatur und Gasstrom) und der Messaufbau optimiert. Es konnte dann für die untersuchten keramischen Dünnfilme die Änderung der Nichtstöchiometrie aufgrund der Änderung des Sauerstoffpartialdruckes bestimmt werden. Anschließend konnten Änderungen des Sauerstoffgehaltes in keramischen Dünnfilmen wie Strontium-dotiertes Lanthan-Cobaltat ($La_{0.6}Sr_{0.4}CoO_{3-\delta}$), undotierten und Eisen-dotierten Strotiumtitanat aufgrund der Änderung des Sauerstoffpartialdruckes bestimmt werden. Eine Massenzunahme von Eisen-dotierten Strontiumtitanat-Dünnschichten während einer Belichtung mit UV Licht konnte zum jetzigen Zeitpunkt nicht quantifiziert werden und wird weiter untersucht.

Abbreviations

Entity	Abbreviation	Unit
Gibb's Free Enthalpy	ΔG	$J\ mol^{-1}$
Configurational Entropy	ΔS	$J\ mol^{-1}$
Electrochemical Potential	$\tilde{\mu}_i$	J
Chemical Potential	μ_i	J
Electrostatical Potential	φ	J
Charge of the Species	z_i	-
Elementary Charge	e	C
Faraday Constant	F	$96485\ C\ mol^{-1}$
Flux	J_i	$cm^{-2}s^{-1}$
Electrical Conductivity	σ_i	$S\ cm^{-1}$
Concentration	c	$mol\ cm^{-3}$
Mobility	u	$cm^2\ V^{-1}s^{-1}$
Activation Energy	E_a	J
Boltzmann's Constant	k_B	$1.381 * 10^{-23}\ J\ K^{-1}$
Temperature	T, Temp.	$K, °C$
Pressure	p	bar
Oxygen Partial Pressure	$p(O_2)$	bar
Resistance	R	Ω
Distance, Width	d	mm, cm, m
Shear Modulus	G	Pa
Height	h	mm, cm, m
Area	A	cm^2, m^2
Resonance Frequency	f	Hz
Acoustic Velocity	v_{tr}	$cm\ s^{-1}$
Density	ρ	$g\ cm^{-3}$
Mass	m	g
Fermi Level	E_F	J
Conduction Level	E_C	J
Vacuum Level	E_{vac}	J
Valence Level	E_v	J
Density of States	N	J^{-1}
Strontium Titanate	STO	-
Iron-doped Strontium Titanate	Fe:STO	-
Strontium Lanthanum Cobaltate	LSC	-
Lanthanum Strontium Chromite	LSCr	
Yttria-stabilized Zirconia	YSZ	-
(Oxygen) Nonstoichiometry	δ	-

Contents

1. Introduction

The ever-growing demand of electrical energy sheds a light onto technologies, which have not reached up to their full potential. Finding new ways to establish renewable, emission-free energy technologies is one of the major issues to replace conventional fossil energy sources. These new energy forms are required to provide energy almost independently from natural fluctuations, like weather, day of time, or else, with strong emphasis on reduction of CO_2 and particulates emission, as well as sustainability in terms nature and costs.

Over the last few decades, increased efforts have been made in the field of solid oxide, ceramic semiconducting energy converters. Photovoltaic cells [1] and solid oxide fuel cells (SOFC) [2] are just two of many examples of bearer of hope for new technologies. With growing scientific interest in these kinds of materials, it has become more important to gain a detailed knowledge of reaction mechanisms, kinetics of stoichiometry change, and interface phenomena.

For this purpose, perovskite-type oxides have been studied heavily in the last few decades, because of their chemical versatility. Due to the applicability in many fields of energy conversion systems, such as permeation membranes [3], oxygen conversion [4], high temperature oxygen sensors [5], *strontium titanate* (undoped $SrTiO_3$ (STO) and doped $Sr(Fe_xTi_{1-x})O_{3-\delta}$ (Fe:STO, FSTO)) is one of the few examples for which defect chemistry is understood in great detail [6-8]. It has become particularly interesting for its feature to be both electronic and ionic conducting, depending on the conditions. As example of so-called mixed ionic and electronic conductors (MIECs) [9, 10] strontium titanates exhibit an oxygen partial pressure ($p(O_2)$) and temperature dependent stoichiometry. Certain compositions can be realized, by annealing specimens under defined conditions. Subsequently the desired status can be frozen in by rapid quenching [7]. The adjusted stoichiometry determines the way of conducting [11]. The chemical reaction, which determines these electrical properties, is the oxygen exchange reaction at the surface [12].

Oxygen incorporation and release is a principal example of the stoichiometric change in an ionic material and thereby its internal chemistry [6]. Brouwer diagrams [11] are widely used in the field of defect chemistry because they heuristically relate defect concentration, and thereby conductivity, to oxygen partial pressure. Solid-state oxides equilibrate with the surrounding atmosphere at sufficiently high temperature. The oxygen content in the surrounding atmosphere plays a major role in the oxygen exchange reaction. Determining the electric properties, changes of about 10 ppm (i.e. $p(O_2)$ change from 10^{-25} to 10^{-5} bar at 800 °C) may transform $SrTiO_3$ from a good conductor into a poor electronic conductor [6, 13].

However, changing the oxygen partial pressure of the surrounding atmosphere is not the only possibility to modulate the oxygen content of strontium titanates. UV light illumination also leads to a change in the oxygen exchange kinetics of such materials [14, 15]. In this context different phenomena could be observed from photochromism [16] and trapping of holes to exhibiting battery-like voltages when embedded in a photoelectrochemical cell [17, 18] as a thin film, which arouses increasing interest for applications involving solar energy.

To gain better understanding of reaction mechanisms and kinetics of oxygen incorporation under UV light, three different approaches were chosen: The influence of UV light illumination on the conductivity of STO

single crystals, on the open-circuit voltage of STO-based photoelectrochemical cells and on the mass of the ceramic material.

As illustrated by the Brouwer diagram, the impact of oxygen nonstoichiometry can be exemplified by the change of conductivity of the ceramic material [11]. This can be achieved by investigating the influence of the illumination of UV light on the oxygen nonstoichiometry of pristine STO single crystals and such with PLD-deposited ceramic thin films on top. The stoichiometry change is monitored *via* in-plane impedance measurements. The influence of UV light on the in-plane conductivity is derived from the change of impedance during UV light illumination. Apart from that, the influence of different ceramic thin films during such measurements is investigated.

The second major topic of this thesis are STO thin film-based electrochemical cells, the so-called solid oxide photoelectrochemical cells (SOPEC) [17], and the influence of UV light illumination on the open circuit voltage. While until now only SOPECs based on STO single crystals with applied YSZ layers have been investigated in research [17, 18], cells consisting of YSZ single crystals and STO-based thin films are investigated in this thesis. The measurements were carried out as function of time and $p(O_2)$, before, during and after UV light illumination.

The aim of the third topic was to ascertain if it is feasible to monitor mass changes due to oxygen stoichiometry changes caused by change of atmosphere and UV light illumination. $GaPO_4$ microbalances are high-temperature piezoelectric materials [19], whose resonance frequencies exhibit a certain relation to their mass [20]. By depositing STO-based thin films onto said microbalances and measuring the resonance frequency as function of oxygen partial pressure and temperature, mass changes in the range of ng can be detected. Schröder, Fritze *et al*. [21] used langasite microbalances to weigh oxygen stoichiometry changes in praseodymium-cerium oxide films. The $GaPO_4$ experiments were conducted as an analogous approach.

2. Theoretical Framework

2.1. Solid state and defect chemistry of strontium titanate and iron-doped strontium titanate

In contrast to liquids and amorphous materials, crystalline materials are defined by their highly ordered structures. Based on the works of Bravais in the 1840s [22], it was shown that in a three dimensional Euclidian geometry the possibilities of arranging points in symmetrical way sum up to fourteen Bravais lattices. These mathematical lattices provide the basis for the seven crystal systems, which are defined by the length of their base vectors and interaxial angles.

Real crystals deviate from the ideal and possess defects. These defects are classified by their dimension:

- Zero-dimensional defects – point defects
- One-dimensional (linear) defects – dislocations
- Two-dimensional (planar) defects – external and internal surfaces
- Three-dimensional (volume) defects – point defect clusters, voids, precipitates

In ionic solids, the point defects are the *decisive* species enabling mass transport and they are reactive acid-base and redox-active centers [11].

2.1.1. Point defects and departures from stoichiometry

Before explaining the classes of point defects in detail, the nomenclature of choice in defect chemistry is the Kröger-Vink notation [23]. In contrast to the standard chemical nomenclature, it has the advantage to precisely describe crystallographic defects, exemplified by

$$M_S^C$$

M denotes the species, which can either be an atom or ion (e.g. Ti, Fe, …), an unoccupied lattice site (also vacancy V or v), an electron (e) or an electron hole (h). The subscript S describes the location of the species M, whether showing the chemical symbol of the normal occupant of the site or i in case of an interstitial. The superscript C is the charge relative to that the same site would have in an ideal structure. It can be either negative ($'$), neutral (x), or positive ($\bullet$).

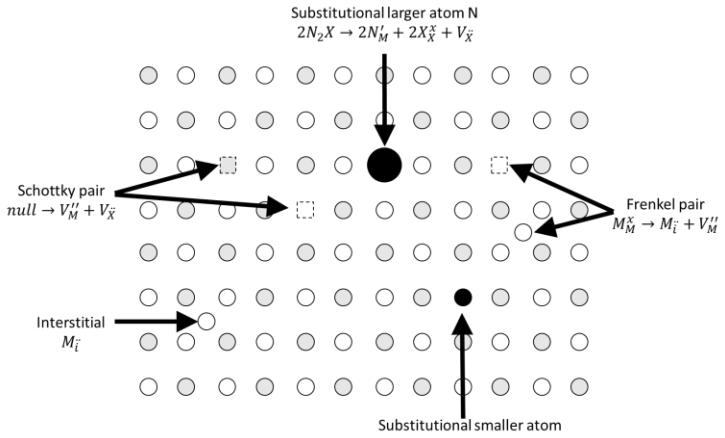

Figure 2.1-1 Hypothetical lattice of an MX crystal to illustrate typical point defects in a lattice: intrinsic (Frenkel, Schottky) and extrinsic defects (substitutional atoms) are shown.

Point defects are subdivided in intrinsic and extrinsic defects. Intrinsic defects are a basic property of a pure crystal. Extrinsic defects are caused by impurities and dopants. Figure 2.1-1 displays the lattice of a hypothetical MX crystal to illustrate point defects in crystal structures. [24]

2.1.1.1. Intrinsic defects

A perfect crystal contains no point, linear or planar imperfections and can only if at all exist at a temperature of 0 K. The concentration of defects increases at higher temperatures to reduce Gibb's free energy ΔG, according to Equation (1).

$$\Delta G = \Delta H - T\Delta S \quad (1)$$

While the creation of a defect requires a certain amount of energy ΔH, the configurational entropy ΔS increases, due to the increasing number of positions a defect can occupy (ΔS decreases at the same time with increasing defect concentration). Hence, the formation of defects can be energetically favored in total. Figure 2.1-1 displays the two most common intrinsic defects in ionic crystals, the Frenkel defect and the Schottky defect, with the example of a hypothetical crystal $M^{2+}X^{2-}$ (Figure 2.1-1).

- Frenkel defect: atom or ion displaced from lattice site to an interstitial position, resulting in a defect pair, consisting of an interstitial site and a vacancy site, $M_M^x \rightarrow M_i^{\bullet\bullet} + V_M''$
- Schottky defect: oppositely charged ions leave lattice sites, creating vacancies, $null \rightarrow V_M'' + V_X^{\bullet\bullet}$

2.1.1.2. Extrinsic defects

In doped ceramics, the effect of intrinsic defects is often negligible compared to their extrinsic counterparts. These extrinsic defects are either impurities, which are mainly undesired, or dopants, which are usually purposefully added. Dopants are categorized in two classes characterized by their electronic contribution:

- **Acceptor dopants**: Ions of *lower* valence relative to host-lattice cations, resulting in a *negative* charge, as when small amounts of Al_2O_3 are incorporated into TiO_2, so that the Al^{3+} ion substitutes for Ti^{4+} as Al_{Ti}'. Charge neutrality is achieved by generation of electron holes $h^{\bullet}$, cation interstitials $M_i^{\bullet\bullet}$ or anion vacancies $V_X^{\bullet\bullet}$.
- **Donor dopants**: Ions of *higher* valence than that of the parent ions, as when small amounts of Nb_2O_5 are incorporated into $SrTiO_3$. This results in an effective *positive* charge, $Nb_{Ti}^{\bullet}$, Nb^{5+} replacing Ti^{4+}, and the introduction of counterbalancing electrons e' into the structure, as well as cation vacancies V_M'' or anion interstitials X_i''.

2.1.1.3. Intrinsic and extrinsic semiconductors

An intrinsic semiconductor is a pure semiconductor with a negligibly small amount of impurities/dopant species present. Thus, the number of excited electrons n and the number of holes p are equal: $n = p = n_i$ and $pn = n_i^2$ (mass-action law).

The number of electrons (occupied conduction-band levels) n is given by the total number of states N(E) multiplied by the occupancy F(E), integrated over the conduction band,

$$n = \int_{E_C}^{\infty} N(E)F(E)dE \quad (2)$$

The density of states N(E) equals the number of states per energy interval. In the case of free electrons in a Fermi gas,

$$N(E) \propto \sqrt{E} \tag{3}$$

which is known as parabolic dispersion. The occupancy is represented by the Fermi-Dirac distribution function

$$F(E) = \frac{1}{1 + \exp\left[\frac{E - E_F}{k_B T}\right]} \tag{4}$$

Figure 2.1-2 depicts energy diagrams of different kinds of semiconductors. When a semiconductor is doped with donor or acceptor impurities (extrinsic), impurity energy levels are introduced that usually lie within the energy gap. A donor impurity has a donor level (N_D in Figure 2.1-2(b)), which is defined as being neutral if filled by an electron, and positive if empty. Semiconductors with donor-doping are referred to as n-type. Conversely, an acceptor level (N_A in Figure 2.1-2(c)) is neutral if empty and negative if filled by an electron. These semiconductors are p-type. In other words, for n-type doping, there are more electrons available in the conduction band, while for p-type dopants, the electron hole concentration in the valence band gets larger. As a result, electric properties like conductivity, are altered considerably.

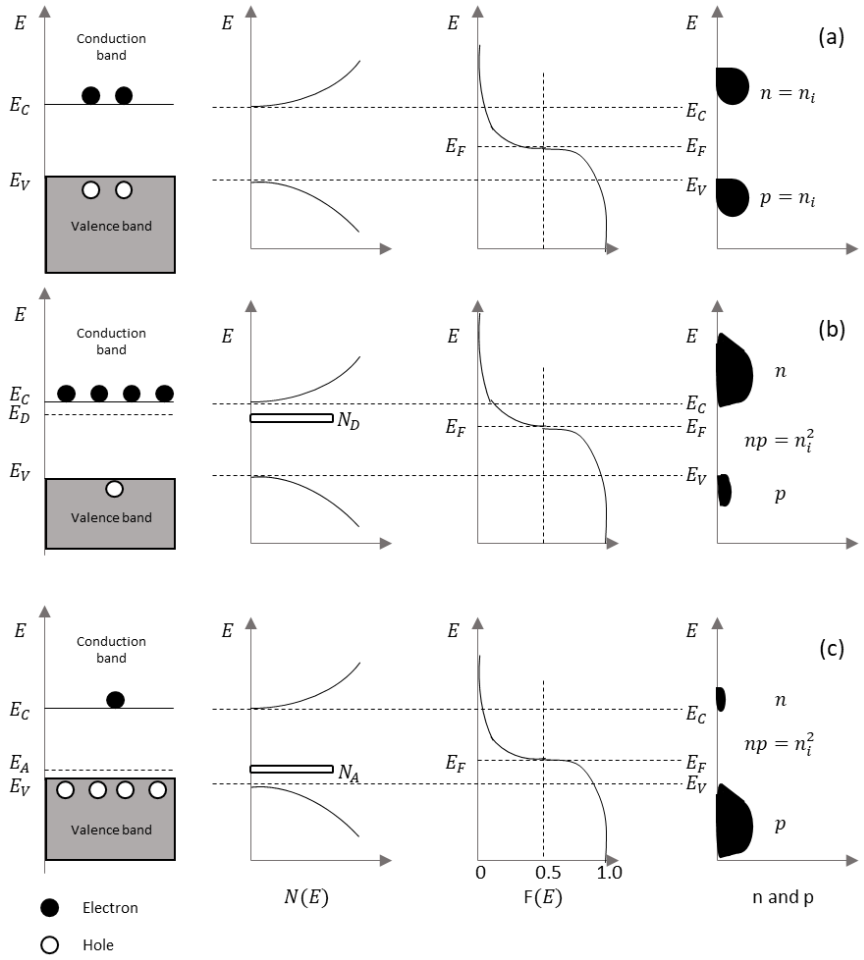

Figure 2.1-2 Schematic band diagram, density of states, Fermi-Dirac distribution, and carrier concentrations for (a) intrinsic, (b) n-type, and (c) p-type semiconductors at thermal equilibrium.[25]

2.1.1.4. *Oxygen nonstoichiometry*

Oxygen nonstoichiometry is a principal example of stoichiometric change in an electroceramic and thus its electric behavior. Solid-state oxides equilibrate with the surrounding atmosphere at sufficiently high temperature (e.g. for STO [26]). The oxygen content in the surrounding atmosphere plays a crucial role in the oxygen exchange reaction.

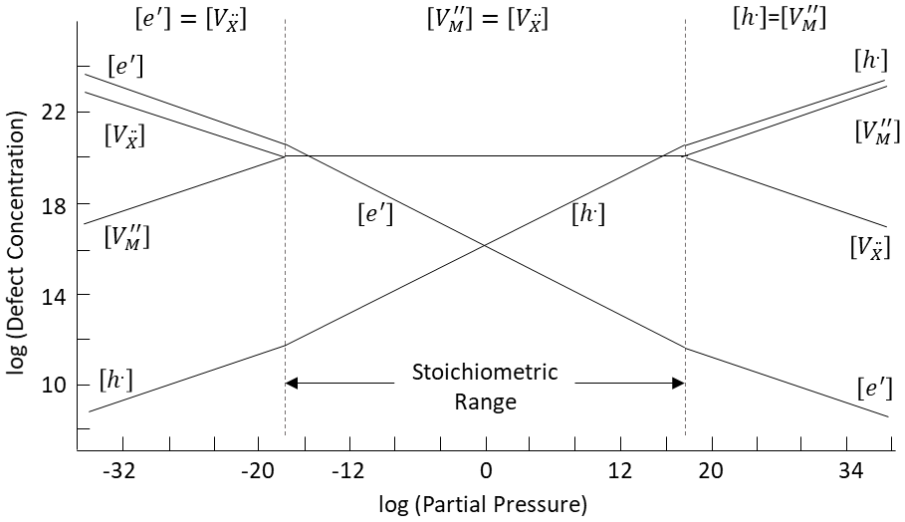

Figure 2.1-3 Brouwer diagram of an ionic ceramic MX with ionic defects. [11]

The Brouwer diagram [11], see Figure 2.1-3, is the graphical representation of the defect concentration, thus charge carrier concentration, as function of the oxygen partial pressure p(O_2). In STO, the Brouwer diagram is divided into three regimes (from low to high p(O_2)): Starting with n-type conductivity and e^- as major charge carriers. Raising the p(O_2), ionic conductivity due to oxygen vacancies becomes determining. Subsequently, the electron holes are the major charge carrier. The stoichiometric range, where the major charge carrier is (oxygen) vacancies, and the two nonstoichiometric ranges, where the major charge carrier is electrons e', at low oxygen partial pressures, and holes $h^\bullet$, at high oxygen partial pressures[7].

The oxygen exchange reaction is a multistep process including the adsorption of molecular oxygen, electron transfer, O-O bond dissociation and incorporation into and release by the lattice by consuming and creating vacancies[27]. This can be broken down to Equations (5), (6) and (7). Equations (5) and (6) are the overall reaction for incorporation into the lattice, Equation (7) represents the release.

$$\frac{1}{2}O_2 + V_O^{\bullet\bullet} + 2e' \leftrightarrow O_O^x \quad (5)$$

$$\frac{1}{2}O_2 + V_O^{\bullet\bullet} \leftrightarrow O_O^x + 2h^\bullet \quad (6)$$

$$O_O^x \leftrightarrow \frac{1}{2}O_2(g) + V_O^{\bullet\bullet} + 2e' \quad (7)$$

Oxygen exchange reaction therefore can determine the electrical behavior of a ceramic, like STO or Fe:STO.

2.1.1.5. *Influence of UV light on oxygen exchange*

Oxygen nonstoichiometry is not only dependent on the oxygen partial pressure of the surrounding atmosphere and temperature, but it can also be heavily influenced by light illumination of sufficient energy in the range of UV light, since its energy is large enough ($E_{light} > E_{bandgap}$) to excite electrons from the valence into the conduction band, according to

$$nil + h\nu \rightarrow e^- + h^\bullet \quad (8)$$

This attributes to the acceleration of oxygen incorporation due to more available electrons to partake in the reaction from Equations (5) – (7). Thus, the generation of additional holes in the UV illuminated zone according to Equation (8) occurs. This typically eventuates in enhanced conductivity [27, 28], electrochemical altering [17] or photocoloration [15, 29].

2.1.2. Crystal structure and defect chemistry in perovskites ABO_3

As explained before, the oxygen exchange reaction is an important example of the stoichiometric change of an ionic material that also typically occurs in perovskite-type materials. Strontium titanate is often used as an electroceramic model material to investigate this reaction [6, 12, 15]. In the course of this study, thin films and single crystals of strontium titanate $SrTiO_3$ (STO), iron-doped strontium titanate $SrFe_xTi_{1-x}O_3$ (Fe:STO) and lanthanum strontium cobaltate $La_{0.6}Sr_{0.4}CoO_3$ (LSC) were investigated. Apart from that, A-site strontium-doped lanthanum chromite ($La_{0.9}Sr_{0.1}CoO_3$ (LSCr10) and $La_{0.8}Sr_{0.2}CoO_3$ (LSCr20)) were used. These crystalize in the perovskite-type structure ABO_3, see Figure 2.1-4.

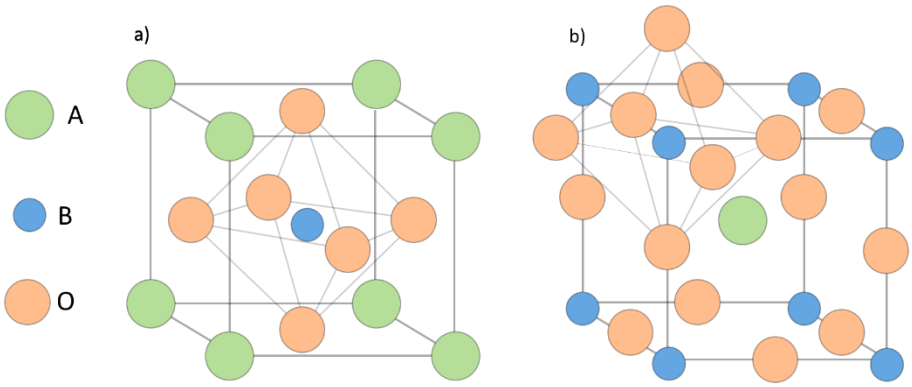

Figure 2.1-4 Two representations of a cubic perovskite showing either the B- (a)) or A-centered (b)) unit cell.

Perovskite-type materials come in a great variety of cations with multiple combinations and strongly varying electrical and mechanical properties. The general formula of perovskite is ABO_3, where A is a larger cation than B, with a combined valence of +6. In STO, the B site is occupied by Ti^{4+} and the A site is occupied by Sr^{2+}. It is a semiconductor with a band gap energy of 3.2 – 3.4 eV [30, 31]. Due to impurities consisting of acceptor-doping material, nominally undoped STO is hole conducting in most cases[13, 32].

Doping of a pure perovskite leads to an occupation of different cations of the same crystallographic site. In the case of Fe-doped STO, the $SrTiO_3$ is doped with Fe-cations as quasi solid solution. The substitution of Ti^{4+} with a Fe^{3+} cation causes a shortage of positive charge, which in Kröger Vink notation can be expressed as a negative charge relative to the $SrTiO_3$ structure, $Fe_{Ti}^{'}$[8, 12]. This is compensated by either an oxygen vacancy or a hole in the valence band. However, Fe^{3+} can also trap a hole, leading to a neutral B-site cation (Fe_{Ti}^{x}) without further counter charge. Formulas (9), (10) and (11) denote the conservation conditions.

$$[Fe]_{tot} = [Fe'_{Ti}] + [Fe^x_{Ti}] \quad (9)$$

$$2[V_O^{\bullet\bullet}] + [h^\bullet] = [Fe'_{Ti}] + [e'] \quad (10)$$

$$2[V_O^{\bullet\bullet}] \approx [Fe'_{Ti}] \quad (11)$$

Contrarily to that, Fe^{2+} counts as an electron ($Fe_{Fe}^{'}$), when it occupies the A-site. This typically does not occur in single crystals.

In the case of $La_{0.6}Sr_{0.4}CoO_{3-\delta}$, Sr^{2+} ions are occupying regular lanthanum lattice sites (A), with $Sr_{La}^{'}$ being the defects with negative effective charge. To maintain electroneutrality, both tetravalent cobalt ions $Co_{Co}^{\bullet}$ and $V_O^{\bullet\bullet}$ are formed. With increasing temperature, $V_O^{\bullet\bullet}$ are formed in the account of $[Co_{Co}^{\bullet}]$ according to [33].

$$[Co_{Co}^{\bullet}] + 2[V_O^{\bullet\bullet}] = [Sr_{La}'] \quad (12)$$

$$2Co_{Co}^{\bullet} + O_O^x = 2Co_{Co}^x + V_O^{\bullet\bullet} + \frac{1}{2}O_2(g) \quad (13)$$

2.1.3. Mass and charge transport and in-plane conductivity

The electrochemical potential $\tilde{\mu}_i$ of a particle i consists of a chemical term, the chemical potential μ_i, and an electrical term, the electrostatical potential φ times the charge number z_i times the elementary charge e, see Formula (14). $\tilde{\mu}_i$ remains constant as long as the thermodynamic equilibrium is maintained.

$$\tilde{\mu}_i = \mu_i + z_i e\varphi \quad (14)$$

Deviations from this equilibrium lead to a particle flux J_i, which is proportional to the resulting gradient in $\tilde{\mu}_i$. The resulting transport equation (15):

$$J_i = -\frac{\sigma_i}{z_i^2 e^2}\nabla\tilde{\mu}_i \quad (15)$$

The electrical conductivity σ_i is proportional to the concentration c_i and mobility u_i of the charge carrier.

$$\sigma_i = |z_i| e c_i u_i \quad (16)$$

Equations (14), (15) and (16) account for both electronic (electrons and holes) and ionic defects (vacancies and interstitials). Considering all the contributions of conductivity, the resulting total conductivity sums up to:

$$\sigma_{tot} = \sum_k \sigma_k = \sigma_{cation} + \sigma_{anion} + \sigma_{electron} + \sigma_{holes} \quad (17)$$

The formula (18) depicts the temperature dependence of the conductivity, an Arrhenius-type relation,

$$\sigma = \sigma_0 \exp\left(-\frac{E_a}{k_B T}\right) \quad (18)$$

2.1.3.1. In-plane conductivity measurements

In the experiments from Section 4.1., the in-plane conductivity of an STO single crystal sample is determined before, during and after UV illumination. The penetrating UV light generates electron-hole pairs in STO, see Formula (5), thereby altering the material electrochemically. Figuratively, the UV light is charging the cell like a battery by incorporation/release of oxygen into/out of STO under/after UV and thus by changing the defect concentrations, as in Formulas (5) – (7). This leads to enhanced incorporation of oxygen into or release of oxygen out of the material. Thus, the conductivity is increased by the elevated charge carrier concentration in the sample and oxygen incorporation induced electron hole formation. This is the main reason for the retarded relaxation of the sample's conductivity after turning the UV light off. Apart from the described effects, heating of the sample might also contribute to the conductivity increase.

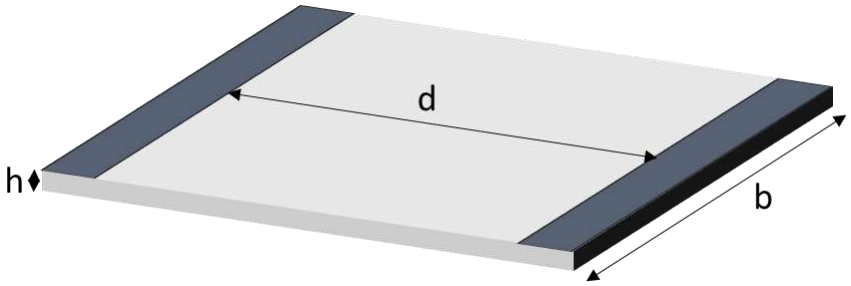

Figure 2.1-5 Dimensions of the single crystal to calculate the in-plane conductivity. d is the stripe distance, h is the height, b is the width

To investigate electrical properties of electroceramics, electrochemical impedance spectroscopy (EIS) is the method of choice. Principally, a small AC potential is applied to an electrochemical cell, and its current response, the frequency-dependent AC resistance, to this perturbation is measured. The in-plane conductivity of single crystals is derived from the obtained AC resistance R according to formula (19). For the sake of simplicity, the two dimensionality of the current flow between the two stripe electrodes is neglected and the conductivity is simply calculated from the stripe distance d, the width b and the sample thickness h, see (19).

$$\sigma_{inplane} = \frac{1}{R}\frac{d}{bh} = \frac{1}{R}\frac{d}{A} \tag{19}$$

For the measured impedance spectra, equivalent circuits consisting of R|CPE proved to be the most suitable for fitting, as depicted in Figure 2.1-6.

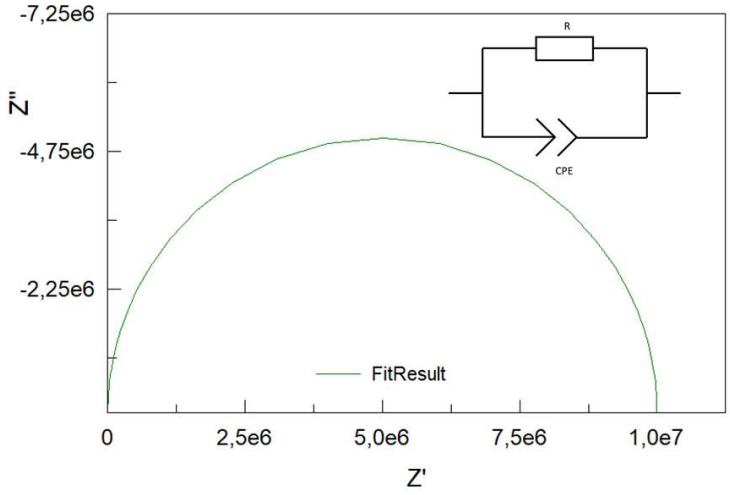

Figure 2.1-6 Fit result of the simulation of a R|CPE circuit, using the "Z view" software. This circuit proved to be most suitable for fitting the measured impedance spectra to obtain the resistance.

This method is used for the investigated STO single crystal samples of Section 4.1.

2.2. The solid oxide photoelectrochemical cell

2.2.1. Principle

Solid oxide photoelectrochemical cells (SOPECs) are a combination of an oxide-based high temperature solar cell and a solid oxide electrochemical cell. UV light illumination triggers two different types of responses, a photovoltaic and an electrochemical, which have an influence on the total measured voltage [17, 18].

The investigated SOPECs of this study consist of a yttria-stabilized zirconia (YSZ) single crystal as a base and electrolyte, (Fe:)STO-based thin films and Pt or Au current collectors, compare Section 4.2. Varying the current collector material changes the properties (work function, electrostatics) of the metal|MIEC interface, which has an influence on the voltage change upon irradiation with UV light.

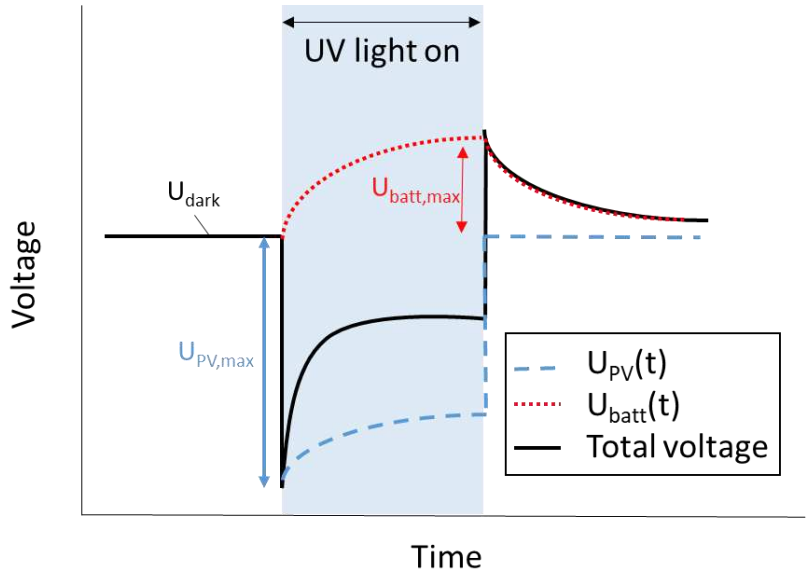

Figure 2.2-1 Typical open circuit measurement curve U(t) of SOPECs during UV light illumination in oxygen-rich atmospheres. The total voltage changes due to enhanced oxygen incorporation into the cell and the resulting oxygen concentration gradient. From this curve, the characteristic voltages, the battery voltage U_{batt} and the photovoltaic voltage U_{PV}, are obtained.

Open circuit measurements of SOPECs lead to typical measurement curves, as displayed in Figure 2.2-1. The dark voltage U_{dark} denotes constant voltage under constant measurement conditions of the (equilibrated) sample. Its value varies with oxygen partial pressure $p(O_2)$ of the surrounding atmosphere and temperature.

The illumination with UV light causes two different distinguished effects: the photovoltaic and the battery-type effect. In Figure 2.2-4, the process of the UV light illumination of an SOPEC is illustrated.

2.2.2. The photovoltage

The generation of DC electricity from light of sufficient energy in the UV range is called the photovoltaic (PV) effect [34, 35]. When light is absorbed, charge carriers (e.g. electrons) are excited to a higher-energy state, but contained in the material. This, in combination with band bending, produces a separation of charges, which results in a voltage. This is often attributed to p-n junctions (semiconductor boundaries

and interfaces see Figure 2.2-2), but it also happens at most semiconductor|metal interfaces, depending on the difference in the work functions and the Fermi level (Schottky junction, Figure 2.2-3).

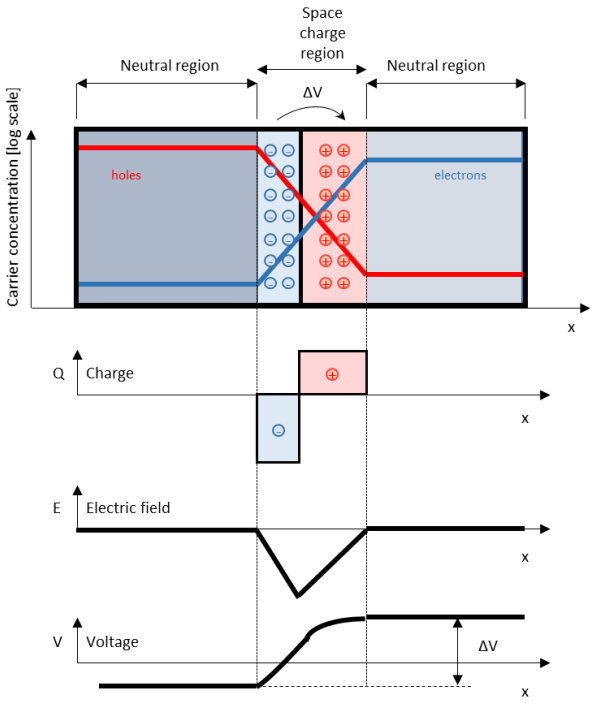

Figure 2.2-2 A p–n junction in thermal equilibrium with zero-bias voltage applied. Under the junction, plots for the charge density, the electric field, and the voltage are depicted.

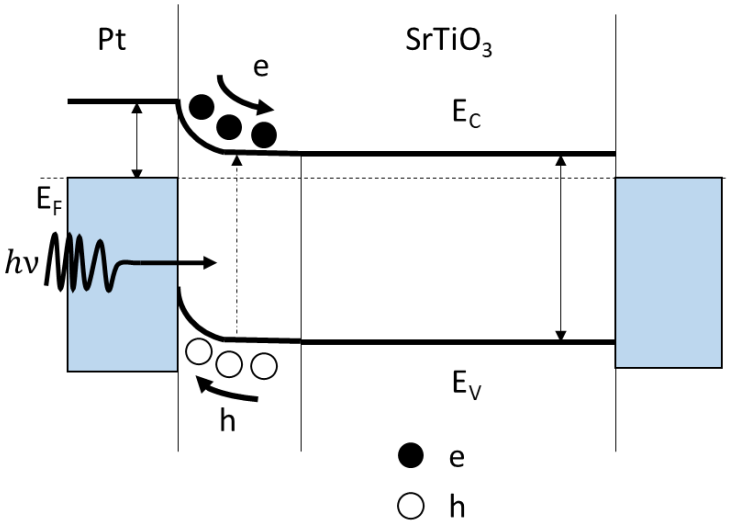

Figure 2.2-3 Schematic band structure of a Pt/STO/Al heterojunction, a Schottky barrier. Source [35] investigated a solar cell consisting of an STO single crystal with two different current collectors (Pt and Al). SOPECs exhibit PV effects similar to this one.

Thus, the measured photovoltage U_{PV} originates from an electrostatic potential step, a Schottky barrier (special case of p-n junction), see Figure 2.2-3, and band bending, between the current collector Au or Pt and the thin film (Fe:)STO. The penetration of UV light into the sample causes the generation electron-hole pairs, see Formula (8), thereby modifying this space charge separated by the space charge region.

$$nil + h\nu \rightarrow e' + h^{\bullet} \qquad (8)$$

As a result, the Fermi level is split into two quasi Fermi levels [36] and the minority charge carrier concentration changes. Thus, a potential difference develops between the grid current collector and the porous counter electrode.

The photovoltaic voltage U_{PV} is determined from the distance between the most negative point in the UV curve and the dark voltage, see Figure 2.2-1. As indicated, it is time-dependent due to the chemical altering during UV light illumination and found shortly after switching on UV light.

The photovoltaic contribution to the total voltage is challenging to quantify, but dependent on oxygen partial pressure, temperature and above all on space charge effects of the thin film. U_{PV} is also time-dependent, because the UV illumination alters the charge carrier concentration, thereby changing the composition, the Fermi level and consequently the U_{PV}.

2.2.3. The battery effect

The battery voltage U_{batt} is the result of the penetrating UV light altering the SOPEC, more specifically the thin film, electrochemically. Figuratively, the UV light is charging the cell like a battery by

incorporation/release of oxygen into/out of STO under/after UV and thus by changing the defect concentrations. The UV light causes a generation of electron-hole pairs, see (8). As a result, the oxygen incorporation reaction into the thin film becomes strongly accelerated, because more conduction band electrons are participating in the rate-determining reaction step. Oxygen is incorporated according to

$$\frac{1}{2}O_2 + V_O^{\bullet\bullet} + 2e' \rightarrow O_O^x \qquad (6)$$

This generates a stoichiometry change, which affects the whole thin film and results in an observable Nernst-type voltage between the two sides of the cell. Accordingly, this battery-type contribution to the voltage is determined by the change of the oxygen concentration in the thin film, under UV light and the oxygen electrochemical potential at the counter electrode, which is still in equilibrium with the surrounding gas.

Thus, U_{batt} is obtained short after the UV light is turned off. It is the difference between the most positive (or negative) point in the U(t) curve and the dark voltage, see Figure 2.2-1. The sign and magnitude of the battery voltage is dependent on oxygen partial pressure and temperature. It raises with UV illumination time, reaching a maximum, $U_{batt,max}$, after a certain time.

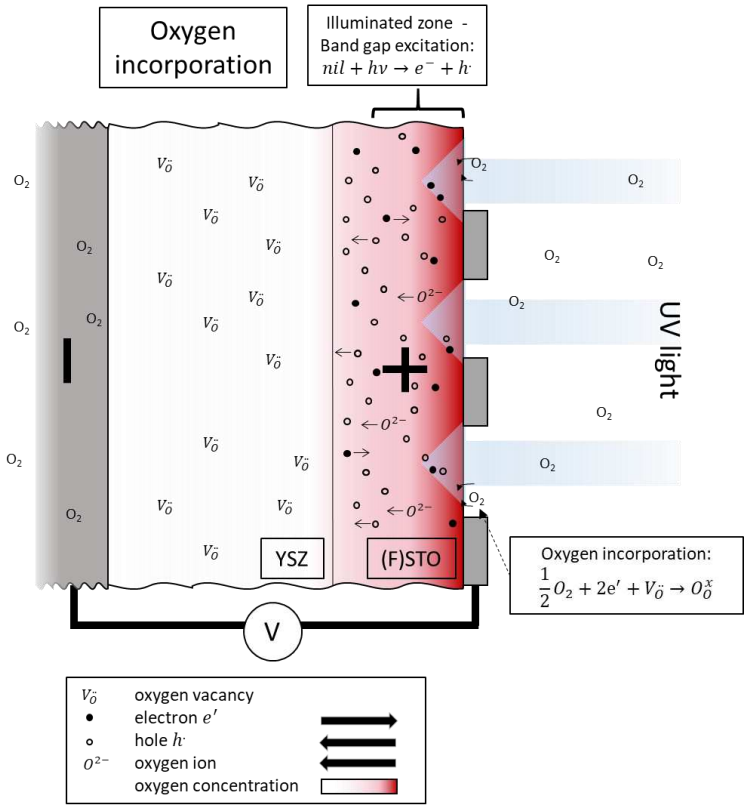

Figure 2.2-4 Schematic illustration of the process of UV light illumination of a SOPEC sample during measurement and enhanced oxygen incorporation. The resulting oxygen concentration gradient leads to a build-up of voltage. The + and – denote the oxygen content, which causes the build-up of U_{batt}.

2.2.4. The dark voltage

When the light is turned off, the cell releases the excess oxygen again and after an equilibration time, the measured voltage becomes U_{dark} again.

2.3. $GaPO_4$ microbalances

In 1880, Pierre and Jacques Curie observed a physical phenomenon when they applied mechanical stress onto the surface of various crystals and thereby generating a potential difference across two surfaces of the crystal. The discovered proportionality of polarization to the strain was the definition of piezoelectricity. One year later, 1881, Gabriel Lippmann discovered the converse effect: applied potential difference leads to mechanical strain. This allows probing an acoustic resonance by electrical means, and thus relating of a resonance frequency to the mass of the material [37].

The first conventionally used piezoelectric material of choice for monitoring mass change was the quartz crystal microbalance (QCM). This kind of microbalance is eponymous for the whole group of microbalance materials ($GaPO_4$, langasites, …). While α-quartz crystals were formerly used because of their superior mechanical stability and piezoelectric properties, their major drawback is their restriction to applications below 300 °C. The preferred microbalance material for temperatures above 300 °C thin film monitoring applications is gallium orthophosphate, $GaPO_4$ [19, 38].

2.3.1. Principle

Electrochemical Quartz Crystal Microbalance (EQCM) devices derive from piezoelectric quartz crystal resonators that resonate electromechanically in a thickness shear mode (TSM). As piezoelectric material, it is predestined to function as device to monitor mass changes in nanogram range.

When applying an alternating current to a properly cut crystal of a piezoelectric material (in the case of the used $GaPO_4$, the Y-11° cut), the induced oscillations generate a standing shear wave. This condition is established when the acoustic wavelength is twice the combined thickness of the crystal and electrodes. Therefore, the resonance frequency f_0 of the microbalance prior to the mass change can be related to the thickness of the crystal d_q (index q for the crystal) by the following equation (20):

$$f_0 = \frac{v_{tr}}{2d_q} = \frac{N}{d_q} \tag{20}$$

With the frequency constant $N = \frac{v_{tr}}{2}$. This relation requires that the thickness of the electrodes is relatively small compared to the microbalance to have identical velocities in the electrodes and crystal. The acoustic velocity depends on the shear modulus and the density of the crystal ($v_{tr} = \sqrt{\frac{G}{\rho}}$ in isotropic media).

Considering that the thickness d is obtained by $d_q = \frac{m}{A\rho}$ and combining this with formula (20), it arises that the resonance frequency is linked with the mass

$$f_0 = \frac{N}{d_q} = \frac{NA\rho}{m} \tag{21}$$

Therefore, an increase in the thin film thickness $\frac{\Delta d}{d}$ leads to a change in the resonance frequency in form of $-\frac{\Delta f}{f_0}$. Considering formula (21) a change of the mass of the deposited layer leads to the same shift of the frequency, according to (22).

$$\frac{\Delta f}{f_0} = -\frac{\Delta d}{d} = -\frac{\Delta m_q}{\rho_q A d} = -\frac{\Delta m}{\rho_q A d} \tag{22}$$

In 1959, Sauerbrey described the correlation between measured change of frequency and the area density $\varphi = \frac{\Delta m}{A}$ by the following equation (23):

$$\Delta f = -\frac{f_0 \varphi}{d_q \rho_q} = -\frac{f_0^2}{N \rho_q} \varphi = -C_f \varphi \tag{23}$$

More commonly, the elastic mass change per unit of the piezoelectrically active area, Δm, is considered (24):

$$\Delta f = -C_f \Delta m \tag{24}$$

where C_f is the sensitivity factor, a characteristic constant of the used microbalance and given by (25)

$$C_f = \frac{2 f_0^2}{(\mu_q \rho_q)^{\frac{1}{2}}} \tag{25}$$

The mode of oscillation and other elastic properties are determined by the cut angle with respect to crystal orientation. The Y-11° cut of the $GaPO_4$ sensor, as used in this thesis, displays a 100 times smaller temperature sensitivity than the conventional and commonly used AT-cut quartz crystals [39-41].

2.3.2. Measurement of the resonance frequency

The resonance frequency of the microbalances is measured by a Gamry resonator. A microbalance behaves as a circuit composed of an inductor, capacitors, and resistor (RLC circuit) in series with a precise resonance frequency in an oscillator [37], as seen in Figure 2.3-1.

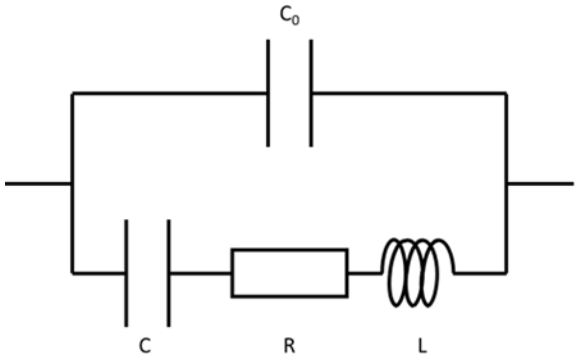

Figure 2.3-1 Equivalent circuit of a microbalance during resonance frequency measurement.

An RLC circuit forms a harmonic oscillator for current, and resonates in a similar way as an LC circuit. The most important property of which is its ability to resonate at a specific frequency, the resonance frequency f_0, which is conveniently related to the angular frequency ω_0, according to

$$\omega_0 = 2\pi f_0 = \frac{1}{\sqrt{LC}} \tag{26}$$

Resonance occurs because energy for this situation is stored in two different ways: in an electric field as the capacitor is charged and in a magnetic field as current flows through the inductor. The resonance frequency is defined as the frequency at which the impedance of the circuit is at a minimum. However, this only accounts for undamped oscillations. Introducing the resistor, making it an RLC circuit, causes the decay of these oscillations, which is also known as damping. The resistor also reduces the peak resonance frequency. In ordinary conditions, some resistance is unavoidable even if a resistor is not specifically included as a component; an ideal, pure LC circuit exists only in the domain of superconductivity.

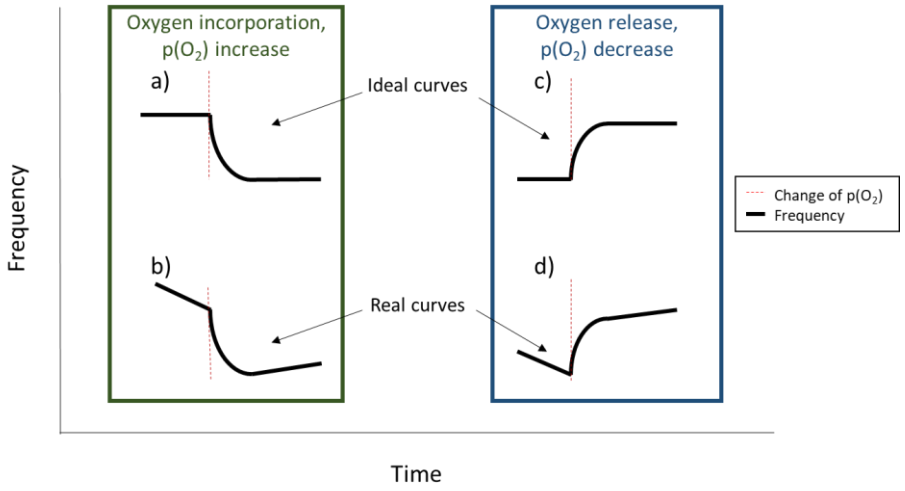

Figure 2.3-2 Illustration of typical resonance frequency measurements. The cases for oxygen incorporation and release, as well as ideal and real curves are illustrated.

Figure 2.3-2 sketches schematically the typical course of the resonance frequency over time in a gas exchange experiment. The curves a) and b) on the left denote an ideal change of the gas atmosphere from low oxygen partial pressure to higher with an associated oxygen incorporation causing a mass increase and consequently a shift of the resonance frequency as described above. The two curves c) and d) on the right denote oxygen release due to decreasing oxygen partial pressure. Thus, the mass decreases and the resonance frequency increases. The real curves b) and d) display the usual shape of the curves during an experiment. They deviate from the ideal curves a) and c) mainly due to the frequency drift.

The frequency drift denotes a change of frequency over time with no change of external parameters. The frequency in-/decreases under constant conditions depending on experimental temperature, flow and chemical nature of the surrounding atmosphere. It is stated in the unit of ppm Hz s^{-1}. Frequency drifts in the range from 50 to 1000 ppm Hz s^{-1} are common and often pose a problem in the interpretation of the mass change.

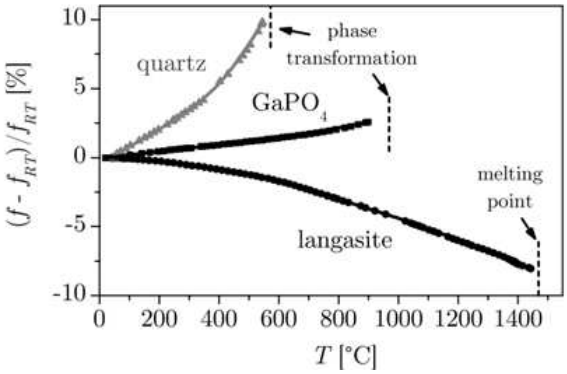

Figure 2.3-3 Temperature-dependency of different conventional microbalance materials. At temperatures under 850 °C, the $GaPO_4$ microbalances exhibit the least resonance frequency drift. [19]

The temperature-dependency of the resonance frequency is illustrated in Figure 2.3-3. It is well illustrated that $GaPO_4$ microbalances exhibit superior temperature properties compared to other conventional microbalances in at temperatures of 300 to 850 °C [38]. From Figure 2.3-3, it is also apparent that the temperature is a major reason for the frequency drift.

2.3.3. Determination of oxygen nonstoichiometry δ

During an oxygen exchange reaction, oxygen is either released from or incorporated into the ceramic material, thereby altering the material's mass. As explained above, a change of oxygen partial pressure as well as light illumination of sufficient energy alters the exchange rate of oxygen. Thus, the mass of the material changes. Arguably, this mass change can be monitored by the means of $GaPO_4$ microbalances, since minor changes (ng range) are detectable [38].

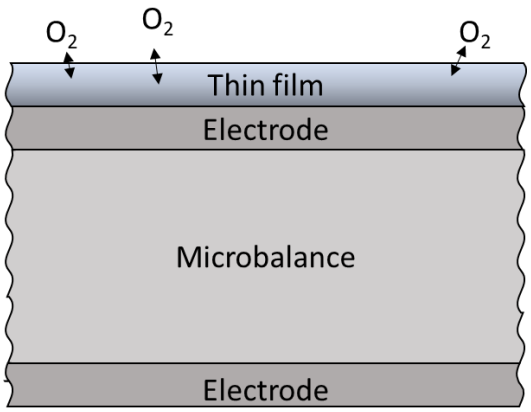

Figure 2.3-4 Illustration of oxygen exchange of a thin film on a microbalance with the surrounding atmosphere. The oxygen exchange reaction at the surface causes a mass change.

The determination of the oxygen nonstoichiometry δ of thin films is based on the work of Schröder, Fritze *et al* [21]. They used a modified form of the Sauerbrey equation, converting the mass change to oxygen nonstoichiometry δ. Regarding this approach, primarily the molar mass of $SrTi_{0.98}Fe_{0.02}O_3$ were used for the calculations of this thesis. Equations (27), (28) and (29) depict how to obtain oxygen nonstoichiometry δ and its change Δδ.

$$\frac{\Delta m}{m} = \frac{\Delta M_{Oxygen}}{M_{Thin\ film}} \tag{27}$$

$$\delta = -\frac{M_{Thin\ film}}{\Delta M_{Oxygen}} \frac{\Delta m}{m} \tag{28}$$

$$\Delta\delta = \delta - \delta_{initial} = \frac{\Delta m}{m} \frac{M_{Thin\ film}}{M_{Oxygen}} \tag{29}$$

The nonstoichiometry (number of oxygen vacancies decisive) due to external influences (change of $p(O_2)$, UV light illumination) is obtained relative to the nonstoichiometry caused by Fe-doping. The investigated thin film $SrTi_{0.98}Fe_{0.02}O_{3-\delta}$ consists of STO with 2 % Fe doping relative to Ti. If only Fe^{3+} is present in the specimens, due to charge balance, a maximum oxygen nonstoichiometry of 0.01 can be realized caused by doping. [12, 42]. The application of different oxygen partial pressure in the surrounding gas atmosphere and UV light illumination of the sample lead to a change of δ.

3. Experimental

3.1. Preparation of the single crystals

3.1.1. Cleaning of the single crystals

In the course of this thesis, two types of single crystal were used:

- STO single crystals (5 x 5 x 0.5 mm^3, (100) oriented, both sides polished, CrysTec GmbH Kristalltechnologie, Germany) were chosen for the in-plane conductivity experiments, compare Section 4.1.

- YSZ single crystals (10 x 10 x 0.5 mm^3, CrysTec GmbH Kristalltechnologie, Germany) were used for the voltage measurements, see Section 4.2.

These were prepared in the following way:

At first, the unconditioned single crystals were cleaned in an ultrasonic bath (VWR chemicals, USA) in roughly 100 ml of ethanol (purity > 99.99 %, VWR chemicals, USA) for 10 min. Afterwards, they were annealed in a chamber furnace (Carbolite RHF 1600, Carbolite Gero GmbH & Co. KG, Germany) at 900 °C for 12 h to remove potential superficial impurities and then cooled with 5 °C min^{-1}. Afterwards, they were rinsed with ethanol again.

3.1.2. Pulsed laser deposition (PLD)

For some of the experiments ceramic thin films were deposited by pulsed laser deposition (PLD) using a Kr/F excimer laser (Lambda COMPex Pro 205F, wavelength λ = 248 nm). The used deposition parameters can be found in Table 3.1-1.

Table 3.1-1 Parameters of the pulsed laser deposition

Thin film	Thickness desired [nm]	Pressure [mbar]	Frequency [Hz]	Heating power [%]	Target distance [cm]
STO	400	$1.5*10^{-1}$	5	92	6.0
Fe:STO	250	$1.5*10^{-1}$	5	92	6.0
LSC	415	$2.0*10^{-2}$	10	80	5.7
YSZ	200	$2.0*10^{-2}$	10	92	6.0
MgO	15	$2.0*10^{-2}$	10	92	6.0
LSCr	40	$1.5*10^{-2}$	5	92	6.0

The heating power, as depicted in Table 3.1-1, is the percentage of maximum power of the used heater. It typically equals a desired temperature of 650 °C. A precise temperature measurement could not be established.

3.2. In-plane conductivity experiments

3.2.1. Setup preparation

The used single crystals were prepared as described in Section 3.1.

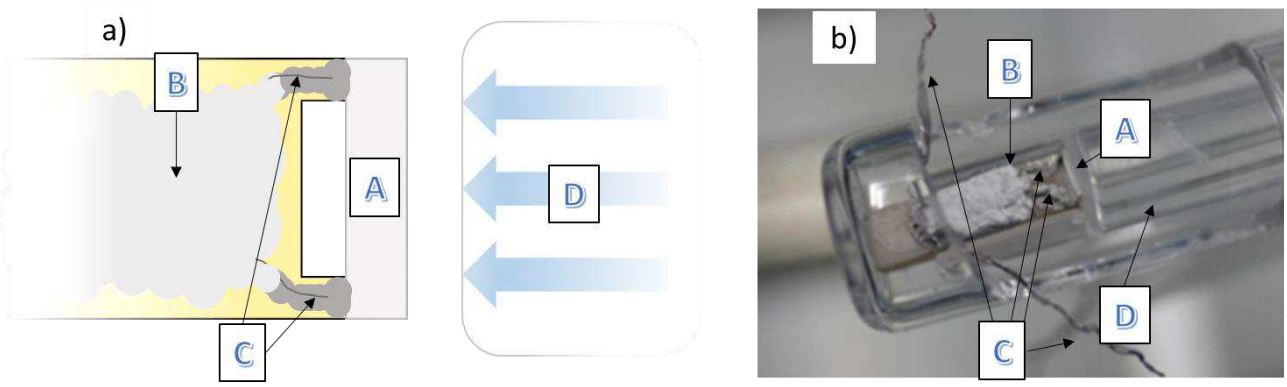

Figure 3.2-1 A not to scale sketch of the sample setup (a)) and a picture of the sample (b)).

The conductivity measurements were carried out on STO single crystals (5 x 5 x 0.5 mm^3, (100) oriented, both sides polished, CrysTec GmbH Kristalltechnologie, Germany). The elements of the setup are described as follows, as seen in Figure 3.2-1:

- A The pristine or conditioned sample "glued" onto the corundum ship with Pt paste.
- B "Corundum ship": A 30 x 5 x 5 mm^3 cut and polished piece of corundum with Pt wires sintered on top.
- C Pt wires for contacting the sample.
- D Quartz rod as light conductor.

In order to contact the samples with the Pt wires on the corundum ship, Pt paste (Tanaka Kikinzoku International (Europe) GmbH, Germany) was brushed on to two opposing edges (distance 3-4 mm) of the backside, glued onto the corundum ship and put into a chamber furnace to calcine the Pt paste at 850 °C for 2.5 h.

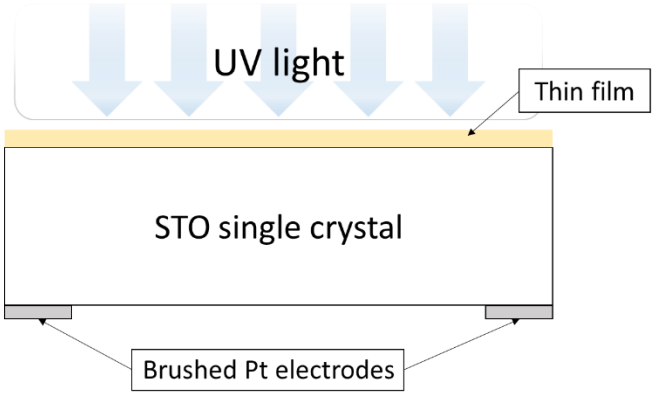

Figure 3.2-2 Sketch of a STO single crystal sample with a thin film on top during measurement.

When an STO sample with a thin film on top was measured, the thin-film side was facing the quartz rod, as depicted in Figure 3.2-2.

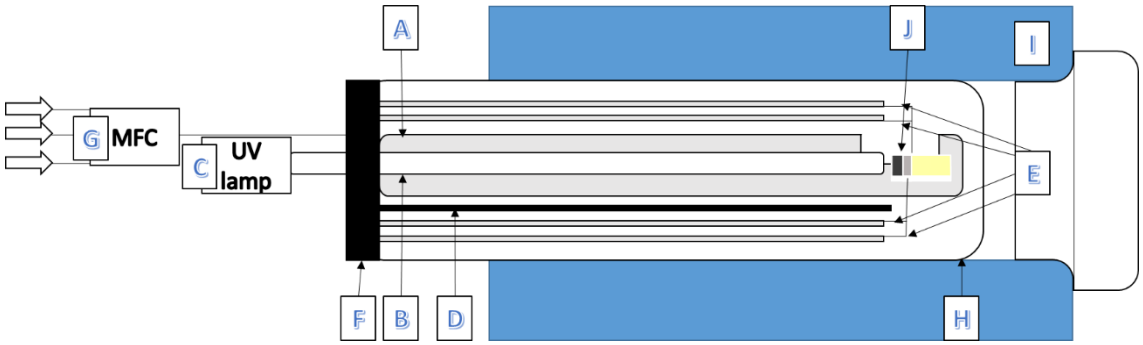

Figure 3.2-3 Schematic sketch of the experimental setup for the in-plane conductivity experiments.

The measurement apparatus, as seen in a schematic sketch in Figure 3.2-3, consists of the following elements:

- A Hollow rod of fused quartz glass was used as base.
- B Rod of quartz glass, which functions both as fixation as well as light conductor of the UV light from the LED.
- C UV LED.
- D Type-S thermocouple mounted in a fused silica housing.
- E Four Pt wires for contacting the sample.
- F Flange melted to the base with feedthroughs for the electrical and thermocouple wires.
- G Two mass flow controllers to adjust the gas atmosphere with flows from 10 to 100 sccm.
- H Quartz glass tube as gas tight housing that is closed in the front.
- I Tube furnace on guide rails to control the experimental temperature.
- J Sample prepared as described in Section 3.1.

The STO single crystals were analyzed by impedance spectroscopy. To do so, the corundum ship was clamped between a quartz rod, which functions as a light conductor, and the end of the hollow rod, as seen and described in Figure 3.2-1. The setup was positioned in a tube furnace with UV–LED light exposure by means of a quartz rod at temperatures between 340 and 400 °C in either pure N_2 or O_2 atmosphere or mixtures of both of these gases. UV illumination and oxygen exchange took place at the surface of the sample facing the UV light. The sample's impedance was measured before, during, and after UV exposure by means of a Novocontrol Alpha-A high-performance frequency analyzer with an Electrochemical Test Station POT/GAL 30 V/2 A or a Novocontrol Alpha-A high-performance frequency analyzer, respectively (both Novocontrol Technologies GmbH & Co. KG, Germany).

UV irradiation was performed by means of a UV–LED (365 nm, 3 W radial output) from Led Engin Inc., USA and a quartz rod, acting as optical guide for the UV light.

Table 3.2-1 provides an overview over the applied measurement parameters of the in-plane conductivity experiments

Table 3.2-1 Overview in-plane conductivity measurements parameters

Thin film	Gas atmosphere	Illumination time [s]	Relaxation time [s]	Temperature [°C]
None	Air	$7.2*10^3$	$2.6*10^4$	340
None	N_2	$7.2*10^3$	$3.6*10^4$	340
None	O_2	$7.2*10^3$	$3.6*10^4$	340
LSCr20 (40 nm)	Air	$1.6*10^4$	$2.0*10^4$	380 – 410
YSZ + LSCr10 (200 + 40 nm)	Air	$1.9*10^4$	$2.0*10^4$	340 – 390
YSZ (~200 nm)	Air	$1.4*10^4$	$3.1*10^4$	340 – 390
MgO (~15 nm)	Air	$1.4*10^4$	$3.1*10^4$	340 – 390

3.3. SOPEC voltage measurements

3.3.1. Sample preparation

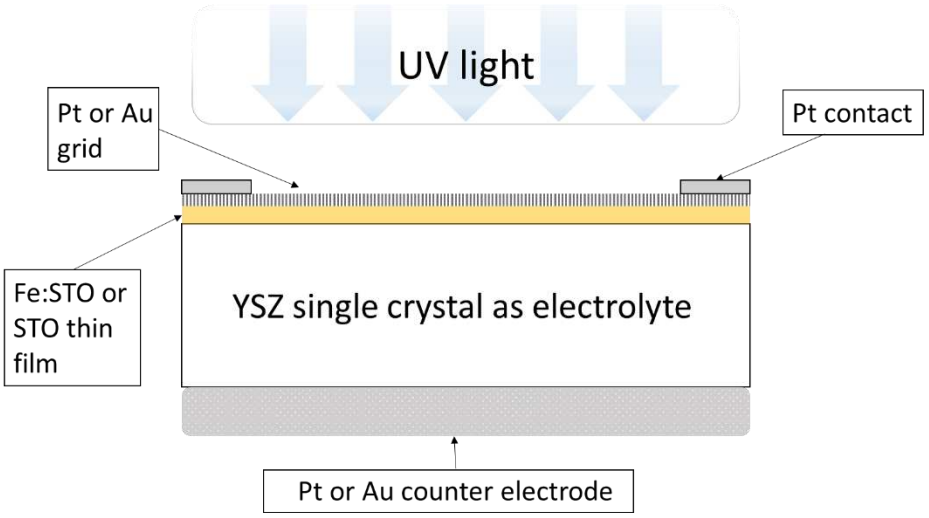

Figure 3.3-1 Schematic sketch of the prepared SOPECs during a measurement

The voltage measurements were carried out on a 10 x 10 x 0.5 mm^3 YSZ single crystal (CrysTec GmbH Kristalltechnologie, Germany) as a base. A schematic sketch of the resulting solid oxide photoelectrochemical cells (SOPECs) in this thesis is depicted in Figure 3.3-1 and consists of the following layers (from bottom to top):

1. Either a porous Pt or a porous Au counter electrode layer
2. A 10 x 10 x 0.5 mm^3 (100) yttria-stabilized zirconia (YSZ) single crystal, both sides polished
3. Either STO or Fe:STO thin film layer
4. A sputter deposited metal grid, Au or Pt

On top of the ceramic thin film, prepared as explained in Section 3.1, a structured metal layer of either Au or Pt was deposited. A grid with a bar width of 25 µm and a mesh opening of 100 µm was chosen as pattern. The structuring of the film was performed using lift-off photolithography as follows:

1. 100 µl of negative photoresist was spincoated onto the deposited thin film for 30 s and baked for at least 5 min at 100 °C.
2. A patterned mask was applied on the surface to expose the sample (with mask) to the radiation of a high pressure Hg lamp (365 nm, 350 W, USHIO 350DP, Ushio Inc., JAP) that hardens the photoresist within an illumination time of 50 s.
3. A developer (ma-D 533S, Micro Resist Technology GmbH, GER) was applied on the surface for 45 s to dissolve the photoresist at regions that were not exposed to UV light.
4. The metal layer, Au or Pt, was deposited using a magnetron BAL-TEC MED020 sputtering device (BAL-TEC, now Leica Microsystems, Austria). The deposition parameter are summarized in Table 3.3-1.
5. The metal layers and the remaining photoresist were removed together by ethanol in an ultrasonic bath (lift-off). The success of the photolithography step was checked by optical microscopy (Zeiss Imager.M1m).

Table 3.3-1 Sputter deposition parameters

Thin film	Thickness desired [nm]	Current [mA]	Deposition time [s]	Pressure Ar [mbar]
Pt	200	100	323	$2.0*10^{-2}$
Au	200	100	190	$2.0*10^{-2}$

Lastly, a porous Au or Pt counter electrode (Tanaka Kikinzoku International (Europe) GmbH, Germany) was brushed on, calcined at 650 °C for 2 h and cooled down 5 °C min^{-1}.

3.3.2. Measurement setup

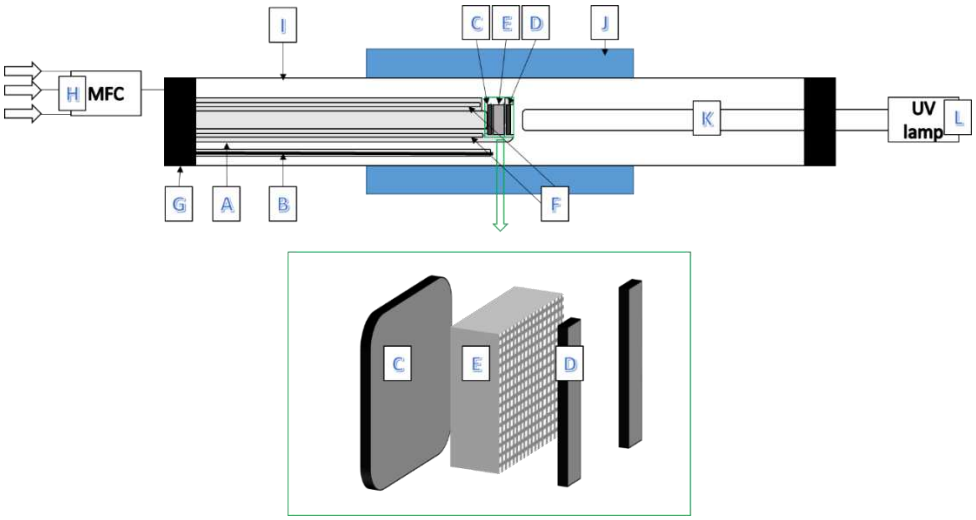

Figure 3.3-2 Schematic sketch of the experimental setup for the DC experiments. The elements are explained in the text below.

A schematic sketch of the measurement apparatus is depicted in Figure 3.3-2. It consists of the following elements:

- A Hollow rod of fused quartz with a spring mechanism for fixation was used as base.
- B Type-S thermocouple mounted in a fused silica housing.
- C Pt foil placed at the backside of the sample.
- D Two Pt foils placed at the edges of the patterned front side of the sample.
- E The sample, facing the quartz rod with the patterned front side.
- F Two Pt wires contacting the Pt foils from the front side and the backside, respectively.
- G Steel flange glued to the base with gas in- and outlets and Feedthroughs for the electrical and thermocouple wires.
- H Mass flow controller to adjust the gas atmosphere.
- I Tube borosilicate glass, which is open on both sides.
- J Tube furnace on guide rails to control the experimental temperature.
- K Rod of quartz glass as a light conductor.
- L UV light LED (Led Engin Inc., USA).

The parts in the heated area of the apparatus were made of inert materials (quartz glass for the tubes, rods, spacers, etc. and Pt for the metallic parts) to avoid any contamination of the samples.

The DC experiments were carried out on the specimens listed in Section 3.3. On that account, a Keithley 2000 multimeter unit was used to measure the open-circuit voltage. The sample was positioned between a flat Pt foil at the backside, contacting the porous metal counter electrode layer, and two folded Pt foils at two opposing edges of the front side. The end of the UV light conducting quartz rod was placed approximately 1 cm short of the sample. Light-emitting diodes (LEDs; Led Engin Inc., USA) of a wavelength of 365 nm were used on the other side of the quartz rod to illuminate the samples.

The $p(O_2)$ dependency measurements were conducted at 300 °C and 350 °C, respectively. The gas atmosphere was adjusted by a Brooks Instrument (GF80, thermal, Brooks Instrument GmbH, Germany) mass flow controller. The oxygen partial pressure was changed by filling the setup with different gas mixture of O_2, N_2 and a mixture of 99 % N_2 and 1 % O_2. Hereby, the oxygen content of the pure N_2 atmosphere is estimated to be 80 ppm due to leakage of the gas pipe system. The $p(O_2)$ was changed gradually seven times with turning the UV light on and off twice for 2 h per $p(O_2)$ at each temperature. The total gas flow was 50 sccm. In Table 3.3-2, the proportions of the gas flows are summarized.

Table 3.3-2 Utilized gas atmospheres and resulting oxygen partial pressures

$p(O_2)$ [bar]	$\log(p(O_2))$	N_2 [sccm]	1 %O_2 [sccm]	O_2 [sccm]	Flow [sccm]
$8.0*10^{-5}$	-4.10	50	0	0	50
$1.1*10^{-3}$	-2.97	45	5	0	50
$2.1*10^{-3}$	-2.69	40	10	0	50
$5.0*10^{-3}$	-2.30	25	25	0	50
$8.0*10^{-3}$	-2.10	10	40	0	50
$9.0*10^{-3}$	-2.05	5	45	0	50
$1.0*10^{-2}$	-2.00	0	50	0	50
$2.1*10^{-1}$	-0.68	10.5	0	39.5	50
$1.0*10^{0}$	0.0	0	0	50	50

Table 3.3-3 provides an overview over the applied measurement parameters of the open-voltage measurements of the solid oxide photoelectrochemical cells.

Table 3.3-3 Summary of the measurement parameters of the SOPEC voltage measurements. The sample name x-y denotes the thin film (x) and the current collector (y).

Type	Sample	Gas atmosphere	Illumination time [s]	Temperature [°C]
Initial	Fe:STO-Pt	Air	$5.7*10^4$ and $1.0*10^4$	350
			$1.4*10^4$	300
	Fe:STO-Au	Air	$1.2*10^4$	350
	STO-Pt	N_2	$7.8*10^3$ and $3.8*10^3$	300
		O_2	$3.8*10^3$ and $7.3*10^3$	300
	STO-Au	Air	Time steps	350
$p(O_2)$	each	$p(O_2)$ steps	$7.2*10^3$	300, 350

3.4. Microbalance $GaPO_4$

3.4.1. Sample preparation

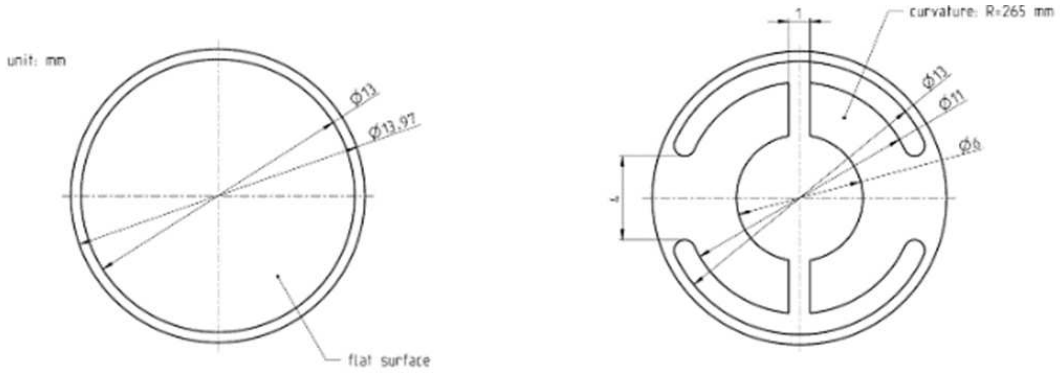

Figure 3.4-1 Sketches with dimensions of the used $GaPO_4$ microbalances. The active area in the middle amounts to 28 mm^2. [43]

In the course of this thesis, two types of commercial $GaPO_4$ microbalances (Y-11 ° cut, Piezocryst, Austria) were used to investigate minor weight changes of STO and Fe:STO thin films, see Figure 3.4-1. The ones with a thickness of 0.2 mm have a conductive Pt layer on the opposing side of the anchor and do not need further preparation for mass change measurements. The ones with a thickness of 0.3 mm do not have a conductive Pt layer on the opposite side of the anchor, thus, they need a deposition of a Pt layer before using them in mass change measurements. A layer of 200 nm Pt was deposited by magnetron sputtering with the parameters from Table 3.3-1.

A 28 mm^2 large area between Pt-electrodes on both the front and the backside the single crystal is piezoelectric-active with a resonance frequency of 5.6 +/- 0.1 MHz (nominal sensitivity $7.42*10^7$ Hz cm^2 g^{-1}) for 0.2 mm thick, or 4.1 MHz (nominal sensitivity $3.84*10^7$ Hz cm^2 g^{-1}), respectively.

Ceramic thin films (STO, Fe:STO, LSC) were deposited on the microbalances *via* PLD for most of the experiments. In Table 3.1-1, the deposition parameters are summarized.

3.4.2. Measurement setup

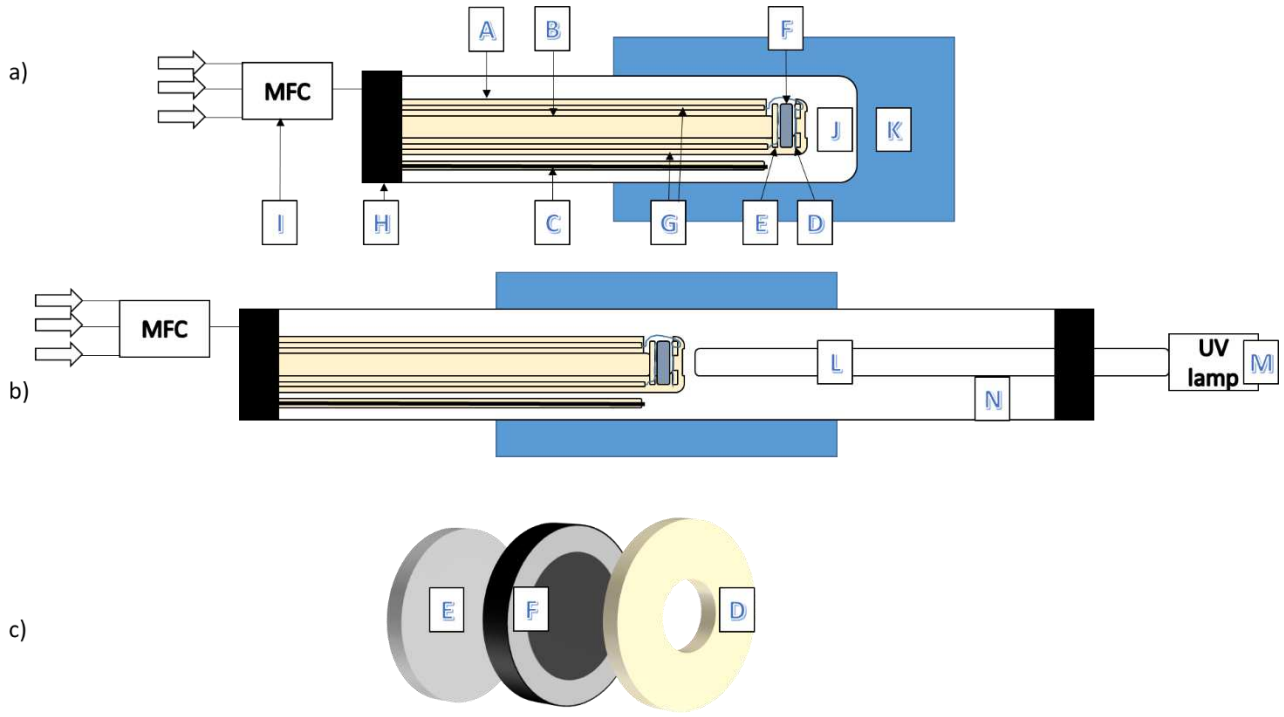

Figure 3.4-2 Schematic sketch of the experimental setup of the mass change experiments. a) illustrates the setup for the gas exchange experiments, b) sketches the setup for the UV light illumination experiments and c) denotes how the sample is placed in the setup between the corundum discs.

The measuring setup consists of two parts, a measuring apparatus, on which the sample was mounted and contacted, and a tube furnace. The measuring apparatus for the gas exchange experiments consists of the following elements, see also Figure 3.4-2:

- A Hollow rod of corundum of 36 mm diameter with a hole at the front side.
- B Hollow rod of corundum of 14 mm diameter for keeping the sample in position.
- C Type-S thermocouple mounted in a corundum housing.
- D One corundum disc of 22 mm diameter with a drilled hole of 8 mm diameter, 200 nm Pt sputtered on the one side and a Pt wire on the other side to contact the microbalance sample on the front side.
- E Corundum disc of 22 mm diameter with 200 nm Pt sputtered on the one side and a Pt wire on the other side to contact the microbalance sample on the anchor side.
- F Microbalance sample
- G Pt wires in a housing of corundum.
- H Steel flange glued to the base with gas in- and outlets with feedthroughs for the electrical and thermocouple wires.
- I Mass flow controller to adjust the gas atmosphere.
- J Quartz glass tube as gas tight housing, which is closed in the front.
- K Tube furnace on guide rails to control the experimental temperature.

For the UV light illumination measurements, the following additional elements were used:

- L Rod of quartz glass as a light conductor.

M UV light LED (LED Engin Inc., USA).
N Gas tight tube borosilicate glass, which is open on both sides.

The gas atmosphere was adjusted as described in Section 3.3 and seen in Table 3.3-2. Pure N_2 and O_2 atmosphere, respectively, as well as a mixtures of these two gases were used, with resulting oxygen partial pressures between $8*10^{-5}$ and $1*10^{0}$ bar. The experimental temperature ranged from 360 °C to 450 °C.

As in the previous Section 3.3, a light-emitting diode (LED; Led Engin Inc., USA) of a wavelength of 365 nm was used to illuminate the samples. It was mounted on the opposing side of the light conducting quartz rod.

The shift in the resonance frequency of the samples was measured with an electrochemical quartz crystal microbalance (EQCM) resonator (Gamry, USA).

The mass change measurements were conducted in either ambient, pure N_2 or O_2 atmosphere or a mixture of these two gas atmospheres, in a temperature range between 350 and 440 °C. The parameters of the performed measurements are summarized in Table 3.4-1.

Table 3.4-1 Summary of the performed experiments with operational parameters.

Type	$GaPO_4$ thickness [mm]	Thin film	Temperature [°C]	Gas atmosphere	Flow [sccm]
T-dependency	0.2	None	370 - 430 370 – 390	Air N_2	40
	0.2	STO	350 - 450 380 - 400 370 - 430	N_2 O_2 vac., $2*10^{-2}$ mbar	40
Gas exchange	0.2	STO	380 400 440 380	$p(O_2)$ variation N_2	40 40 → 10
	0.3	LSC	380	$p(O_2)$ variation	10
	0.3	Fe:STO	380 - 410	$p(O_2)$ variation	10
UV light illumination	0.3	None	380	O_2	10
	0.3	Fe:STO	380 380 380 - 410	N_2 O_2 Air	10

4. Results & Discussion

4.1. Determination of in-plane conductivity

The aim of these experiments was to investigate the influence of UV light illumination on the in-plane conductivity of STO single crystal samples. Said effect is referred to as light effect in the following. The light effect primarily originates from two UV light induced, time-dependent effects, which can be considered separately: a photoelectrical and an electrochemical process (see also Section 2.1.).

Initially, the photoelectric contribution is, in most cases, the more dominant part of the increase. Absorption of light of sufficient causes excitation of charge carriers to higher-energy states. The effect vanishes as soon as the light is turned off [34, 35].

To characterize the STO cell system, prepared as described in Section 3.2, impedance measurements were conducted in either ambient atmosphere, in pure O_2 or N_2 atmosphere and in a temperature range from 340 to 390 °C. At each temperature step, the sample was illuminated by a UV LED either two or three times. The process of the measurement before, during and after one UV light illumination will be referred to as *illumination cycle* in the following.

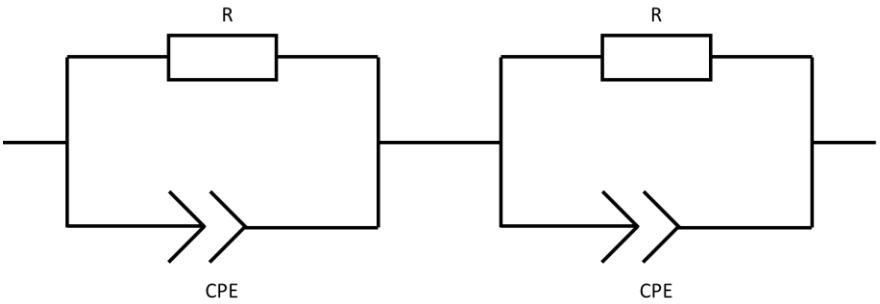

Figure 4.1-1 Chosen equivalent circuit to fit the impedance spectra consisting of two R||CPE elements in series.

All impedance spectra consisted of a high frequency semicircle, which represents the bulk resistance (STO single crystal) and shifts towards higher frequencies during illumination, and a low frequency semicircle, which represents the electrodes' resistance and space charge. The equivalent circuit depicted in Figure 4.1-1, consisting of two R||CPE elements in series, was chosen to fit the spectra.

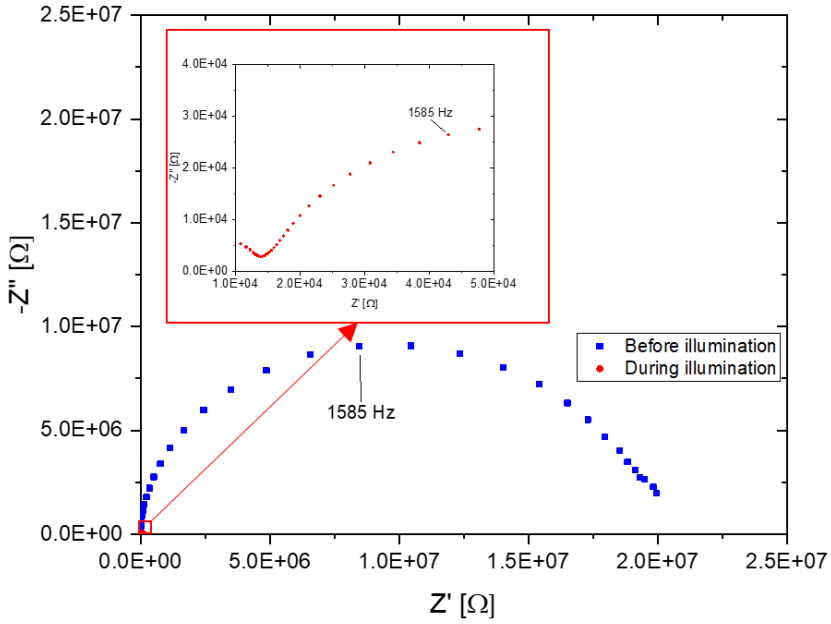

Figure 4.1-2 Typical impedance spectra of a STO in-plane measurement before (blue squares) and during (red dots) UV light illumination. The electrolyte's resistance differs by three orders of magnitude. These spectra were measured at 340 °C in air.

In Figure 4.1-2, emblematic impedance spectra of the STO in-plane conductivity measurements are displayed. In this case, the measurement was conducted at 340 °C in air. The blue curve corresponds to the impedance before the UV light is turned on, the red curve stands for the impedance during illumination. Evidently, the overall resistance decreases by three orders of magnitude due to UV light illumination. While before illumination, only one semicircle is resolved in the measured frequency range (bulk arc), after illumination, two arcs are found. The leftmost semicircle could be attributed to the single crystal's resistance. Further results will be discussed in detail in the following sections.

For the purpose of overview, Table 3.2-1 displays the measurement parameters that were chosen for the in-plane conductivity measurements. STO single crystal samples with no thin film as well as thin films on top were investigated at different gas atmospheres and temperatures.

A part of the discussion revolves around the comparison of the in-plane conductivity before and during UV light illumination, as well as the relaxed conductivity after a defined time, the relaxation time (see Table 3.2-1). Figure 4.1-3 explains how the comparison graphs of this work should be interpreted.

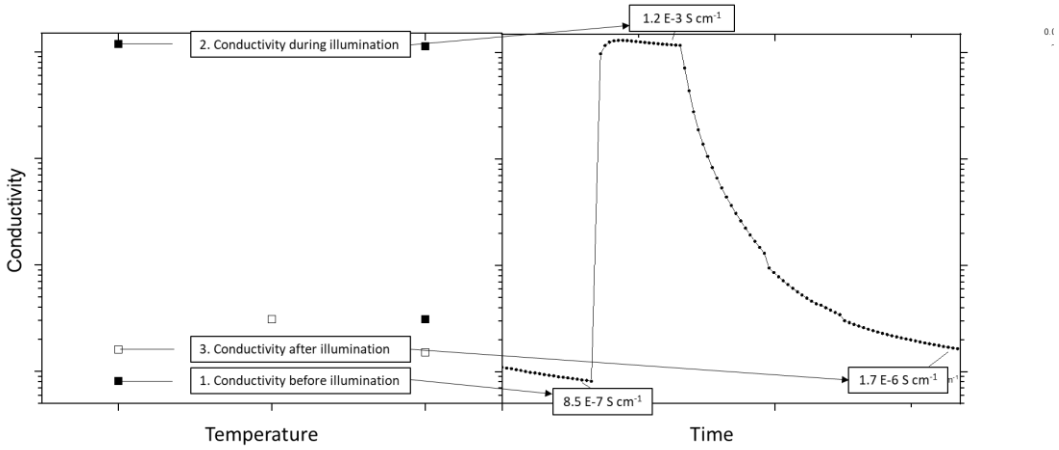

Figure 4.1-3 Illustration of how the comparison plots are created. The conductivity before illumination corresponds to the lowest filled symbol. The elevated filled symbol stands for the conductivity during illumination. The hollow symbol represents the relaxed conductivity.

The values of the in-plane conductivity are extracted from an illumination cycle exemplarily. The filled symbol at the bottom indicates the value of the in-plane conductivity seconds before the UV light is turned on. The elevated filled symbol stands for the conductivity during UV illumination right before the light is turned off. The hollow symbol represents the relaxed conductivity at the end of the relaxation time, and will be denoted with the affix “relax”.

On top of that, the time τ was determined, after which the conductivity reaches a factor of e^{-1} during relaxation for better comparability of the samples.

In the following, UV light illumination is indicated with a blue highlighted area in the figures.

4.1.1. Influence of the heating by the UV LED on the temperature of the sample

The actual temperature cannot be safely determined, since the thermocouple is placed two centimeters below the specimen, compare Figure 3.2-3. Therefore, the sample is certainly heated up more than measured by the thermocouple. Estimations suggest an increase of minimum 15 to 20 °C. From calculations according to the Denk model [8], it arises that within a temperature increase of 20 °C (e.g. from 340 to 360 °C) in air and a defect concentration of $1*10^{16}$ acceptor dopants per cm^3 (due to impurities), the conductivity increases by a factor of 1.5 (in this case $1.40*10^{-6}$ S cm^{-1} to $2.24*10^{-6}$ S cm^{-1}). In comparison, the light effects contribute by a factor of ~1000. As a result, it can be assumed that the contribution of the heating is almost negligible to the gain in conductivity.

4.1.2. Pristine STO sample

A pristine STO single-crystal sample, prepared as described in Section 3.2, with no thin film on top was investigated at 340 °C in different gas atmospheres. At first, the measurements are explained and discussed in extract. Afterwards, all the results of the measurements are compared.

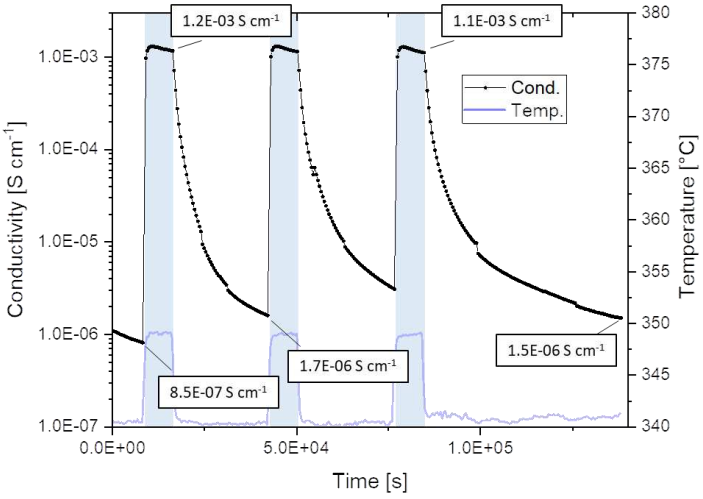

Figure 4.1-4 Results of the first in-plane conductivity measurement of a pristine STO single crystal with three illumination cycles in air at measured 340 °C. Illumination is highlighted with a blue area.

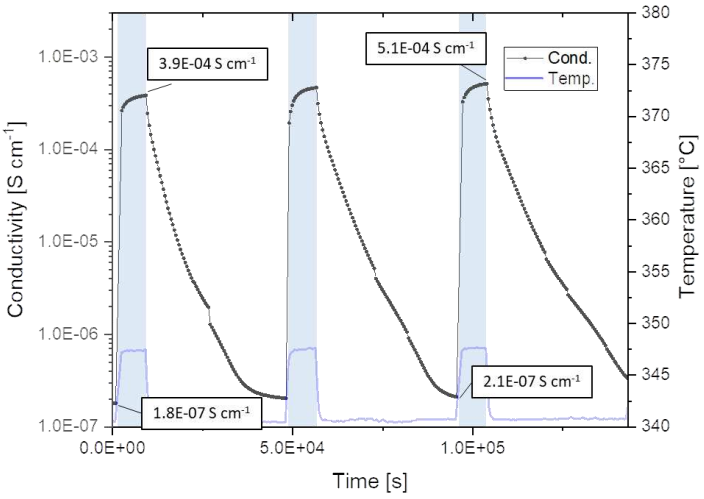

Figure 4.1-5 Results of the in-plane conductivity measurement of the pristine STO single crystal in pure N_2 atmosphere at measured 340 °C. The conductivity fully relaxes during the relaxation time. Illumination is highlighted with a blue area.

In Figure 4.1-4, the results of the first measurement of the STO sample are shown. The measurement was carried out in air, at a temperature of 340 °C. The negative slope at the beginning of the measurement, before the first illumination cycle, originates from the non-equilibrium state of the sample, before the experiment began. The calculated in-plane conductivity amounts to roughly $8.5*10^{-7}$ S cm^{-1} at the beginning. When turning the UV light on, the conductivity jumps up by three orders of magnitude to a value of approximately $1*10^{-3}$ S cm^{-1}. At the same time, the measured temperature increases by 8 °C. After the illumination cycle, the conductivity does not relax to the initial state within 8 h, but remains on a slightly enhanced level, 1.5 10^{-6} S cm^{-1}, which is roughly a factor 1.8 greater than the initial value at the beginning of the experiment.

In pure N_2 atmosphere (~80 ppm O_2), see Figure 4.1-5, the initial conductivity, $1.8*10^{-7}$ S cm^{-1}, of the single crystal is by a factor of 5 lower than in air at the same temperature (340 °C). Furthermore, it does not escalate to $1*10^{-3}$ S cm^{-1}, as in air, but remains at approximately $4*10^{-4}$ S cm^{-1} during the first illumination cycle. Remarkably, the conductivity relaxes back to almost the value before illumination ($1.9*10^{-7}$ S cm^{-1}). In the following illumination cycles, the conductivities before, during, as well as the relaxed conductivity range in the same magnitudes as in the first illumination cycle.

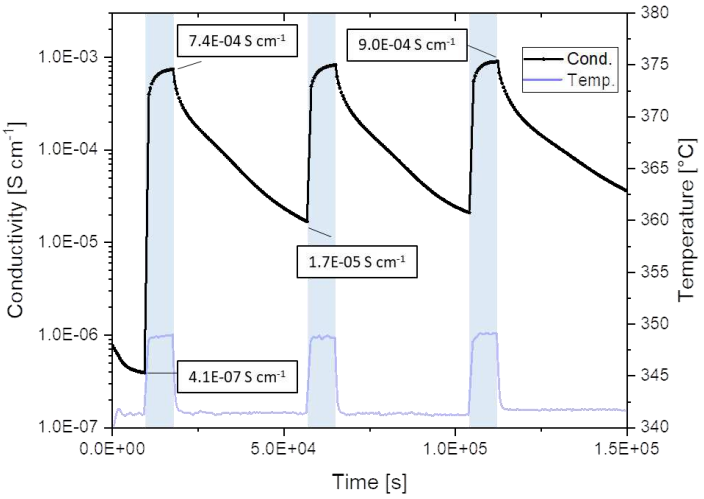

Figure 4.1-6 Results of the in-plane conductivity measurement of the STO single crystal in pure O_2 atmosphere at measured 340 °C. As seen in the experiments in air and pure N_2 atmosphere, the in-plane conductivity jumps up three orders of magnitude during illumination. The sample does not exhibit a full relaxation during the relaxation time. Illumination is highlighted with a blue area.

The results of the in-plane conductivity measurement of the STO single crystal in pure O_2 atmosphere at 340 °C are displayed in Figure 4.1-6. The initial conductivity ranks between the two initial values of the previous measurements ($4.1*10^{-7}$ S cm^{-1}). As seen in the experiments in air and pure N_2 atmosphere, the in-plane conductivity jumps up by three orders of magnitude during illumination to $7.5*10^{-4}$ S cm^{-1}. The relaxed in-plane conductivity amounts to a value of 1.7 10^{-5} S cm^{-1} (a drop to 2.3 % of the conductivity under UV light illumination), a factor of roughly 41 higher than the initial value at the start of the experiment. The following illumination cycles resemble the first one in the shape.

In ambient atmosphere, the UV light usually causes enhanced oxygen incorporation into STO. When there is only little oxygen available (e.g. in pure N_2 atmosphere), there are two possibilities, why the conductivity increases (apart from photocurrent): either less oxygen is incorporated, or the UV light even accelerates oxygen release. A consequence of the second possibility would be that the majority charge carriers were electrons and not holes as usual. This would go along with a shift in the Brouwer diagram [11], see Figure 2.1-3, from the right to the left regime. This is especially important for the relaxation, when the light is off.

Accordingly, the relaxation behavior appears to be closely intertwined with the oxygen content of the surrounding atmosphere. When the UV light is turned off, the conductivity relaxes in a faster manner when the atmosphere lacks oxygen. As a result, the in-plane conductivity reaches the initial value within the relaxation time of 8 h in N_2. Once the UV light is turned off in pure O_2 atmosphere, the relaxation is decelerated compared to the measurements in air and N_2 and the conductivity is slowly but steadily decreasing. This relates the oxygen partial pressure of the surrounding gas atmosphere to space charge and surface effects, making the kinetics of oxygen exchange surface-limited. Accordingly, the equilibration time in pure O_2 atmosphere is much longer in N_2 and air and beyond the experiment's relaxation time. This indicates and confirms that the relaxation is function of the oxygen partial pressure [44].

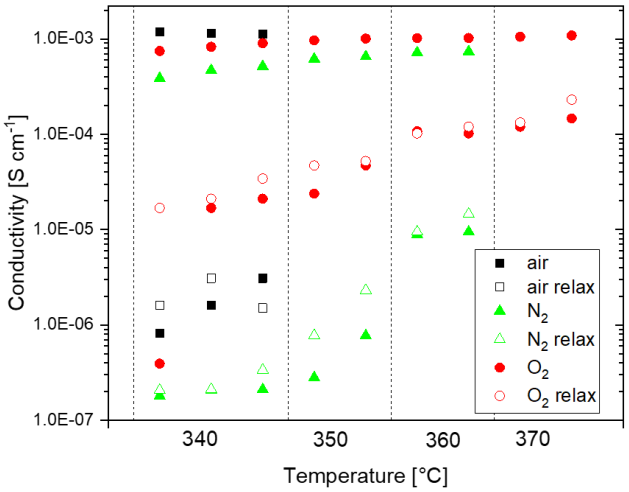

Figure 4.1-7 Comparison of the result of the in-plane conductivity measurements of the pristine STO sample in different gas atmospheres. The affix "relax" denotes the relaxed conductivity at the end of the relaxation time.

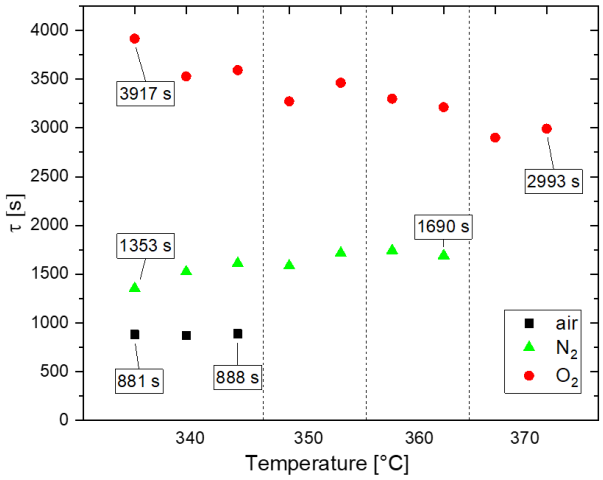

Figure 4.1-8 The time τ, after which the sample reaches a factor of e^{-1} during relaxation versus temperature. In O_2, the sample takes by factor of ~ 4 longer to relax than in air.

In Figure 4.1-7, the results of the pristine STO sample in the three different gas atmospheres are compared. Four temperatures are used and two to three cycles are performed for each temperature, indicated by two or three columns for each T in Figure 4.1-7. Before the first illumination cycle, the obtained conductivities are within one order of magnitude ranging from roughly $2*10^{-7}$ S cm^{-1} in N_2 atmosphere, to $8*10^{-7}$ S cm^{-1} in air. The initial conductivity in air is significantly higher than in pure O_2 atmosphere, namely roughly a factor of two. It seems that the specimen was not in an equilibrium state at the beginning of the measurement in air and oxygen, since at such low temperatures full equilibration would take several days.

During the first illumination cycle, the sample's in-plane conductivity escalates three orders of magnitude during UV light illumination and reaches a threshold of roughly $1*10^{-3}$ S cm^{-1}. This applies for every gas atmosphere reaching the highest conductivity in air.

The measurements differ the greatest during the relaxation. While the sample reaches the initial conductivity in N_2 after 8 h of relaxation, the conductivity remains on an enhanced level in air. The measurement in pure O_2 atmosphere even displays a conductivity raise of roughly 1.5 orders of magnitude after 8 h, compared to the initial state. The same applies for the second and third cycle at 340 °C. In air, the conductivity remains enhanced by a factor of roughly 2 after the first illumination cycle. It is noteworthy that the relaxed conductivity of the third cycle in air is after a relaxation time of over $5*10^4$ s. This is the reason why it lies beneath the conductivity before illumination. At 350 °C, the sample does not exhibit full relaxation in pure N_2 atmosphere, but is enhanced by a factor of 2-3 after both illumination cycles, most probably due to longer lasting effects caused by the previous cycles. In all applied atmosphere, the slow conductivity decay after UV irradiation implicates a specimen composition changing effect, e.g. oxygen incorporation by UV light. Photoconductivity is not able to explain such long-lasting conductivity changes at such temperature, since this effect typically vanishes within µs [45] after the UV light is turned off.

In Figure 4.1-8, the determined τ values are plotted versus temperature. It is well illustrated that in O_2 atmosphere, it takes the sample the longest to relax, with values ranging from ~4000 s at 340 °C to roughly 3000 s at 370 °C. Even though the sample reaches the initial conductivity within the relaxation time in N_2 at 340 °C, it takes 60 % longer (~1400 s) than in air (~900 s) to relax to a conductivity of a factor of e^{-1}. This underlines the assumption that this process is surface-limited depending on the applied gas atmosphere.

4.1.3. STO single crystal with thin film on top

The subsequent measurements were carried out to investigate the influence of deposited thin films on the in-plane conductivity during UV light illumination.

4.1.3.1. LSCr-type thin films

LSCr10 and LSCr20 thin films are often used in research as top layers for high temperature solid oxide photovoltaic cells [46] and known to p-type conducting in oxidizing conditions [47, 48]. For this reason, it was investigated, whether the deposition of such thin film might influence the in-plane conductivity and its relaxation.

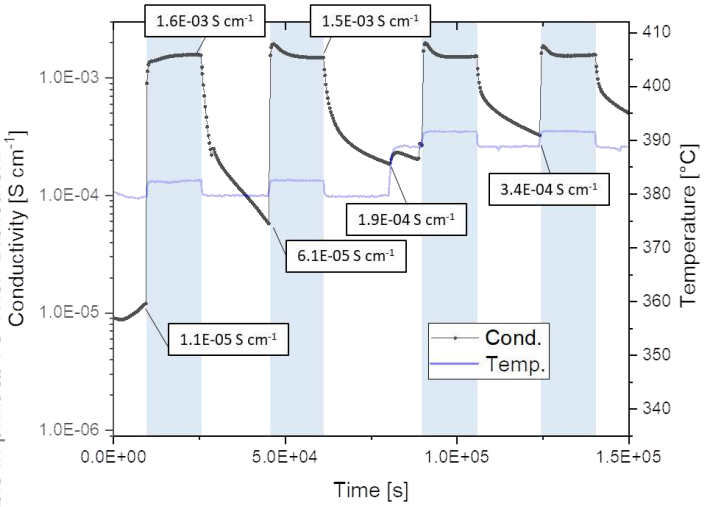

Figure 4.1-9 Results of the STO in-plane conductivity with an LSCr20 thin film upon at measured 380 and 390 °C in air. The conductivity and relaxation behavior resembles the STO sample in pure O_2 atmosphere. Illumination is highlighted with a blue area.

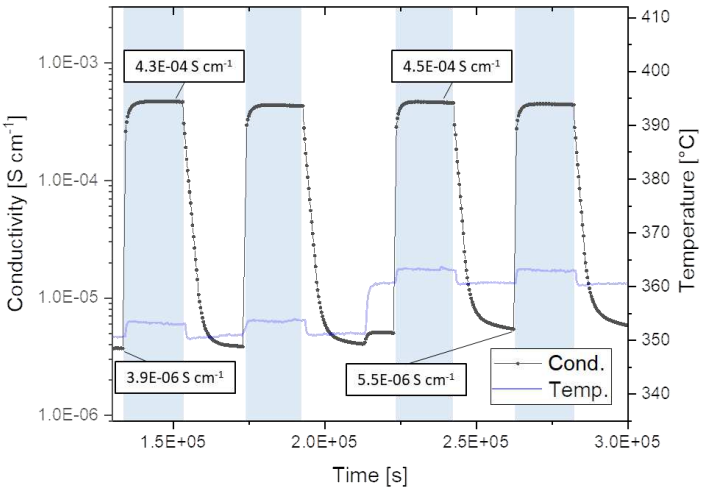

Figure 4.1-10 Results of the STO in-plane conductivity measurement in air with an YSZ and an LSCr10 thin film on it. The illumination cycles at measured 350 and 360 °C are displayed. Illumination is highlighted with a blue area.

STO with a deposited 40 nm LSCr20 thin film (results at 380 and 390 °C are depicted in Figure 4.1-9) initially exhibits an in-plane conductivity roughly $1*10^{-5}$ S cm at 380 °C, which increases to $1.6*10^{-3}$ S cm^{-1} during the first illumination cycle. Afterwards, it relaxes to a conductivity of $6.1*10^{-5}$ S cm^{-1} after 5 h of relaxation time. Remarkably, during the second illumination cycle, the conductivity initially reaches a maximum immediately at the beginning of the illumination, and then declines to a value of $1.5*10^{-3}$ S cm^{-1}, a factor of roughly 24.5 than higher before the cycle. This shape of the course of the conductivity also occurs during the following illumination cycles. The relaxed conductivity in the following cycles is enhanced by a factor of 2.5 - 3.5 compared to the value before illumination after each cycle. The relatively high conductivity might be caused by the fact that LSCr20 is higher conducting than STO (5 - 9.5 S cm^{-1} at 400 °C [49]).

The YSZ_LSCr10 sample composition was chosen after the LSCr20 sample conductivity was determined. The YSZ layer between the single crystal and the LSCr10 thin film was meant as an oxygen-conducting [50] barrier to deter the current from flowing only over the LSCr10 layer, but also through the YSZ layer and the single crystal. The results of the measurement at 350 and 360 °C are depicted in Figure 4.1-10. The sample initially displays a conductivity of $3.9*10^{-6}$ S cm^{-1} at 350 °C. When illuminating with UV light, the conductivity jumps up to approximately the maximum value of 4.3 – 4.5 10^{-4} S cm^{-1} during each illumination cycle. Remarkably, the conductivity relaxes back to the state before illumination already after

2 h of relaxation time. This occurs at every investigated temperature, during every illumination cycle and might indicate that the YSZ layer facilitates relaxation.

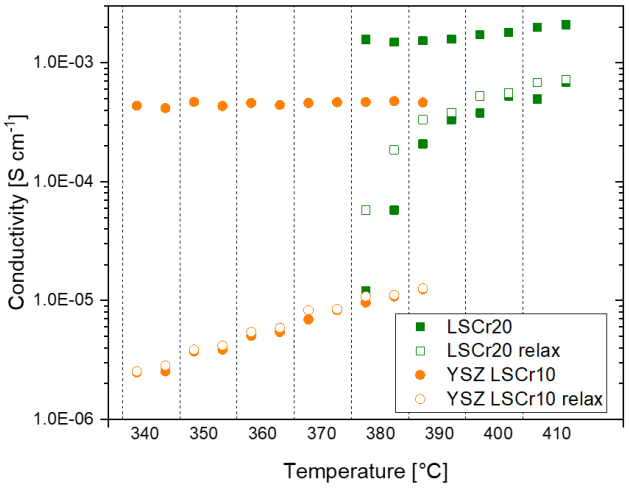

Figure 4.1-11 Comparison of the results of the measurements of an STO sample with a layer of LSCr20 on top with an STO sample with layers of YSZ and LSCr10 on top in ambient atmosphere. The affix "relax" denotes the relaxed conductivity at the end of the relaxation time.

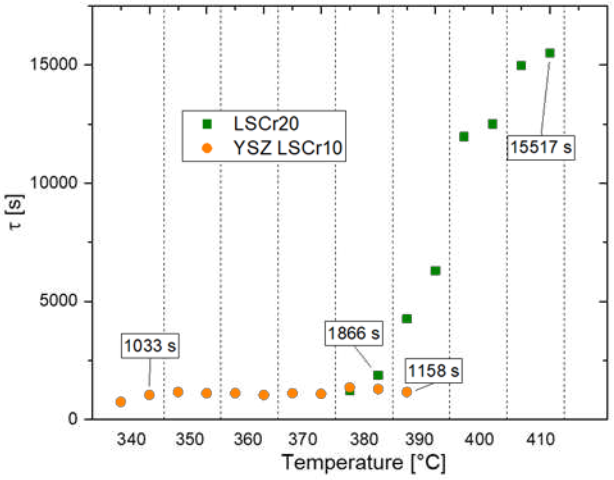

Figure 4.1-12 The time τ, after which the sample reaches a factor of e^{-1} during relaxation versus temperature. The values for the YSZ_LSCr10 sample remain relatively constant, the LSCr20 exhibits an increase by a factor of ~12 in the course of the experiment.

In Figure 4.1-11, the results of the LSCr20 and YSZ-LSCr10 measurements are compared. Eight temperatures are used and two to three cycles are performed for each temperature, indicated by two or three columns for each T in Figure 4.1-11.At 340 °C, the initial in-plane conductivity of the LSCr20 sample amounts to $1.6*10^{-6}$ S cm^{-1}. The measurement of the YSZ_LSCr10 sample was initiated at 380 °C, with an in-plane conductivity of ~$1*10^{-5}$ S cm^{-1}. At 380 °C, the two specimen have a conductivity in the same order of magnitude. When turning on the UV light, however, the LSCr20 sample reaches a conductivity of $1.6*10^{-4}$ S cm^{-1}, roughly 0.5 orders of magnitude higher than the YSZ_LSCr10 sample. While the YSZ_LSCr10 sample relaxes back to almost the initial value, the LSCr20 sample remains on a by a factor of 5 enhanced level. It appears that the YSZ layer between the single crystal and the LSCr10 thin film causes the significant differences in the conducting behavior. YSZ is known to be a primarily ionic conducting electrolyte material [50, 51]. From this perspective, it might facilitate the balancing of charge and the transport of the whilst illumination incorporated oxygen. The specimen relaxes back near initial in-plane conductivity after every illumination cycle. The initial enhanced in-plane conductivity value of the LSCr20 sample of $1.6*10^{-6}$ S cm^{-1} compared to the pristine sample (~$1*10^{-6}$ S cm^{-1}) is also reasonable, because strontium-doped lanthanum chromite is known to be a better conductor than the STO substrate (5 – 9 S cm^{-1} at 400 °C [49]).

In Figure 4.1-12, the obtained τ values are depicted. While the YSZ_LSCr10 sample exhibits a relatively constant τ over the course of the experiment (in the range of 1000 s), the τ LSCr20 sample increases with every illumination step, from 1200 s at first to 15517 s after the last illumination cycle at 410 °C. This hints towards a chemical altering of the sample (and the LSCr20 thin film) during illumination.

4.1.3.2. YSZ and MgO thin films

YSZ is a wide band gap, oxygen ion conducting semiconductor [50, 51] and MgO is an insulator (both $E_{bandgap}$ > 5.7 eV [52, 53]). They both do not absorb UV light of a wavelength of 365 nm. Thin films of those were chosen to be deposited on STO single crystals, because these layers might act as an oxygen-conducting barrier between the single crystal and the surrounding atmosphere, which might aggravate an oxygen exchange reaction. This should have an impact on both the electric behavior under UV light illumination as well as on the relaxation.

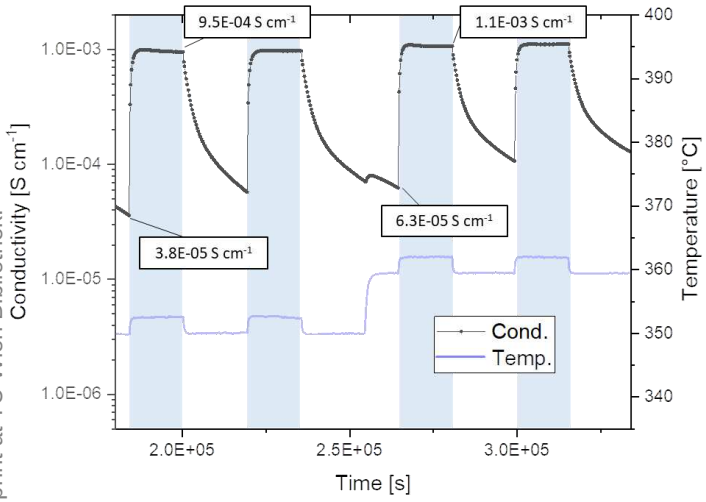

Figure 4.1-13 Results of the measurement of the in-plane conductivity of an STO single crystal with a 200 nm thick layer of YSZ on top at measured 350 and 360 °C in air. Illumination is highlighted with a blue area.

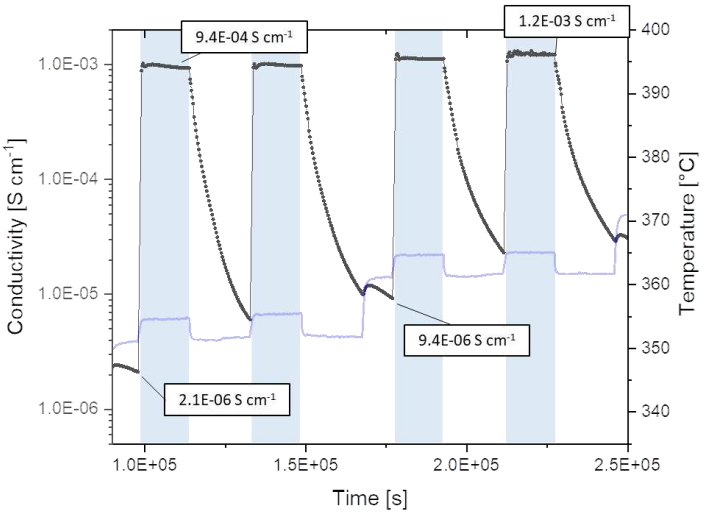

Figure 4.1-14 Results of the measurement of the in-plane conductivity of an STO single crystal with a ~15 nm thick layer of MgO on top at measured 350 and 360 °C in air. Illumination is highlighted with a blue area.

In Figure 4.1-13, the results of the measurement at 350 and 360 °C of a STO single crystal with YSZ layer of a thickness of 200 nm on top are displayed. At 350 °C, it exhibits an in-plane conductivity of ~4*10^{-5} S cm^{-1} before, and an enhanced conductivity of 9.5*10^{-4} S cm^{-1} during UV light illumination. After turning off, it declines continuously, yet does not reach the initial value within the relaxation time of 3.1*10^{4} s and possesses a relaxed conductivity of roughly 6*10^{-5} S cm^{-1}, a factor of 1.6 enhanced compared to before illumination. During every other UV light illumination, it reaches a temperature independent threshold of approximately 1*10^{-3} S cm^{-1} and the curves display a similar shape.

MgO exhibits such a big band gap (5.7 eV [53]), that deposition *via* PLD might only lead to layers, which are only a few nm thin and possibly not dense. An in-plane conductivity experiment with the same measurement parameters as the YSZ sample was conducted, as depicted in Figure 4.1-14. At 350 °C, the specimen initially exhibits a conductivity of 2.1*10^{-6} S cm^{-1}, which is then enhanced due to UV light illumination to 9.4*10^{-4} S cm^{-1}. In the course of the following illumination cycles, the conductivity under UV light illumination slightly enhances to ~1.2*10^{-3} S cm^{-1}. After turning the UV light off, the conductivity after illumination is enhanced by a factor of roughly 2 - 3 compared to before illumination. This also applies for most of the illumination cycles of this sample.

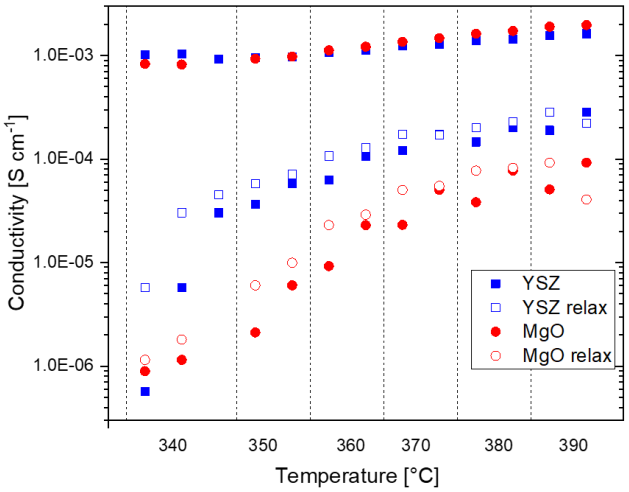

Figure 4.1-15 Comparison of the results of the measurements of an STO sample with a layer of YSZ on top with an STO sample with a layer of MgO on top. The affix "relax" denotes the relaxed conductivity at the end of the relaxation time.

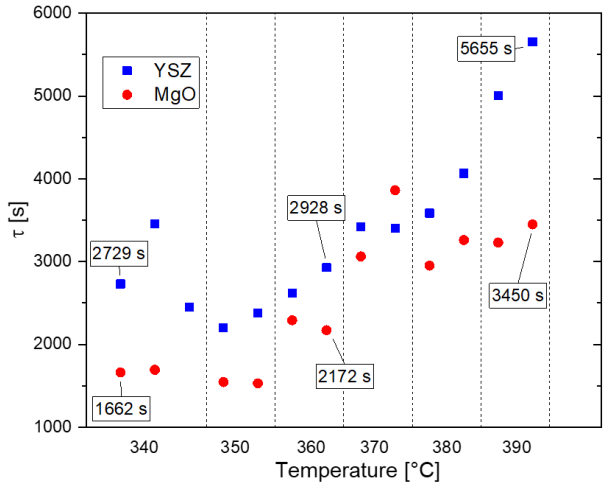

Figure 4.1-16 The time τ, after which the conductivity of the MgO and the YSZ samples decline to a factor of e^{-1} during relaxation, versus temperature. The τ values roughly double for both samples.

In Figure 4.1-15, the results of samples with deposited YSZ and MgO thin films, respectively, are compared. Six temperatures are used and two to three cycles are performed for each temperature. Initially, the MgO sample exhibits higher ($8.9*10^{-7}$ S cm^{-1}) in-plane conductivity than the YSZ sample ($5.7*10^{-7}$ S cm^{-1}) at 340 °C. During illumination, however, the value of the YSZ sample is slightly higher. While the MgO seems to relax to almost the initial state, the YSZ sample exhibits an enhanced conductivity of roughly one order of magnitude after the first illumination cycle. The higher the experimental temperature is, the closer the YSZ-deposited sample relaxes to the state before the cycle.

Remarkably, the sample with MgO on top relaxes to enhanced conductivity after the first illumination cycle of each temperature. The second illumination cycle always leads to a relaxed conductivity closer to the initial one.

After the last illumination cycle at 390 °C, the YSZ sample remains on a conductivity, which is two orders of magnitude higher than before the experiment. The MgO sample gains 1.5 orders of magnitude in conductivity in the course of the whole experiment and a temperature step of 50 °C. Both values account for the observed relaxation time.

The determined τ values of the MgO and the YSZ sample are plotted versus temperature (illumination cycle) in Figure 4.1-16. The YSZ sample exhibits by tendency higher τ (2700 s to 4000 s between 340 and 380 °C, >5000 s at 390 °C) than the MgO sample (1660 to 3500 s). Both samples roughly double their τ values over the course of the experiment (YSZ: from 2729 to 5655 s; MgO: from 1662 to 3450 s).

Since it could not be determined that the deposited MgO thin film is completely dense, the conductivity of the MgO sample (Figure 4.1-15) and the pristine sample (Figure 4.1-7) in air are to be compared: While the conductivity at 340 °C is within the same range (~$1*10^{-6}$ S cm^{-1}), the τ values differ. The τ of the MgO sample is roughly double the size of the pristine sample in air, compare Figure 4.1-16 (MgO, 1660 s) and Figure 4.1-8 (STO, 880 s). Hence, either the MgO thin film is thick enough to influence the sample's

conductivity, or this is the result of the PLD process, where the used UV laser possibly chemically alters the sample.

Due to the presence of an additional layer, the YSZ_LSCr10 sample (Figure 4.1-10, Figure 4.1-11) and the YSZ specimen differ in certain points remarkably. Firstly, the YSZ_LSCr10 sample exhibits an in-plane of $1.6*10^{-6}$ S cm^{-1} compared to the $5.7*10^{-7}$ S cm^{-1} of the YSZ sample. Secondly, the maximum conductivity of the YSZ_LSCr10 sample under UV light illumination is a factor of 2.3 smaller than that of the YSZ sample. These two effects are not surprising, since the LSCr10 top layer might causes the difference, as discussed above. Thirdly, the YSZ_LSCr10 sample exhibits a relaxation to the initial value, while the YSZ sample's relaxed conductivity is up to 1 order of magnitude higher than the initial. This is interesting, because considering the results, the YSZ layer causes facilitated relaxation. However, the comparison of the results of these two samples contradicts that. Apart from that, the YSZ_LSCr10 sample's τ remains constant over the course of the experiment (~1000 s), while the YSZ sample exhibits increasing values, which are 2.7 to 5.7 times higher (~2700 to ~5700 s).

4.1.4. Conclusion of the in-plane conductivity measurements

The findings summarized:

- The results suggest that UV light illumination with a 365 nm LED of an STO single crystal leads to an increase of the in-plane conductivity by several orders by magnitude, independently from the deposited thin film. In the gain of conductivity, photovoltaic and temperature effects only play an negligible role. By far, the increase is mainly caused by the UV light induced oxygen incorporation.

- The surrounding gas atmosphere, namely the oxygen partial pressure, plays a major role. When the atmosphere consists of less oxygen, the specimen takes longer time to reach the maximum conductivity and relaxes faster to the initial value for the oxygen to be released back into the atmosphere.

- The results of the measurement could not provide an Arrhenius relation between conductivity and temperature, because the samples did not reach the required equilibrium state during the measurements. As expected, however, conductivity increases with increasing temperature.

- The in-plane conductivity reaches a temperature-independent threshold during UV illumination. The values revolve around $1*10^{-3}$ S cm^{-1} plus or minus half an order of magnitude. It is also observed at specimens with various top layers such as LSCr, YSZ and MgO.

- Thin films influence the in-plane conductivity: In the case of LSCr20 it enhances the conductivity. A layer of YSZ between the STO single crystal and an LSCr10 layer possibly causes enhanced relaxation. A layer of YSZ alone causes a decelerated relaxation compared to the pristine single crystal. The effect of MgO cannot be determined unambiguously, because of its small thin-film thickness. However, the values differ from the pristine STO single crystal in air.

- The comparison of the τ values illustrates the major differences in the relaxation behavior of the samples.

4.1.5. Mechanistic conclusion

An illustration of the light illumination process from a mechanistic perspective is displayed in Figure 4.1-17.

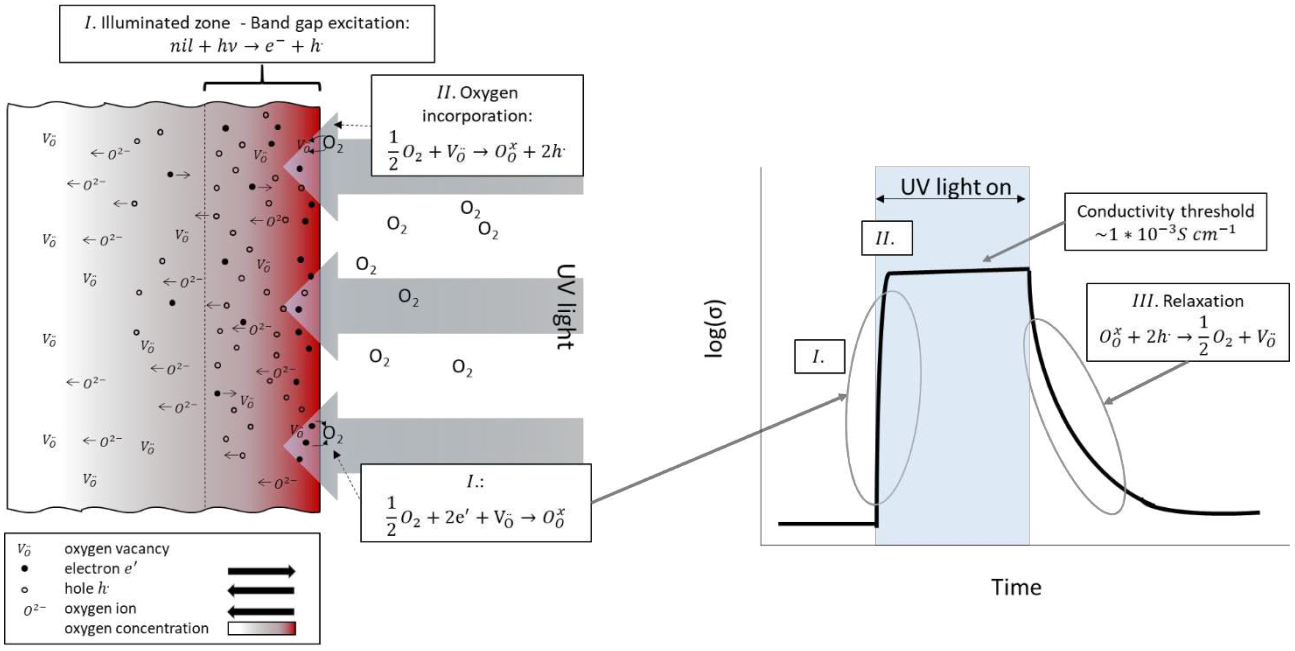

Figure 4.1-17 Illustration of the mechanism of the light effect during an in-plane conductivity experiment.

I. **Photocurrent:** At the moment the UV light penetrates the STO sample, hole-electron pairs are generated. The increased number of electrons leads to an increase of oxygen incorporation into the sample, thereby generating photocurrent, according to

$$\frac{1}{2}O_2 + 2e' + V_O^{\bullet\bullet} \rightarrow O_O^x$$

The UV light causes enhanced migration of oxygen ions away from the STO|air interface, thus altering the material electrochemically with time.

II. **Change of charge carrier concentration due to altered oxygen exchange:** The elevated ion movement to the surface causes additional enabling of elevated oxygen incorporation into the specimen.

$$\frac{1}{2}O_2 + V_O^{\bullet\bullet} \rightarrow O_O^x + 2h^{\bullet}$$

With that, the concentration of holes rises, which results in increased conductivity.
After maximal 30 min of illumination, the conductivity reaches a maximum of about $1*10^{-3}$ S cm^{-1} plus minus half an order of magnitude for every sample.

III. **Relaxation:** After the UV light illumination, "excess" oxygen in the material is released back in the atmosphere, according to

$$O_O^x + 2h^{\bullet} \rightarrow \frac{1}{2}O_2 + V_O^{\bullet\bullet}$$

As a result, the conductivity gradually decreases. Depending on the oxygen partial pressure of the surrounding atmosphere, the relaxation to the initial state takes a shorter at low oxygen partial pressures (equilibration within 8 h at $p(O_2) \approx 10^{-4} bar$), or longer, at higher oxygen partial pressures (only slow relaxation in the course of the relaxation time at $p(O_2) \approx$

$10^0 bar$). Arguably, space charge effects in dependency of the oxygen partial pressure are the reason, making it a surface-limited process.

Since formally undoped STO behaves like a p-type semiconductor at probed conditions [13, 32], it can be assumed that based on the findings of the in-plane conductivity experiments, UV light irradiation leads to a hole conducting type of response in the material. Deposited thin films cannot shift the conductivity from hole to electron conducting.

4.2. SOPEC voltage measurements

Open circuit voltage measurements of YSZ and (Fe:)STO based solid oxide photoelectrochemical cells (SOPECs) were carried out as function of temperature T and oxygen partial pressure $p(O_2)$ while switching UV light on and off. In the following, UV light illumination is indicated with a blue area in the figures.

The SOPEC consisted of Fe:STO or STO thin films deposited on YSZ single crystal substrates, Pt or Au grids acted as current collectors on the illuminated surface. The crucial parameters for the conducted measurements are summarized in Table 3.3-3. The specimens are named x-y, after the thin film (x) and the current collector (y).

4.2.1. Sample preparation

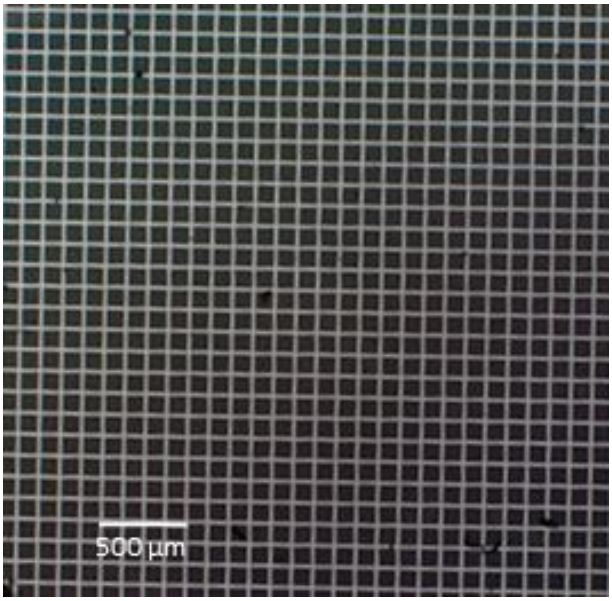

Figure 4.2-1 Microscope image of a SOPEC with Pt grid with a bar width of 25 µm and a mesh opening of 100 µm.

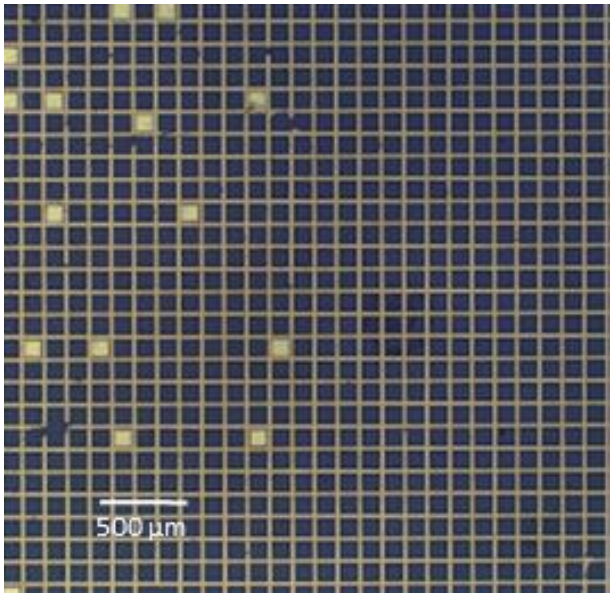

Figure 4.2-2 Microscope image of a SOPEC with Au grid with a bar width of 25 µm and a mesh opening of 100 µm.

Figure 4.2-1 and Figure 4.2-2 display the results of the sample preparation of the SOPECs. Using lift-off photolithography and sputtering, well-defined platinum and gold, respectively, grid structures were established on the substrate. A grid with a bar width of 25 µm and a mesh opening of 100 µm was chosen as pattern. This equals an illumination area percentage of 64 %.

4.2.2. Intial measurements

The first measurements were conducted in order to get an overview of the voltage behavior at different temperatures and in different gas atmospheres during UV light illumination. The discussed measurements were picked exemplarily and their results aided in optimizing the setup and parameters for further measurements displayed in Section 4.2.3. The UV light was mostly turned on and off manually.

4.2.2.1. SOPEC with Fe:STO thin film and Pt current collectors

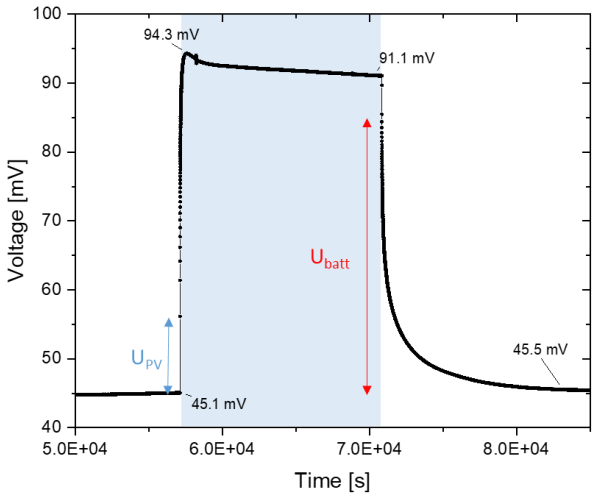

Figure 4.2-3 Results of the measurement of the Fe:STO-Pt sample at 300 °C, in air.

The measurement displayed in Figure 4.2-3 was carried out at 300 °C in air. Within the measurement, the sample was illuminated for $1.4*10^4$ s. Initially, a U_{dark} of 45 mV was measured. When turning the UV light on, the value immediately jumped up by roughly 10 mV and then increased more slowly to reach the peak value after 100 s of illumination. Subsequently, the voltage decreases by 2 mV and exhibits a slightly negative slope during the rest of the illumination. When turning the UV lamp off, the voltage immediately jumps down from 91 mV by roughly 6 mV, to then slowly decrease within ~10^4 s to reach the approximate value of U_{dark} again. The deducted values from the U(t) curve amount to roughly 10 mV for the photovoltage U_{PV} (blue arrow) and roughly 40 mV for the battery voltage U_{batt} (red arrow), as indicated in Figure 4.2-3. It is noteworthy that both U_{batt} and U_{PV} are positive. U_{PV} decreases within the course of the measurement. The first jump up when turning the UV light differs from the jump down when turning the lamp off. The UV light causes a chemical altering of the sample, thus leading to different values.

The samples, which were used in literature [17], typically exhibited a negative photovoltage (Pt samples 0 to -100 mV; Au -180 to -600 mV). However, with this composition, it is positive. The used materials cause the difference: Walch *et al.* used STO single crystal and PLD-deposited YSZ layers. Here, YSZ single crystals and Fe:STO thin films are utilized.

4.2.2.2. SOPEC with Fe:STO thin film and Au current collectors

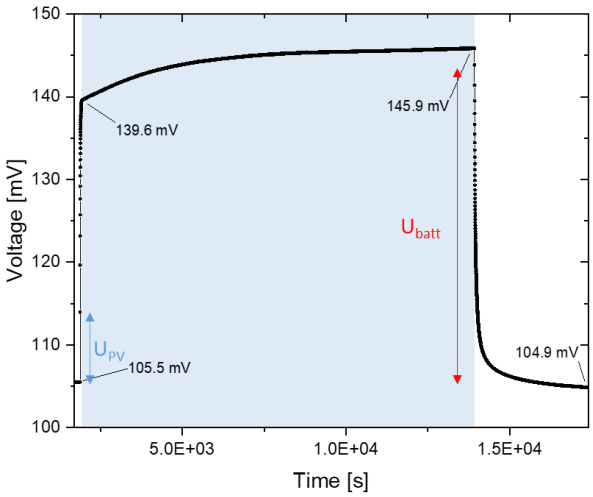

Figure 4.2-4 Results of the measurement of the Fe:STO-Au sample at 350 °C in air. After roughly 7000 s of illumination time, the total voltage remained constant at 145.9 mV, which hints towards a maximum battery voltage.

The measurement depicted in Figure 4.2-4 was conducted at 350 °C in air. When turning the UV lamp on, the voltage jumps up from a dark voltage of 105.5 mV by ~10 mV and then slowly increases to roughly 140 mV after 200 s and increases more slowly during the illumination. After an illumination time of approximately 7000 s, the voltage reaches the maximum value of roughly 146 mV and stays constant until the UV light was turned off. Arguably, the illumination time dependent battery voltage reaches its maximum value after 2 h at latest. The deduced values of U_{batt} of 40 mV and U_{PV} of 8 mV resemble the values of the Fe:STO-Pt sample (see Figure 4.2-3). In both cases, the positive photovoltage is caused by the interface between the Fe:STO thin film and the current collector. Apart from that, the dark voltage amounts to over 100 mV, more than twice as large as the value of the Fe:STO-Pt sample (40 mV). This is typically found at the investigated Au samples.

4.2.2.3. SOPEC with STO thin film and Pt current collectors

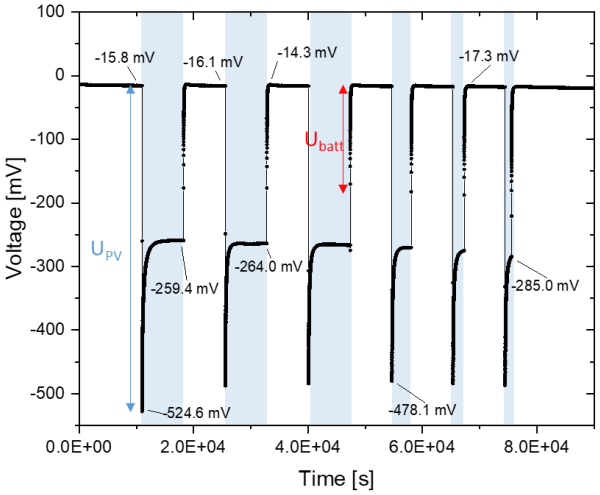

Figure 4.2-5 Results of the measurement of the STO-Pt sample in pure N_2 atmosphere at 350 °C. Negative battery voltages, which are basically constant over the course of the experiment, are observable.

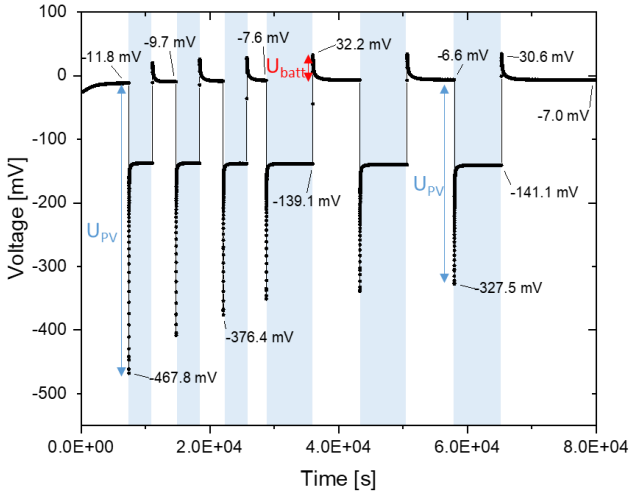

Figure 4.2-6 Results of the measurement of the STO-Pt sample in pure O_2 atmosphere at 350 °C. The sample displays a positive battery voltage in contrast to the measurement on the left.

The two measurements displayed in Figure 4.2-5 and Figure 4.2-6 were carried out at 350 °C, on the same sample, STO-Pt, but in different gas atmospheres. They illustrate the battery voltage dependency on the oxygen partial pressure. In the beginning, the dark voltage amounts to a similar value of ~-12 mV in both cases.

The measurement seen in Figure 4.2-5 in a flow of pure N_2 atmosphere ($p(O_2)=8*10^{-5}$ bar) displays negative battery voltage in every illumination cycle in the range of roughly -150 mV. This indicates that the UV light might causes an enhanced oxygen release at the Pt grid: the electrode facing the light conducting rod exhibits a lower oxygen concentration than the opposing electrode when the UV light is turned off. The remaining excess electrons in the thin-film are then provided to incorporate oxygen from the atmosphere. A negative value results.

The measurement of Figure 4.2-6 was conducted in pure O_2 ($p(O_2)=10^0$ bar) atmosphere. The battery voltages amounts to roughly +25 mV. The positive sign contrasts the previous measurement. Apparently, the oxygen concentration at the Pt grid is higher than at the porous counter electrode and hints towards enhanced oxygen incorporation during illumination due to the abundance of oxygen in the surrounding atmosphere.

These two measurements reveal how the battery voltage can be tuned by modulating the applied gas atmosphere.

4.2.2.4. SOPEC with STO thin film and Au current collectors

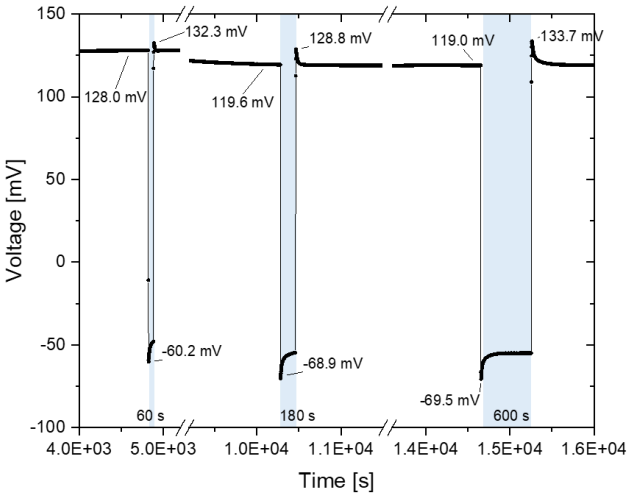

Figure 4.2-7 Results of the measurement of the STO-Au sample, conducted in air, at 350 °C. It illustrates how the battery voltage develops with increasing illumination time. Note the broken axis.

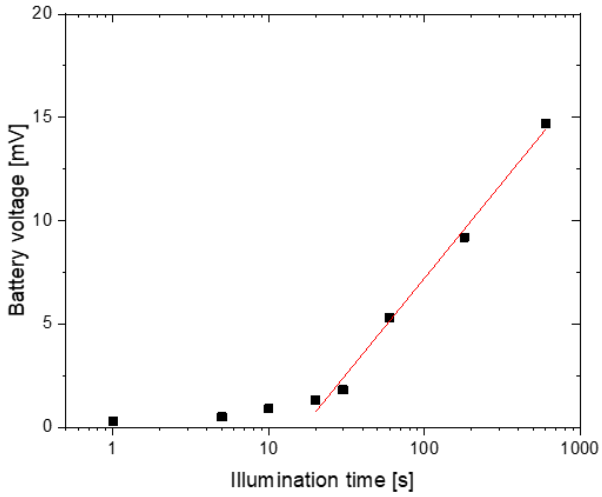

Figure 4.2-8 The measured battery voltage of the measurement displayed on the left, plotted against illumination time. Note the logarithmical scale of time.

The measurement from Figure 4.2-7 illustrates the illumination time dependence of the battery voltage. It was performed in air at a temperature of 350 °C and with an initial U_{dark} of roughly 130 mV. The illumination time and the time between the illumination cycle was increased successively in the course of the experiment to ensure an equilibrium state before the next cycle. From illumination time of 20 s on, the battery voltage increases logarithmically with increasing illumination time as Figure 4.2-8 shows. However, as shown in the measurement displayed in Figure 4.2-4, the samples reach a maximum value U_{batt} after some illumination time (typically after $7*10^3$ s).

4.2.2.5. Conclusion of the initial measurements

The initial measurements leaded to the following new findings:

- Contrary to literature [17] (Pt samples ~ -100 mV at 360 °C; Au -500 to -600 mV 360 °C), positive photovoltages (8 – 10 mV) were obtained from the Fe:STO samples.
- The battery voltage is illumination time-dependent. The total voltage, thus U_{batt} typically reaches constant value after approximately $7*10^3$ s of illumination.
- The battery voltage is oxygen partial pressure dependent. When there is a lack of oxygen in the atmosphere, the battery voltage is negative. In oxygen-rich atmospheres, a positive battery voltage can be obtained. Since the UV light causes an oxygen release/uptake, when it is turned off, oxygen is taken up/released back in the atmosphere to reach an equilibrium state.
- Compared to SOPECs based on STO single crystals and YSZ thin films as electrolyte, only small battery voltages (25 - 40 mV; -125 mV) can be realized (Walch *et al.* >100 - 400 mV in air, at 360 °C). This discrepancy consists due to the reduced STO volume of the investigated cells. Moreover the absorption length in STO is by far larger than the film thickness, consequently only a small portion of the provided UV light is absorbed and plays a role in the process of oxygen incorporation or release.

4.2.3. $p(O_2)$ dependency measurements

The $p(O_2)$ dependency measurements were carried out after basic relations of the light effect on the thin films with gas atmosphere and illumination time were understood in the initial measurements, see Section 4.2.2. It was observed in literature [17, 18] and in the initial experiments that higher temperature leads to lower magnitude of the voltage. Additionally, battery voltage scales with the oxygen partial pressure and after 2 h ($7.2*10^3$ s) of illumination, the voltage remains constant and therefore the battery voltage reaches a maximum. All these findings were taken into account for further measurements. The experimental temperature was either 300 or 350 °C. The oxygen partial pressure was increased gradually seven times, as explained in Table 3.3-2. An automatized trigger switch was used to turn the UV light on and off. The illumination time was fixed at 2 h with 2 h pause between each cycle or after change of partial pressure. During each of these experiments, the UV light was turned on and off twice at each partial pressure.

4.2.3.1. SOPECs with Fe:STO thin films

4.2.3.1.1. Fe:STO thin film and Pt current collectors

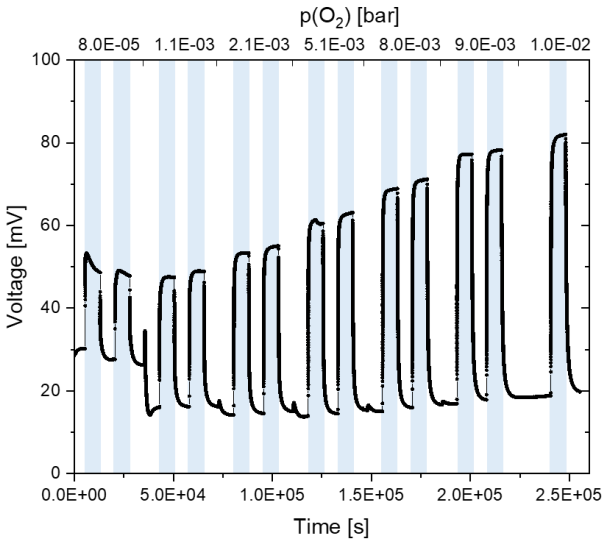

Figure 4.2-9 Results of the $p(O_2)$ dependency measurement of the Fe:STO-Pt sample at 300 °C. Within the course of the experiment, the $p(O_2)$ was increased successively. This resulted in increasing battery voltages.

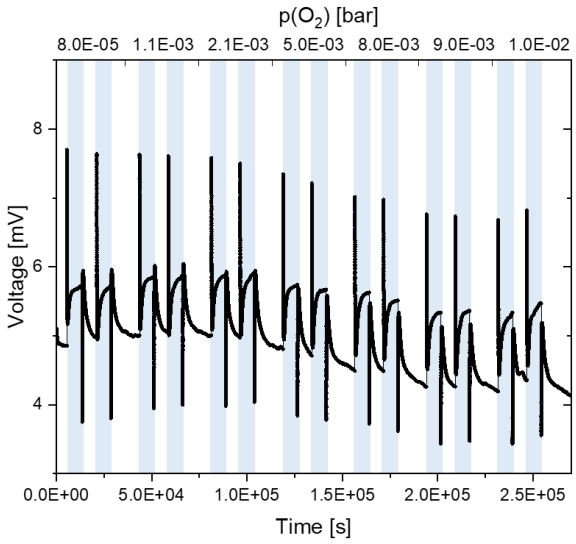

Figure 4.2-10 Results of the $p(O_2)$ dependency measurement of the Fe:STO-Pt sample at 350 °C. The sample responses to the light, but the effect is relatively small. Note the y axis scaling (3 to 9 mV).

In Figure 4.2-9, the results of the voltage measurement of the Fe:STO-Pt sample at 300 °C are displayed. While in pure N_2 atmosphere, U_{dark} amounts to 30 mV, it decreases to 20 mV at the end of the experiment (1 % O_2 containing atmosphere). Each time the partial pressure changes, the dark voltage sharply increases (as seen best after the first two illumination cycles e.g. at around $4*10^4$ s) and then drops within hundreds of seconds. Afterwards, it reaches a constant value. At each partial pressure, the voltage jumps up sharply when turning on the UV light and subsequently gradually increases with illumination time. As explained before, the sharp jump denotes the photovoltaic voltage. An evolving battery voltage and a slight decline of the photovoltage, causes this slow and steady increase. When turning the UV light off, the voltage immediately drops by a similar amount it sharply increased before. The effect of the battery voltage

increases, ranging from 12 to 60 mV, and dominates the voltage change with increasing $p(O_2)$, while the photovoltage basically remains in the same range in the course of this experiment (around 10 mV).

The measurement at 350 °C, seen Figure 4.2-10, contrasts the previous one in the shape of the curve. All the characteristic voltages are in a small range (2 – 4 mV). Once again, a sharp in- and decrease occurs when turning the UV light on and off, respectively. Both the battery and the photovoltaic voltage are in the range of only 2-3 mV. Remarkably, there is still a tendency that the battery voltage increases with increasing $p(O_2)$. In addition, in this case the battery voltage dominates successively. The shape and the magnitude of this curve can be explained by the experimental temperature. Both the battery and the photovoltaic voltage are temperature-dependent, and usually decrease with increasing temperature. Arguably, at 350 °C, the effect of the battery as well as the photovoltaic voltage is on a distinctly low level, in the range of -1 to 3 mV.

4.2.3.1.2. Fe:STO thin film and Au current collectors

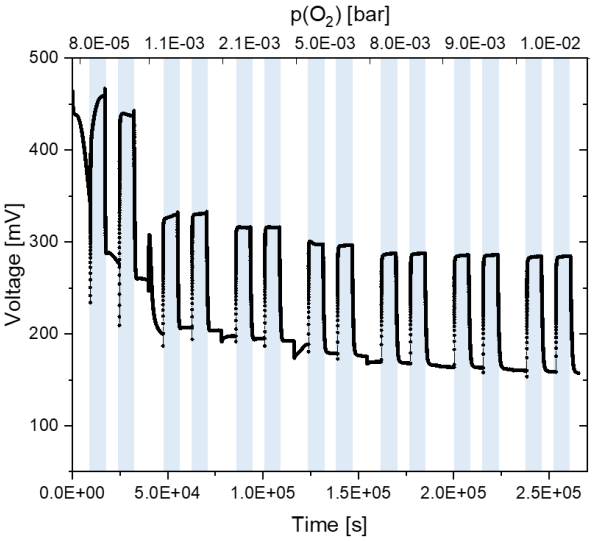

Figure 4.2-11 Results of the $p(O_2)$ dependency measurement of the Fe:STO-Au sample at 300 °C. The battery voltage decreases with increasing $p(O_2)$.

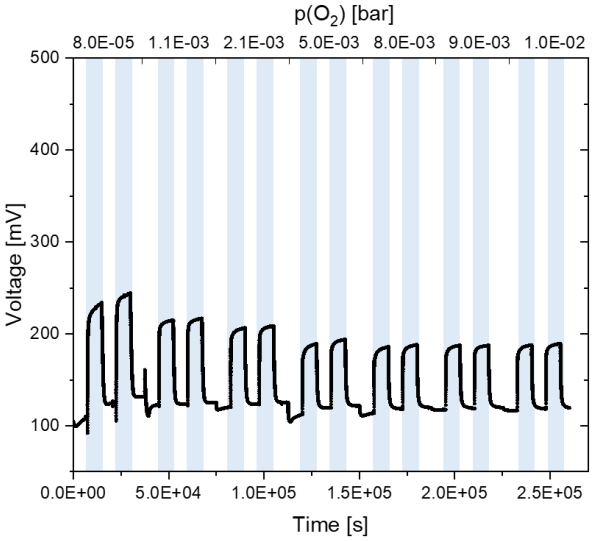

Figure 4.2-12 Results of the $p(O_2)$ dependency measurement of the Fe:STO-Au sample at 350 °C. The battery voltage also decreases with increasing $p(O_2)$, but at a lower level.

In Figure 4.2-11, the results of the $p(O_2)$ dependency measurements of Fe:STO-Au at 300 °C are depicted. Before the first illumination cycle, the sample was not in equilibrium with the surroundings, which explains the sharp decrease of U_{dark} from 450 to 350 mV at the beginning. In the course of the experiment, however, U_{dark} decreases with increasing oxygen partial pressure to ultimately reach a value of roughly 150 mV. The two characteristic voltages of the light effect have different signs: the battery voltage positive while the photovoltage is negative. Apart from that, the partial pressure dependence contradicts the other Fe:STO measurements with a decrease of the battery voltage with increasing $p(O_2)$ and values ranging from 165 (in pure N_2) to 125 mV (in 1 % O_2 containing atmosphere). In comparison to the Fe:STO-Pt measurements, the magnitude of the battery voltage is much higher (compare 12 to 60 mV). Remarkably, the battery voltage decreases almost logarithmically with increasing $p(O_2)$. This tendency is only observed for this sample. Interestingly, the photovoltaic voltage also scales with $p(O_2)$, with a strongly positive U_{PV} in pure

N_2 atmosphere of over 106 and 67 mV, respectively, and positive 28 mV in pure O_2 atmosphere. This was also not observed at any other samples.

The Fe:STO-Au measurement at 350 °C, see Figure 4.2-12, exhibits a similar $p(O_2)$ dependency as the one at 300 °C. U_{dark} ranges from ~100 mV at the beginning (pure N_2 atmosphere) to roughly 120 mV at the end of the experiment ($p(O_2) = 1.0*10^{-2}$ bar). Both U_{batt} and U_{PV} decrease with increasing $p(O_2)$, with values of U_{batt} between 106 to 55 mV, and values of U_{PV} of -18 to 12 mV, respectively. As expected from theory, the light effect is weaker at higher temperature (300 vs. 350 °C).

4.2.3.1.3. Comparison of the battery voltage of Fe:STO-based SOPECs

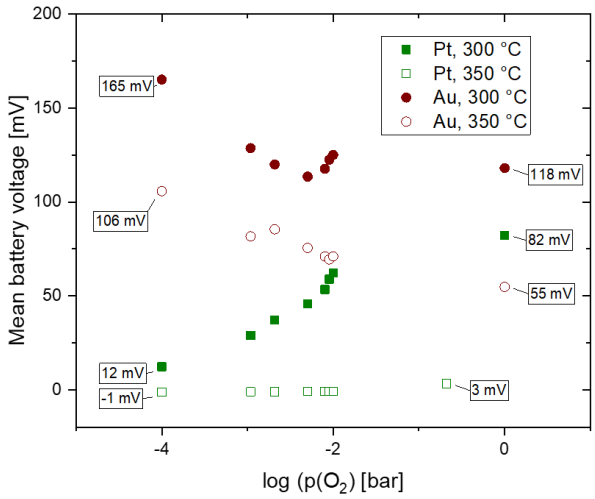

Figure 4.2-13 The two determined battery voltages of each partial pressure averaged arithmetically as a function of the oxygen partial pressure.

In Figure 4.2-13, the results of the systematic $p(O_2)$ experiments of the Fe:STO thin film based SOPECs are compared. They differ both in magnitude and $p(O_2)$ dependence considerably.

- The Pt current collector sample exhibits an increasing battery voltage with increasing oxygen partial pressure, for the Au sample it is the opposite. Here, the battery voltage decreases with increasing $p(O_2)$.
- A further important difference is the magnitude of the battery voltage. The values of the Au sample range from 165 to 118 mV at 300 °C and 106 to 55 mV at 350 °C, while the Pt sample ones only from 12 to 82 mV at 300 °C and -1 to 3 mV, respectively. It is also noteworthy that for the Pt sample at a temperature of 350 °C and at an oxygen partial pressure of $1*10^{-4}$ bar the battery voltage becomes negative (-1 mV).They both have in common that the magnitude decreases with increasing temperature.
- As mentioned above, the atypical light effect behavior (lower U_{batt} values at higher $p(O_2)$) might originate from differences in the work function of the two metals and the thin-film.

4.2.3.2. SOPECs with STO thin films

4.2.3.2.1. STO thin film and Pt current collectors

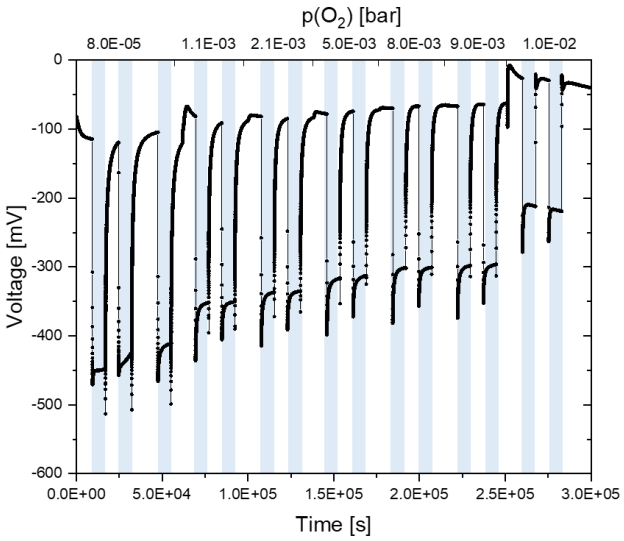

Figure 4.2-14 Results of the p(O_2) dependency measurement of the STO-Pt sample at 300 °C.

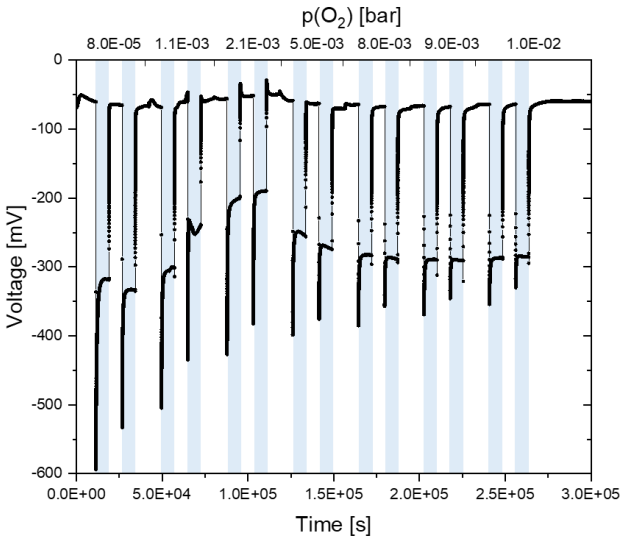

Figure 4.2-15 Results of the p(O_2) dependency measurement of the STO-Pt sample at 350 °C.

The oxygen partial pressure dependence experiment of the STO-Pt sample at 300 °C is displayed in Figure 4.2-14. The measurement starts with a dark voltage of around -100 mV in pure N_2 atmosphere, which evolves to a value of ~-45 mV in 1 % O_2 atmosphere in the course of the experiment. The values of the battery voltage increase from -400 mV in pure N_2 atmosphere to -80 mV in pure O_2 atmosphere. The photovoltaic voltage ranges between values from -211 to -160 mV. Both the photovoltage as well as the battery voltage exhibit negative values. Unlike the Fe:STO-Au sample, the dark voltage exhibits a negative value amounting between ~-100 and -50 mV within the investigated p(O_2) range. This measurement confirms the assumption of a correlation between the battery voltage and the oxygen partial pressure in the investigated range.

At 350 °C, see Figure 4.2-15, the dark voltage remains within in same range in the course of the experiment (roughly -50 mV), and shortly sharply changes when changing the p(O_2). The values of the battery voltage scatter between -250 mV and -25 mV. No strict correlation between U_{batt} and p(O_2) can be observed from the STO-Pt sample measurements at 350 °C. Interestingly, U_{PV} seems to scale with increasing p(O_2), with values between -275 and -160 mV.

4.2.3.2.2. STO thin film and Au current collectors

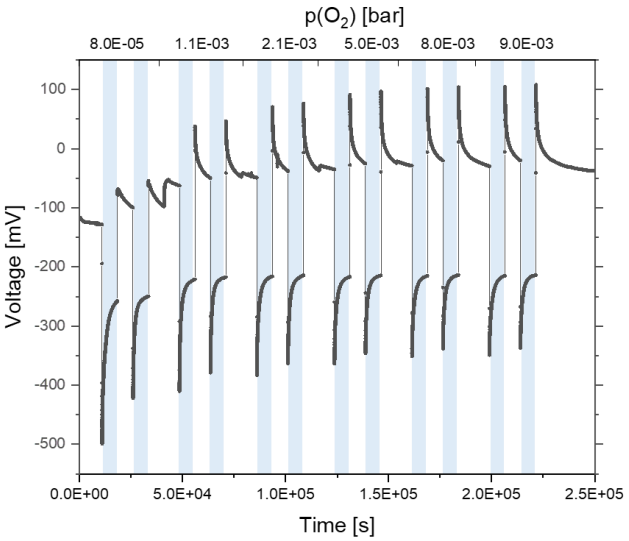

Figure 4.2-16 Results of the $p(O_2)$ dependency measurement of the STO-Au sample at 300 °C.

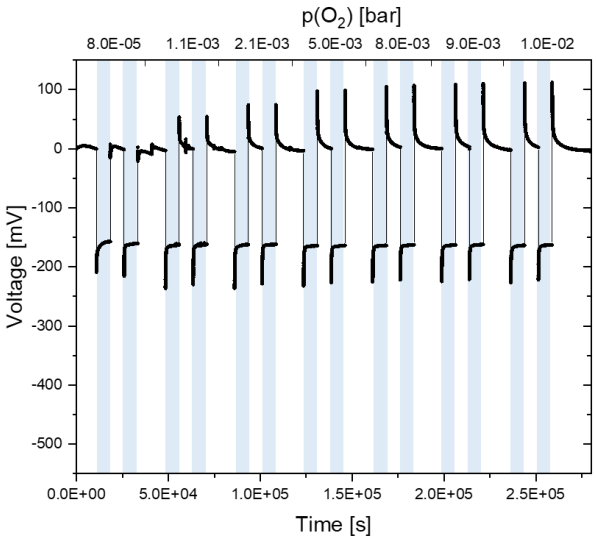

Figure 4.2-17 Results of the $p(O_2)$ dependency measurement of the STO-Au sample at 350 °C.

The results of the STO-Au measurements at 300 °C are depicted in Figure 4.2-16. The dark voltage U_{dark} evolves from roughly -120 mV in pure N_2 atmosphere to ~-50 mV at the highest $p(O_2)$ ($9*10^{-3}$ bar). This goes along with the previous measurements, in which the dark voltage approximates the zero value with increasing oxygen partial pressure. Unsurprisingly, the photovoltaic voltage U_{pv} exhibits no clear relation to $p(O_2)$, with decreasing values ranging from -500 mV to -300 mV. This is also in accord with the previous measurements. The battery voltage U_{batt} remaining with a positive sign in the course of the measurement goes along with the findings of the Fe:STO-Au sample, which also has exclusively positive values. However, with values from 50 to 130 mV increasing with the oxygen partial pressure, it contrasts the Fe:STO-Au sample.

Figure 4.2-17 depicts the results of the STO-Au measurements at 350 °C. In contrast to the measurement at 300 °C, the dark voltage at 350 °C is close to zero at every partial pressure. This is remarkable, because except of the Fe:STO-Pt sample, see Figure 4.2-10, none of the other samples exhibited such a small U_{dark}. The difference might be related to the temperature difference of 50 °C between the two measurements. Apart from that, the measurement at 350 °C complies with expectations due to the measurement at 300 °C: The values of U_{PV} (~200 mV) and U_{batt}, ranging from 6 to 100 mV, are as expected smaller and the battery voltage scales in the same fashion with the oxygen partial pressure.

4.2.3.2.3. Comparison of U_{batt} of the STO based SOPECs

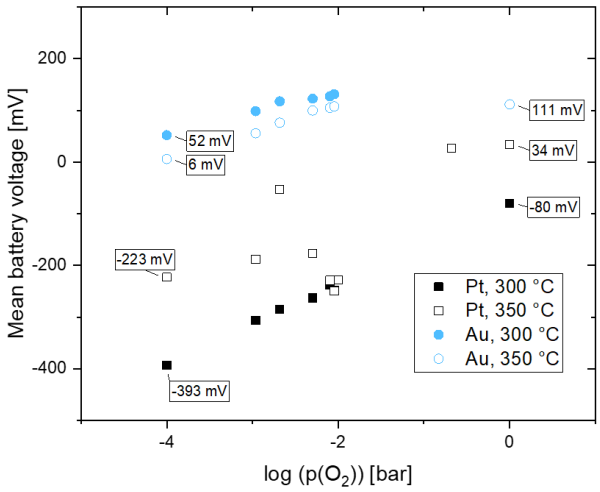

Figure 4.2-18 The two determined battery voltages per partial pressure averaged arithmetically as a function of the oxygen partial pressure.

The results of the battery voltage from the U(t) measurements are displayed in Figure 4.2-18.

- The Pt and the Au sample exhibit battery voltages with different signs. While the Au sample displays positive values at both temperatures, the Pt sample possesses negative values throughout at 300 °C, and mainly at 350 °C. Positive values are only obtained at the highest investigated partial pressures (0.2 and 1 bar).
- The Pt sample delivers surprisingly large values for the photovoltages, ranging from -275 to 160 mV. However, the measurement of the Pt sample at 350 °C was unusually challenging to interpret, and eventually delivered results, which exhibited scattering.
- The Au sample exhibits partly expectable behavior: high pronounced photovoltages (-500 to -300 mV at 300 °C; ~-200 mV at 350 °C), smaller characteristic voltages at higher temperatures, that scale with the oxygen partial pressure [17].
- All the measured battery voltage values obtained from the Au sample are positive.

4.2.4. Comparison of the thin films and conclusion of the voltage measurements

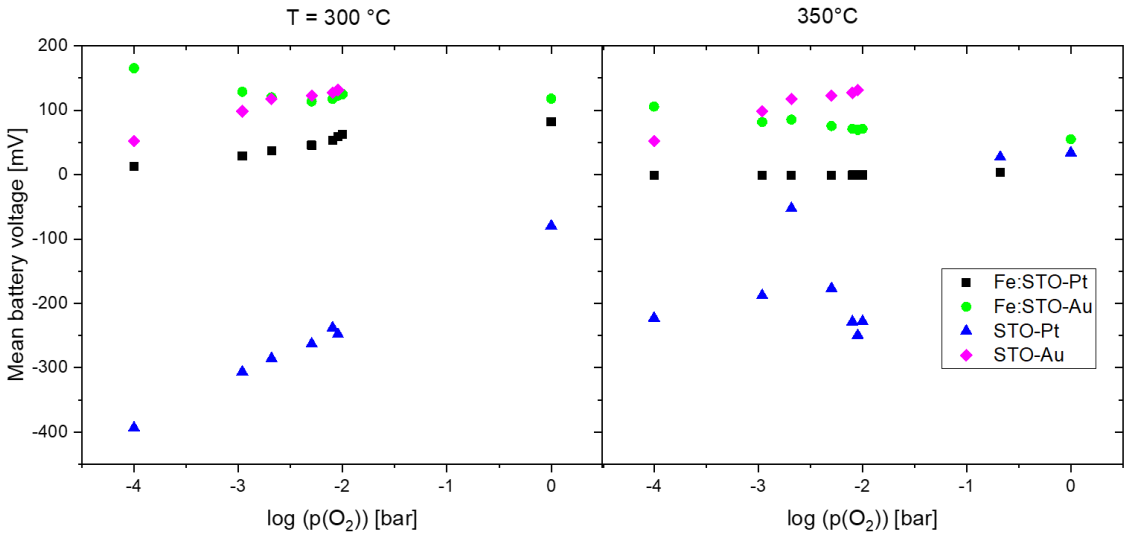

Figure 4.2-19 The battery voltage results of all thin film measurements combined: The two determined battery voltages per partial pressure averaged arithmetically as a function of the oxygen partial pressure, at a) 300 °C and b) 350 °C..

In Figure 4.2-19, all thin film measurements of the systematic oxygen partial pressure dependency measurements are compared and sorted by temperature. Some fundamental tendencies can be observed.

- The battery voltage scales with oxygen partial pressure: While all the other samples show an increase with increasing $p(O_2)$, the battery voltage of Fe:STO-Au is the only that decreases with increasing $p(O_2)$.
- The magnitude of the light effect is temperature dependent: the higher the temperature, the smaller the effect. This accounts for every sample except STO-Au, where the values are almost identical at 300 and 350 °C.
- Fe:STO thin film samples exhibit positive battery voltages at almost every $p(O_2)$ (except Fe:STO-Pt in 80 ppm O_2 at 350 °C, where the light effect arguably collapses). Thus, UV light leads to an enhanced oxygen incorporation into Fe:STO thin-film based SOPECs at oxygen partial pressures above $1*10^{-3}$ bar.
- Against expectations, current collectors have an impact on the battery voltage. STO thin-film specimens with Pt grids on top exhibit at nearly all investigated p(O2) negative battery voltages at 300 and 350 °C. On the other hand, Au grids cause exclusively positive type battery voltages at both temperatures.
- As expected, no distinct relation between oxygen partial pressure and photovoltaic voltage was determined. In theory, the photovoltage decreases with increasing temperature due to the recombination of the charge carriers.
- The dark voltage is oxygen partial pressure dependent, it decreases with increasing $p(O_2)$

4.2.5. *Mechanistic conclusion*

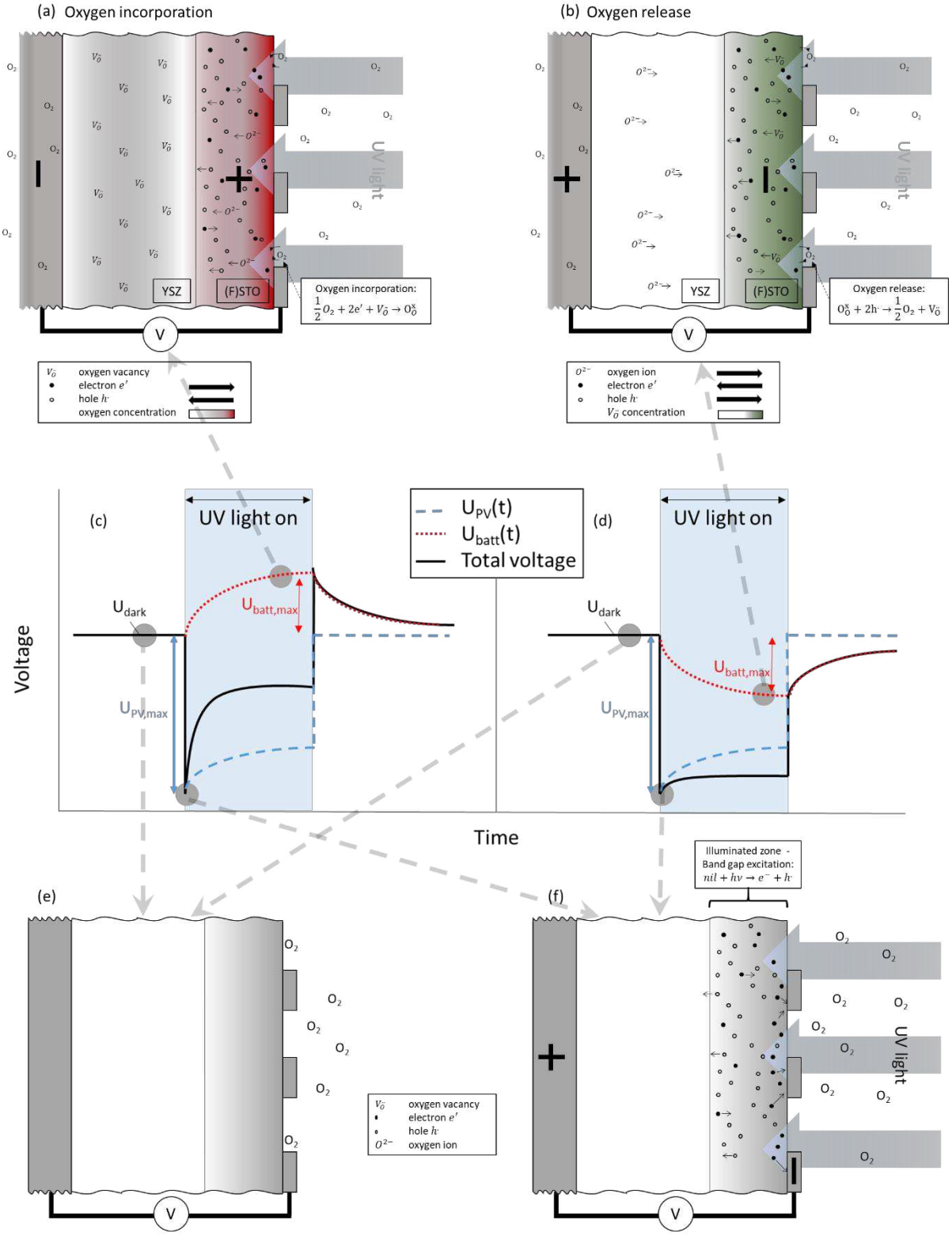

Figure 4.2-20 Schematic illustration of the mechanism of the light effect during a voltage measurement. Both the mechanisms during the measurement and the resulting U(t) curve are illustrated. (e) the SOPEC before illumination measuring U_{dark}, (f) SOPEC exactly when the UV light penetrates exhibiting U_{PV} (for the purpose of clear view, only negative U_{PV} is depicted, however, it can also be positive), (a) and (b) sample during UV illumination exhibiting U_{batt}. (c) and (d) depict typical measurement curves.

The illustration depicted in Figure 4.2-20 schematically sums up the processes the samples undergo during UV light illumination:

Dark voltage U_{dark} (a), depicted in the left bottom: The dark voltage U_{dark} is the constant, measured open circuit voltage of the (equilibrated) sample before UV light illumination. It is typically unequal zero and dependent on temperature and oxygen partial pressure. Different factors might contribute to it, one of them being the distribution of the oxygen concentration over the sample is and how it is equilibrated in the surrounding atmosphere.

The dependency on $p(O_2)$ can be then explained by the gradient of oxygen concentration between the grid electrode and the porous counter electrode. When changing the oxygen concentration in the atmosphere from lower to higher, U_{dark}, a Nernst-type voltage, typically sharply increases. This behavior is demonstrated in most of the systematic measurements, when changing the $p(O_2)$ from 10^{-4} to roughly 10^{-3} bar, at around $4*10^4$ s. Shortly after this increase, the dark voltage reaches a constant value within the following 10^3 s, because the sample gradually equilibrates. The higher the oxygen partial pressure, the less pronounced the effect of changing the $p(O_2)$ on the total voltage is. With increasing oxygen partial pressure, it approximates the zero value.

Photovoltage U_{PV} (b), displayed in right bottom: The measured photovoltage U_{PV} originates from an electrostatic potential step, a Schottky barrier and band bending, between the current collector and the thin film, causing separation of electrons and holes. Consequently a space-charge region is formed [17]. The penetration of UV light into the sample causes the generation of electron-hole pairs, subsequently separated by the space charge region. As a result, a potential difference develops between the grid current collector and the porous counter electrode. Even though it is not explicitly indicated in the illustration, it can also adopt positive values, as seen in the Fe:STO-Pt sample measurements (Figure 4.2-9, Figure 4.2-10).

As mentioned, the magnitude of U_{PV} is mainly governed by the space charge regions in the thin film and the potential step. Pt current collectors samples tend to exhibit lower U_{PV} than their Au counterparts.

U_{PV} is also time-dependent, because the UV illumination alters the charge carrier concentration, thereby changing the composition, the Fermi level and consequently the U_{PV}.

Battery voltage U_{batt} (c) and (d), two upper illustrations: The battery voltage U_{batt} is the result of the penetrating UV light altering the SOPEC, more specifically the thin film, electrochemically. As explained in Section 2.2, the UV light causes a generation of electron-hole pairs, thus enforcing enhanced oxygen incorporation/release. This leads to an oxygen concentration gradient in the cell and accordingly, a development of Nernst-type potential difference between the thin film and porous counter electrode. The longer the sample is illuminated, the longer the material is altered electrochemically. Thus, the battery voltage is time-dependent, but typically reaches its maximum value within 2 h of illumination time, since a steady state is reached in which oxygen incorporation and release is balanced once more. Apart from that, U_{batt} is dependent on temperature and $p(O_2)$.

Positive U_{batt} (left upper illustration): A positive battery voltage develops, if oxygen is incorporated into the (Fe:)STO thin film of the SOPEC. This is the case, when the surrounding atmosphere provides sufficient oxygen. Thus, oxygen can be incorporated according to

$$\frac{1}{2}O_2 + V_O^{\bullet\bullet} + 2e' \rightarrow O_O^x$$

The Fe:STO samples exhibited, bar one measurement (Fe:STO-Pt, at 350 °C and $p(O_2)= 1*10^{-4}$ bar, -1 mV), positive battery voltage at every oxygen partial pressure.

Negative U_{batt} (right upper illustration): A negative battery voltage occurs, when the concentration of oxygen is larger at the porous counter electrode than in the thin film. In low $p(O_2)$, the absence of oxygen in the surrounding atmosphere leads to the holes dominating over the electrons, when they are generated, and oxygen is released according to the rate-determining

$$O_O^x + 2h^{\bullet} \rightarrow \frac{1}{2}O_2 + V_O^{\bullet\bullet}$$

It was observed, that mainly the STO thin-film samples exhibit negative battery voltages.

4.3. Mass change experiments

4.3.1. Premise

To determine mass changes due to change of atmosphere or UV light illumination, the prepared microbalances, as described in Section 2.3, were used. $GaPO_4$ microbalances exhibit dependencies on certain experimental operational parameters, primarily temperature, gas flow and oxygen partial pressure. This results in a frequency drift, a constant change of frequency at constant measurement conditions, which aggravates the interpretation of the frequency plots the most. The first measurements were performed in order to gain an understanding of the setup and optimization of different operational temperatures and gas atmospheres. In the later experiments, calculations were made to derive a mass change as a function of oxygen partial pressure and UV light illumination under optimized conditions (minimization of frequency drift).

The mass change measurements were conducted in either ambient, pure N_2 or O_2 atmosphere or a mixture of these two gas atmospheres, in a temperature range between 350 and 440 °C. In Table 3.4-1, the parameters of the performed measurements are summarized.

4.3.1.1. Sample preparation

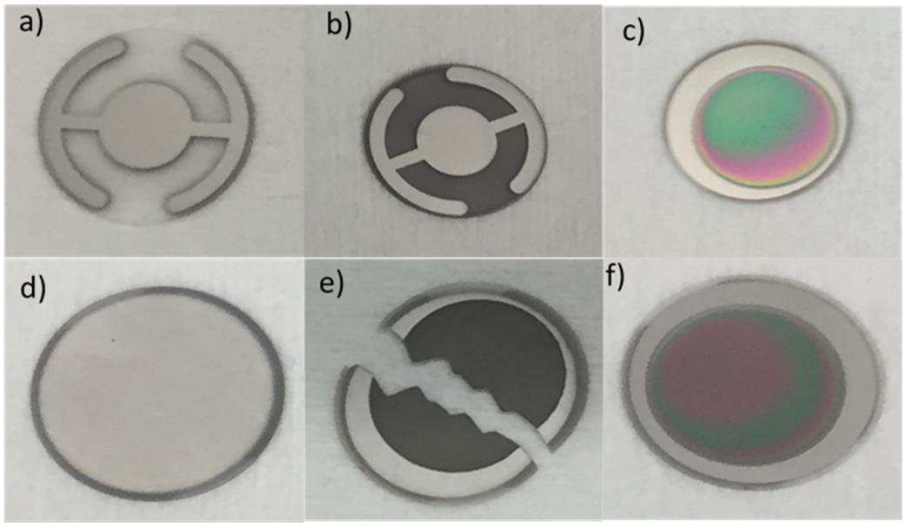

*Figure 4.3-1 $GaPO_4$ microbalances provided by Piezocryst **a)** 0.3 mm thick single crystal with one Pt electrodes on the backside. **b)** 0.2 mm thick microbalance with two Pt electrodes. **c)** 0.2 mm $GaPO_4$ single crystal, two Pt electrodes and Fe:STO thin film on top. **d)** 0.3 mm thick microbalance with two Pt electrodes. **e)** Broken 0.3 mm thick $GaPO_4$ crystal, with Pt electrodes and LSC thin film. **f)** 0.2 mm thick $GaPO_4$ crystal, with two Pt electrodes and STO thin film.*

In Figure 4.3-1, some microbalances used in the reported experiments, such as 0.2 and 0.3 mm thick $GaPO_4$ single crystals with STO, Fe:STO and LSC thin films on top, are shown. The sample in Figure 4.3-1e) broke during cooling phase of the PLD process and consist of a 0.3 mm thick $GaPO_4$ single crystal, two Pt electrodes, and a 415 nm LSC thin film on top.

4.3.2. Temperature dependency measurements

The influence of the experimental temperature on the frequency drift was investigated in the first measurements. The aim was to find the temperature at which the immanent frequency drift is minimal (compare Figure 2.3-2). The first experiments indicated an optimal temperature range between 350 and 450 °C. For kinetic reasons, temperatures lower than 350 °C were not taken into consideration, temperatures higher than 450 °C were expected to lead to an excessive resonance frequency drift.

For the temperature dependency experiments, only $GaPO_4$ microbalances of a thickness of 0.2 mm, with resonance frequencies in the range of 5.5 to 5.6 MHz at the investigated temperatures, were used. As described in Section 3.4, these balances already exhibit a front side Pt electrode. Therefore, no Pt sputtering step was necessary.

4.3.2.1. Pristine 0.2 mm thick $GaPO_4$ microbalance

The temperature dependency measurements of the pristine microbalance with no ceramic thin film upon were all performed on the same microbalance, but in different gas atmospheres (in air and pure N_2 atmosphere) and with different temperature programs.

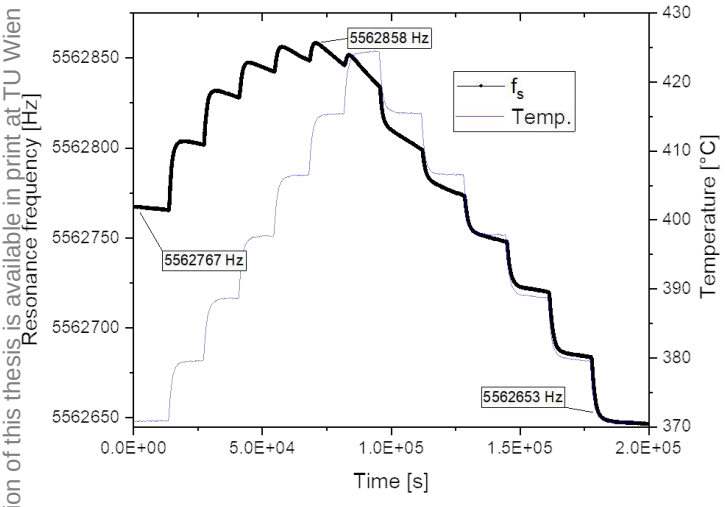

Figure 4.3-2 Results of the temperature cycle measurement in ambient atmosphere. The temperatures range from 370 to 430 °C.

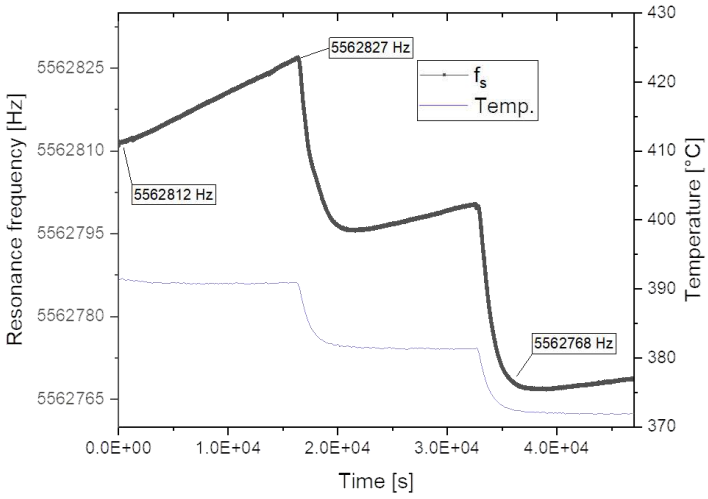

Figure 4.3-3 Results of the temperature dependence measurement of the $GaPO_4$ microbalance in pure N_2 atmosphere.

In the experiment displayed in Figure 4.3-2, the frequency drift in dependency on temperature of a pristine single crystal is investigated. For that purpose, the frequency during application of a temperature program is measured. The experiment starts at 370 °C with set temperature steps of 10 °C, peaking at measured 425 °C and afterwards decreasing to the initial temperature. The initial resonance frequency amounts to roughly 5562767 Hz and the frequency drift to nearly -135 ppm Hz s^{-1}. The frequency increases with increasing temperature, peaking at 415 °C and a value of 5562858 Hz. Exceeding this temperature, the frequency decreases and the drift aggravates at maximum temperature to 1575 ppm Hz s^{-1}. While stepwise decreasing the temperature, the drift also declines. At the end of the experiment, the drift reaches almost the initial value of -135 ppm Hz s^{-1} like the resonance frequency at 5562650 Hz. During the heating phase, the frequency change caused by temperature increase, becomes successively smaller. At the jump from 370 to 380 °C, the frequency step is about 30 Hz, from 415 to 425 °C, it is around 5 Hz.

During cooling, the frequency jump (Δf) successively becomes greater to reach 30 Hz at the step from 380 to 370 °C, the identical value as the first heating step.

The experiment in pure N_2 atmosphere, see Figure 4.3-3, starts at 390 °C with a resonance frequency of 5562812 Hz and a frequency drift of approximately 1000 ppm Hz s^{-1}. After $1.5*10^4$ s, the temperature decreases to 380 °C, which leads to a frequency loss of roughly 30 Hz. At the same time, the drift decreases to 450 ppm Hz s^{-1}. Further cooling steps leads to frequency loss in the same range and decreasing drifts. Interestingly, the sign of the temperature dependent frequency shifts change from +981 ppm Hz s^{-1} at 390 °C to -666 ppm Hz s^{-1} at 360 °C.

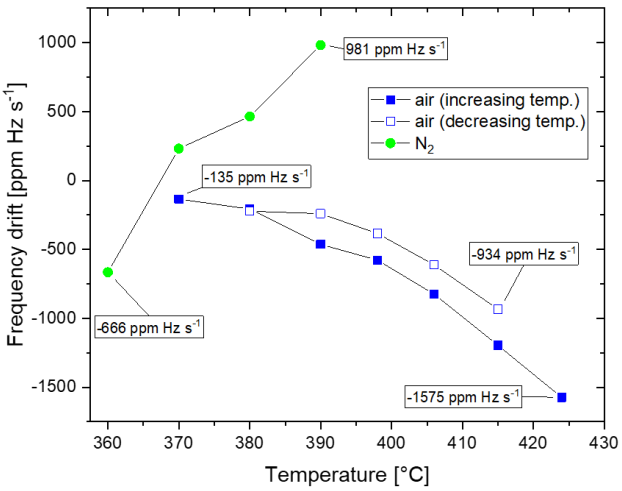

Figure 4.3-4 Comparison plot of the frequency drift of the previous three temperature dependence measurements. Between 370 and 400 °C, the frequency drift is the smallest. Consequently, this temperature range was chosen for further experiments.

The frequency drift denotes the slope of the resonance frequency vs. time plots. In Figure 4.3-4, the drift behavior under ambient atmosphere and in a 40 sccm flow of N_2 at different temperatures are compared.

- Temperatures between 370 and 400 °C lead in air to the smallest frequency drift, temperatures above 405 °C result in excessive drifts. In N_2 decent frequency shifts are obtained at 373 and 381 °C.
- In air, the drifts exhibit negative shifts in the investigated temperature range. This is in accord with the manufacturer's instructions, which also suggest a relative deviation of the resonance frequency in air of roughly -45 ppm Hz s^{-1} at temperatures between 350 and 450 °C [43]. However, the obtained values exceed the literature value by a factor of 3 (-135 ppm Hz s^{-1} at 370 °C) to 35 (-1575 ppm Hz s^{-1} at 415 °C).

As a consequence of these measurements, further experiments were conducted in a temperature range between 370 and 400 °C.

4.3.2.2. 0.2 mm thick $GaPO_4$ microbalance with STO thin film on top

The temperature dependency measurements of a 0.2 mm thick microbalance with a ~220 nm thick STO thin film on top were all performed on the same microbalance, but in different gas atmospheres (in pure O_2 and N_2 atmosphere) and with different temperature programs.

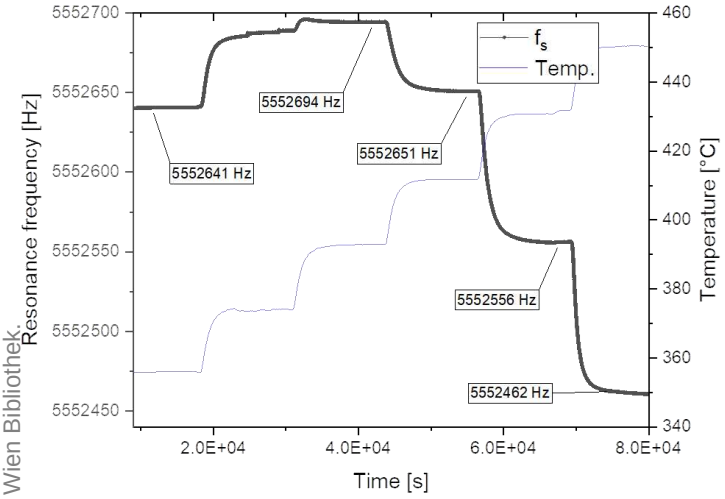

Figure 4.3-5 Results of the temperature dependence measurement of the $GaPO_4$ with an STO thin film on top in pure N_2 atmosphere.

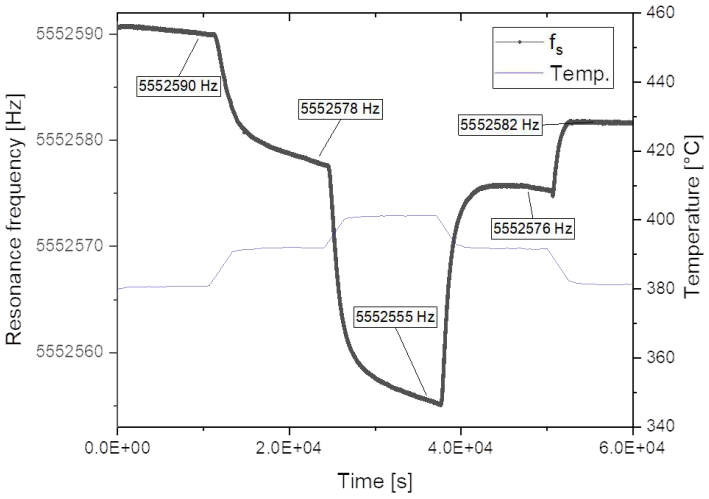

Figure 4.3-6 Results of the temperature dependence measurement of the $GaPO_4$ with an STO thin film on top in pure O_2 atmosphere.

The experiment displayed in Figure 4.3-5 was conducted in order to investigate the temperature dependence of a $GaPO_4$ microbalance with an STO thin film on top in N_2 atmosphere. The initial temperature is 350 °C with 20 °C steps peaking at 450 °C.

At the beginning of the experiment, the resonance frequency amounts to 5552641 Hz and the specimen exhibits a frequency drift of 132 ppm Hz s^{-1} at 350 °C. With increasing temperature, it reaches a maximum of 5552694 Hz at 390 °C with a minimum frequency drift (~-50 ppm Hz s^{-1}) to gradually more negative drifts at higher temperatures, peaking at 450 °C with a drift of -275 ppm Hz s^{-1}. At this temperature, it possesses a minimum resonance frequency of 5552462 Hz. Interestingly, in comparison to the previous measurements of the pristine sample, this sample exhibits less frequency drift over the temperature range from 350 to 450 °C.

Over the whole experiment, the heating step between 370 and 390 °C leads to the smallest frequency shift. The applied temperature steps of 20 °C results in changes of over 20 Hz (except of the step from 370 to 390 °C) and appear to affect the resonance frequency gravely. Consequently, smaller steps were chosen to facilitate interpretation.

The measurement in pure O_2 atmosphere, depicted in Figure 4.3-6, starts at a frequency of in the range of 5552590 Hz. Different temperatures, as well as a different negative initial frequency drift of -78 ppm Hz s^{-1} explain the difference to the starting value of the N_2 measurement (~5552641 Hz). A temperature program of temperatures between 380 and 400 °C with 10 °C steps was applied.

During the first temperature step from 380 to 390 °C, the frequency drops by roughly 10 Hz, aggravating the drift to 277 ppm Hz s^{-1}. When heating to 400 °C, the frequency drops by ~20 Hz and exhibits an increasingly negative drift of -369 ppm Hz s^{-1}. After then decreasing the temperature, the frequency again

gains roughly 20 Hz. The last temperature step leads to a frequency increase by 6 Hz. The frequency drifts at 380 and 390 °C are smaller in the cooling phase than in the heating phase (see Figure 4.3-8). Remarkably, in pure O_2 atmosphere and at a flow of 40 sccm, the sample exhibits a frequency decrease with increasing temperature, that stands in contrast to the measurements in pure N_2 atmosphere. Within the investigated temperature range, the frequency drift remains at a lower level.

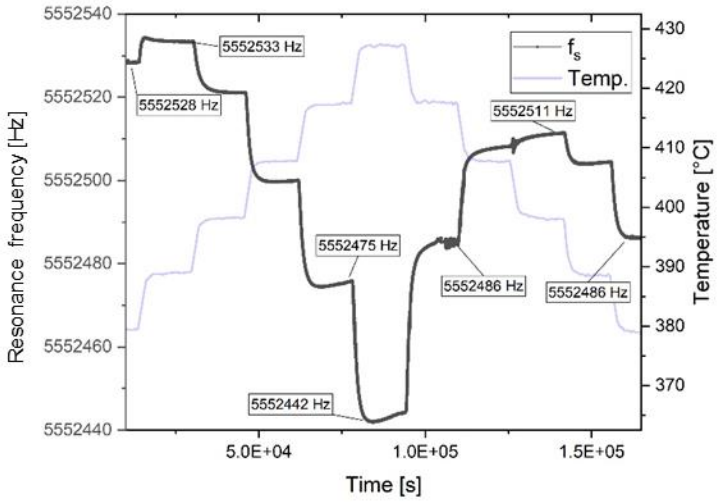

Figure 4.3-7 Results of the temperature dependence measurement of the $GaPO_4$ with an STO thin film on top in vacuum. When decreasing to ~400 °C, the frequency inexplicably curve "collapses" to lower resonance frequencies.

To investigate the impact of the chemical nature of the atmosphere on the frequency drift, a temperature-step experiment was conducted under vacuum conditions, roughly $2*10^{-2}$ mbar, see Figure 4.3-7. The applied temperature program ranges between 380 and 430 °C with temperature steps of 10 °C. At the beginning of the heating phase, the resonance frequency first amounts to roughly 5552528 Hz. The first temperature step from 380 to 390 °C leads to a frequency gain of 5 Hz to the maximum experimental frequency of ~5552534 Hz. The subsequent heating steps from 400 to 428 °C result in a step-wise frequency drop to a minimum of roughly 5552442 Hz at 428 °C with a gradual aggravation of the frequency drift to ~282 ppm Hz s^{-1}. The cooling phase first results in two frequency gains of 35 Hz from 430 to 420 °C and 20 Hz from 420 to 410 °C. After that, the following cooling steps result in a decrease of the resonance frequency. The asymmetrical temperature behavior of the curve was not witnessed before and cannot be explained up to the date of this work.

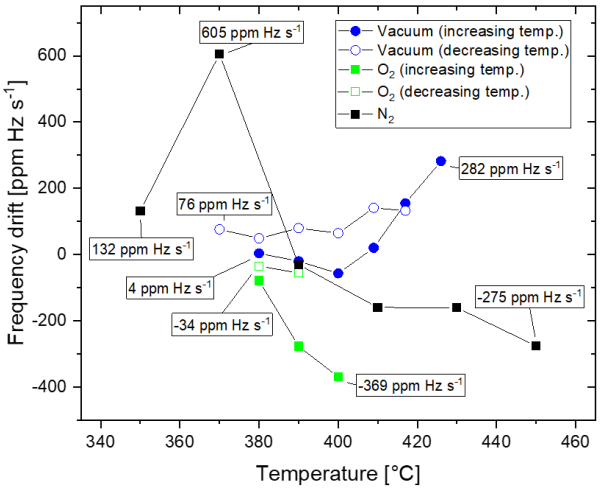

Figure 4.3-8 Frequency drift of the STO thin film sample in different gas atmospheres compared. In the range from 370 to 400 °C, the drift appears to be moderate in each investigated atmosphere

The frequency drifts of the STO sample in O_2, N_2 and in vacuum ($2*10^{-2}$ mbar) are compared in Figure 4.3-8. Again, the temperature range of the least drift is located between 380 and 400 °C.

- While the drift is relatively constant in vacuum, the values in N_2 are in the range of 131 ppm Hz s^{-1} at 350 °C. At 370 °C the drift peaks at 600 ppm Hz s^{-1}, and finally, declines to -275 ppm Hz s^{-1} above 440 °C. In O_2 atmosphere, the sample exhibited negative drifts exclusively, ranging between -34 and -369 ppm Hz^{-1}.
- Increasing the temperature in vacuum leads to an increasing frequency drifts from 76 to 282 ppm Hz s^{-1}. On the other hand decreasing temperatures cause negative drifts below 410 °C, followed by a sharp increase under further heating.

4.3.2.3. Conclusion of the temperature dependency measurements

The temperature dependency measurements delivered important findings for the consecutive measurements.

- The microbalances have a temperature-dependent frequency drift. This drift usually aggravates at temperatures of around 400 °C and upwards. Not only the drift is temperature-dependent, but also the frequency step when changing the temperature.
- The frequency drift is dependent on the gas atmosphere. At each temperature, the magnitude differs in dependence of the surrounding gas.
- The measurement in vacuum (~10^{-2} mbar) indicates that temperature might influence the drift more than the chemical nature of the surrounding gas.
- The frequency drifts in the STO sample measurements do not differ greatly from the drifts of the pristine microbalance sample.

4.3.3. Gas exchange experiments

Ideally, by changing from pure N_2 to pure O_2 atmosphere, the thin film gains weight because of oxygen incorporation into the ceramic thin film and thereby the resonance frequency drops. From this drop, the amount of the incorporated oxygen can be derived. However, the frequency drift massively aggravates the calculation and has to be algorithmically suppressed.

In contrast to the temperature dependence measurements, the gas exchange experiments show that the change of the slope of the frequency curve is caused by the change of the gas atmosphere in the reactor. Different gas atmospheres and, as shown in one experiment, different gas flows amount to differences in the magnitude and sign of the frequency drift.

The first measurements were performed to estimate the influence of the oxygen content of the gas atmosphere and the flow on the drift. Once this was determined, measurements were conducted to calculate the weight gain/loss by oxygen incorporation/release.

4.3.3.1. $GaPO_4$ with STO thin film on top

The gas exchange measurements of the microbalance with a 220 nm thick STO thin film on top were all performed on the same 0.2 mm thick microbalance, but in different gas atmospheres and at different temperatures.

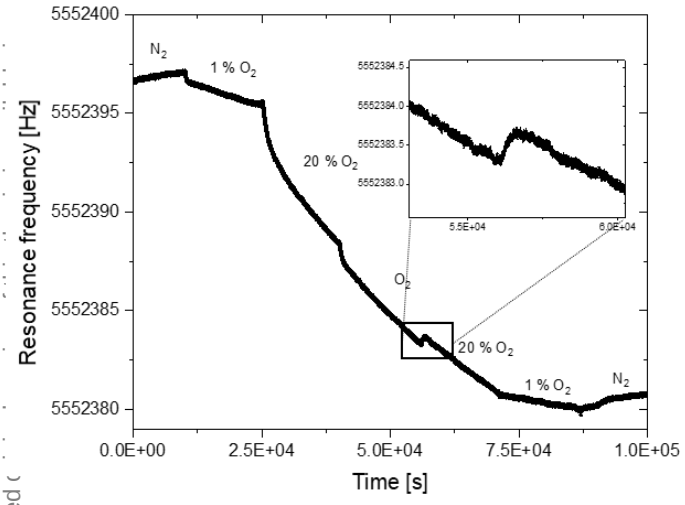

Figure 4.3-9 Results of the gas exchange experiment of the sample with an STO thin film on top at 400 °C. The $p(O_2)$ was changed from 10^{-4} to 10^{0} bar and back. A zoom in of the change of the from pure O_2 containing to 20 % O_2 containing atmosphere can be seen.

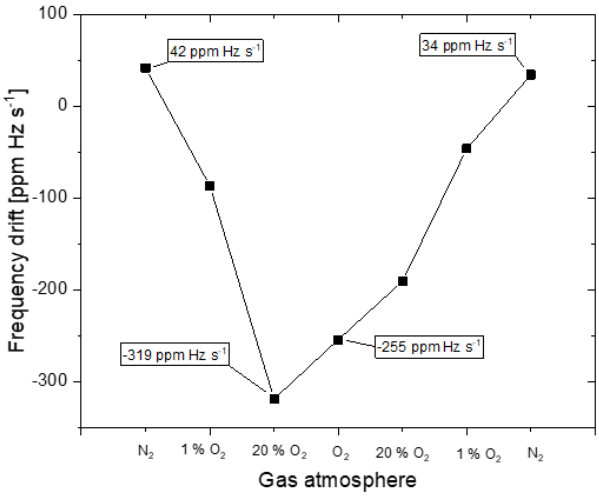

Figure 4.3-10 The drift derived from the curve of Figure 4.3-9 as function of the gas atmosphere. In 20 O_2 containing atmosphere, the frequency drift is the strongest (-319 ppm Hz s^{-1}).

The gas exchange experiment depicted in Figure 4.3-9 was conducted at 400 °C at a flow of 40 sccm and the gas atmosphere was changed every $1.4*10^4$ s. The atmosphere was not only changed between N_2 and O_2, but also an atmosphere containing 1 % O_2, as well as 20 % O_2, was established. The measurement started in pure N_2 atmosphere, successively increasing oxygen partial pressure, over 1 % O_2 and 20 % O_2 containing atmospheres to pure O_2 atmosphere. Afterwards, it was decreased in reverse order.

At each change of atmosphere, the frequency changes distinctly by several tenths of a Hz. This suggests a relation to the chemical nature of the surrounding atmosphere. Accordingly to the expectation that an oxygen-rich atmosphere facilitates oxygen incorporation, thus mass gain, the frequency dropped when the oxygen content is increased and rose when it is decreased. [15]

Only in pure N_2 atmosphere, a positive slope is obtained for the drifts. Under all O_2 containing measurement environments the slopes of the curve are negative. Changing from 1 % O_2 to 20 % O_2 and subsequently to pure O_2 leads to significant jumps in the resonance frequency, whereas the change back from 1 % O_2 to N_2 only causes a change in the curve's slope.

Figure 4.3-10 displays the frequency drifts as function of the different gas atmospheres obtained from the curve of Figure 4.3-9. It is well illustrated that only in pure N_2 atmosphere the slope is positive (increasing $p(O_2)$ 42, decreasing 34 ppm Hz s^{-1}). Contrarily to the expectation that the most oxygen-rich atmosphere exhibits the highest drift, the drift in 20 % O_2 atmosphere when increasing oxygen content is at maximum (-319 ppm Hz s^{-1}). When decreasing the oxygen partial pressure from pure O_2 to 20 % O_2, however, the drift abates (-189 ppm Hz s^{-1}). This directional behavior could not be determined for the other atmospheres, where the drifts when increasing and decreasing $p(O_2)$ are within the same range.

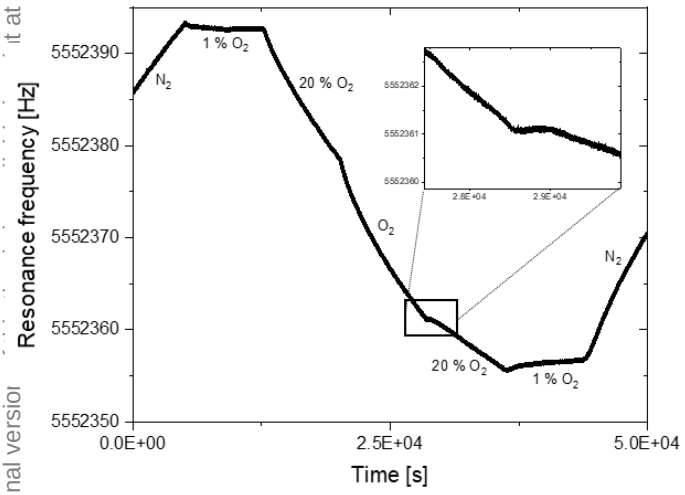

Figure 4.3-11 Results of the gas exchange experiment of the sample with an STO thin film on top at 440 °C. The $p(O_2)$ was changed from 10^{-4} to 10^{0} and back. A zoom in of the change of the from pure O_2 containing to 20 % O_2 containing atmosphere can be seen.

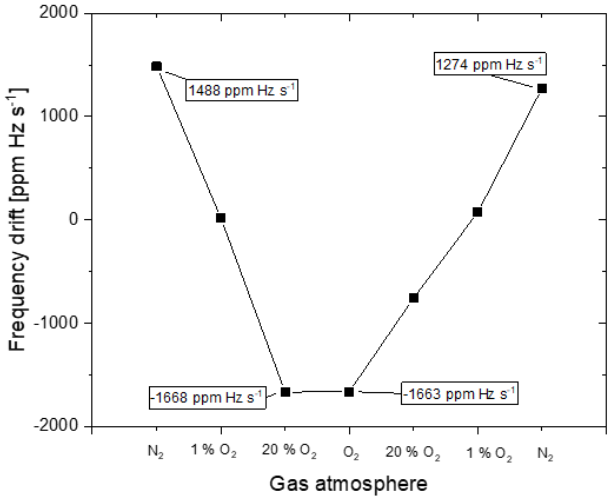

Figure 4.3-12 The frequency drift of Figure 4.3-11 as function of the gas atmosphere. Similar to the measurement at 400 °C, the drift in 20 % O_2 is higher when increasing the oxygen partial pressure than when decreasing.

The experiment depicted in Figure 4.3-11 was conducted at 440 °C at a gas flow of 40 sccm and a gas exchange was performed every 7000 s with a similar premise as in the previous measurement. This measurement also started in pure N_2 atmosphere, and stepwise increasing oxygen partial pressure, over a 1 % O_2 and 20 % O_2 containing atmosphere to pure O_2 atmosphere. Afterwards, it was decreased the other way around. As in the measurement above, each gas exchange step is visible by a fast frequency change by several tenths of a Hz and a change of the drift. Similar to the experiment at 400 °C, the 20 % O_2 atmosphere exhibits the highest drift (-1668 ppm Hz s^{-1}). At this temperature and flow, the frequency drift is as expected higher by a factor of 5 to 10 than at 400 °C. In contrast to the measurement at 400 °C, the

frequency shift at each $p(O_2)$ change is less pronounced, since it is mostly covered by the stronger frequency drifts.

Figure 4.2-12 depicts the frequency drift as function of the gas atmosphere. Again, the drift is only positive in pure N_2 atmosphere, modulating to higher oxygen partial pressures, the drift tilts to negative values. As at 400 °C, when increasing the oxygen content to 20 % O_2 the highest frequency drift (-1668 ppm Hz s^{-1}) is obtained at 440 °C. The same directional behavior as in the measurement above is displayed.

For both of the experiments displayed in Figure 4.3-9 and Figure 4.3-11, the two processes of the frequency change are well visible. On the one hand, at each $p(O_2)$ change, there is a distinct jump in the resonance frequency. In comparison to the measurement at 400 °C, the magnitude of the drifts is by a factor of roughly 5 higher. Determining a change of the oxygen nonstoichiometry would not make sense in both cases given the high frequency drift.

Since the severity of the frequency drift of a $GaPO_4$ microbalance is also influenced by an excessive flow rate, the dependency of the flow rate on the frequency curve and the frequency drift is demanded to be investigated.

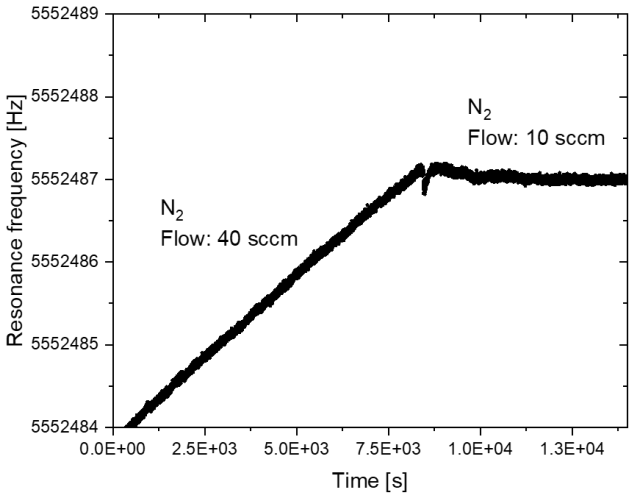

Figure 4.3-13 Results of the flow rate dependence measurement at 400 °C. Different flows were tested during this experiment. Due to the flow change from 40 to 10 sccm, the frequency drift could be minimized from 440 ppm Hz s^{-1} to -17 ppm Hz s^{-1}.

In the experiment displayed in Figure 4.3-13, different flow rates were applied. All previous measurements were conducted at a flow rate of 40 sccm, which was suspected to have a high effect on the frequency drift. Therefore, the flow was changed to lower flows, namely to 10 sccm. Within a few seconds, the drift declines from 440 ppm Hz s^{-1} to -17 ppm Hz s^{-1}. This equals a frequency drift reduction by roughly 96 %. In addition to that, it changes sign from positive to negative. As a result, lower flow rates of 10 sccm were used in most of the following experiments.

While for the first couple of measurements the 0.2 mm thick microbalances were used, it was discovered that the 0.3 mm thick ones exhibit less noise and thus were more suitable for the following measurements, even though they exhibit a lower sensitivity.

For the following experiments, the assumption is emphasized that the investigated thin films are dense and homogeneously thick. This is important, because the oxygen exchange reaction must only occur at the thin film and not at the microbalance itself.

4.3.3.2. $GaPO_4$ with $La_{0.6}Sr_{0.4}CoO_{3-\delta}$ (LSC) thin film

For the reason of testing the measurement setup, a LSC thin film was deposited, as described in Section 3, onto a 0.3 mm thick microbalance. The kinetics of the oxygen exchange reaction in an LSC system have been studied heavily, which is why this ceramic material was chosen [33, 54-56]. The mass change in ng is obtained as explained in Section 2.3.3. The applied gas atmospheres are color-coded in the subsequent figures. Green areas indicate pure N_2, pink areas indicate pure O_2 atmosphere.

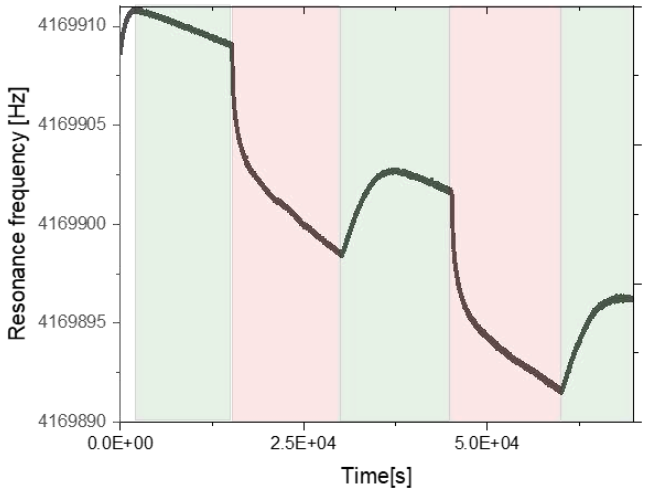

Figure 4.3-14 Results of the first gas exchange measurement of the microbalance with LSC on top at 380 °C. In both gas atmospheres, the frequency drift is negative. The obtained mass changes amount to 43.3 ng when increasing oxygen partial pressure from pure N_2 (green) to pure O_2 (pink) atmosphere (6.1 Hz drop), and 38.4 ng when changing back (5.4 Hz frequency gain).

The experiment shown in Figure 4.3-14 was conducted at a temperature of 380 °C, a flow rate of 10 sccm and in alternating pure N_2 and O_2 atmospheres. At the beginning (white area), the sample initially equilibrates. In pure N_2 atmosphere, it starts at around 4169910 Hz with a change from pure O_2 to N_2 atmosphere immediately before the beginning of the experiment. During the first N_2 phase, the frequency drift amounts to 142 ppm Hz s^{-1}. When changing to O_2, the frequency drops by 6.1 Hz and the drift magnifies by a factor of 2.26 to 321 ppm Hz s^{-1}. This almost identically applies for the second gas exchange cycle.

The obtained frequency jumps from N_2 to O_2 are in the range of 6.1 Hz, the mass gain of the thin film amounted 43.4 ng. From O_2 to N_2 the frequency changes are in the range of 5.4 Hz (38.4 ng).

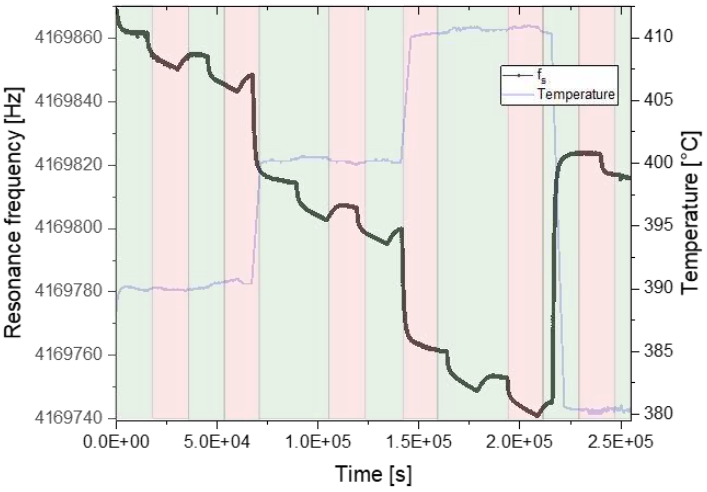

Figure 4.3-15 Results of the gas exchange measurements of the LSC sample with temperature steps.

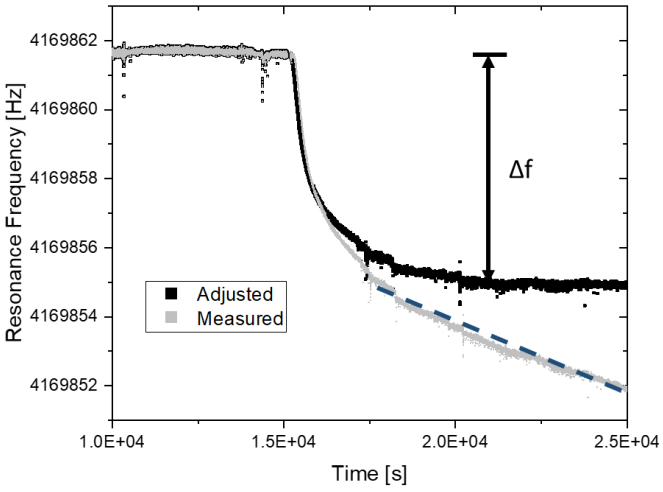

Figure 4.3-16 "Adjusted" frequency curve (black) of the first gas atmosphere change of the experiment depicted in Figure 4.3-15 ($N_2 \rightarrow O_2$). The measured curve (grey) is depicted for comparison. The algorithmically eliminated frequency drift is indicated with a dashed line.

Figure 4.3-15 depicts the results of a gas exchange measurement at a flow rate of 10 sccm with 10 °C temperature steps, and temperatures ranging from 390 to 410 °C. Within every temperature, the gas atmosphere was changed from N_2 to O_2 and back twice.

As in previous segments, the resonance frequency decreases with increasing temperature. In both atmospheres, the frequency exhibits a negative drift and is in O_2 a factor of roughly 2 higher than in N_2. The frequency dropped sharply by between 6.7 Hz at 390 °C and 7.0 Hz at 410 °C every time the atmosphere was changed from N_2 to O_2. Respectively, it increased by roughly 5 Hz when changing from O_2 to N_2. In the temperature range, the obtained frequency jumps hardly depend on temperature and are reproducible.

Figure 4.3-16 illustrates the adjusted (black) and the measured (grey) curve of the first gas exchange from N_2 to O_2 atmosphere in Figure 4.3-15 after roughly 1.5 10^4 s. "Adjusted" means that the frequency drift before and after gas switching is mathematically eliminated from the curve. Compared to the measured curve, the actual frequency change Δf due to gas exchange can be determined more accurately. Therefore, Figure 4.3-16 just illustrates the attempt.

The resulting mass gain of switching from N_2 to O_2 is in the range of 47 to 49 ng, changing from O_2 to N_2 results in a mass loss of 34 to 38 ng. The gas exchange from O_2 to N_2 is typically harder to quantify, since decreasing the oxygen content in atmosphere takes to a greater extent more time than increasing it. In Table 4.3-1, the results of the mass change experiment are summarized. Only the changes from N_2 to O_2 are considered. The increase of O in the thin film was determined by obtaining the molar increase of oxygen Δn_O and dividing it by the amount of oxygen in the thin film $n_{O\ in\ thin\ film}$. Δδ was calculated according to equations (27) to (29).

Table 4.3-1 Results of the gas exchange experiment from Figure 4.3-17. Only jumps from N_2 to O_2 atmosphere were considered.

Jump	Δf [Hz]	Δm [ng]	Increase of O in thin film $\left(\frac{\Delta n_O}{n_{O\ in\ thin\ film}}\right)$ [‰]	Δδ [10^{-2}]	Temperature [°C]
1	-6.93	49.3	3.9	1.2	391
2	-6.88	49.0	3.8	1.1	
3	-6.95	49.5	3.9	1.2	400
4	-6.84	48.7	3.8	1.1	
7	-6.72	47.8	3.7	1.1	411
8	-6.72	47.8	3.7	1.1	

The increase of oxygen in the thin film amounts to 3.7 to 3.9 ‰ in the course of the experiment. Since for the determination of the absolute nonstoichiometry, many assumptions have to be made (e.g. in pure N_2 atmosphere none of the vacancies caused by doping are filled), it is more reasonable to determine its change Δδ.

While there is no source that investigated this composition of LSC in the same temperature interval (653 to 673 K), source [54] gathered data (TGA, coulometric titration) for similar composition ($La_{0.7}Sr_{0.3}CoO_{3-\delta}$) for temperatures higher than 1100 K. At this temperature, they found δ values of 0.08 to 0.10 at low partial pressures (~1 to 2.5*10^{-2} bar). For $La_{0.4}Sr_{0.6}CoO_{3-\delta}$ at 673 K, they found δ values of ~0.1 at ~10^{-2} bar. These values are within the range of this work's finding, assuming that the nonstoichiometry by this doping is roughly 0.08 to 0.12 (as source [54] also suggests, however at 1373 K in air). Then, the gain of oxygen in the thin film would lead to a new δ, which would also be within this range. However, it must be considered that with increasing Sr content, the potential value of δ increases [54]. Source [33] obtained a δ value of around 0.1 to 0.14 at 380 to 400 °C for a composition of $La_{0.4}Sr_{0.6}CoO_{3-\delta}$, which would also be within this range.

4.3.3.3. 0.3 mm thick $GaPO_4$ with Fe:STO thin film on top

A 0.3 mm thick microbalance with 400 nm Fe:STO thin film was used to derive a mass change for the gas exchange experiments. One of these was picked exemplarily to calculate the mass change as explained in Section 2.3.3.

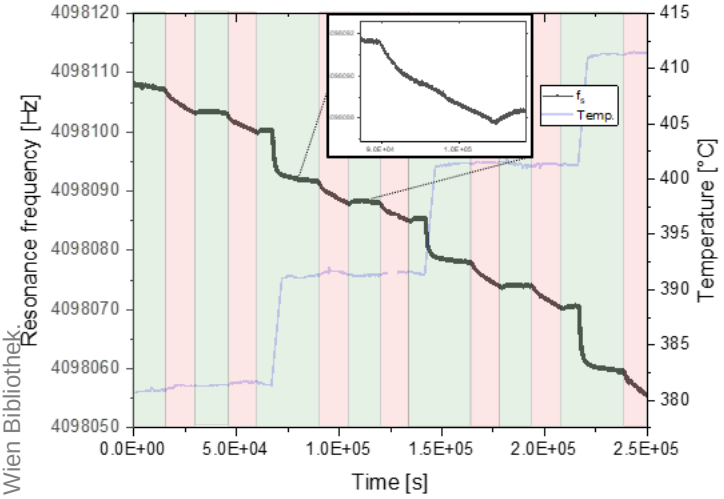

Figure 4.3-17 Results of the gas exchange measurements of the Fe:STO sample with temperature steps.

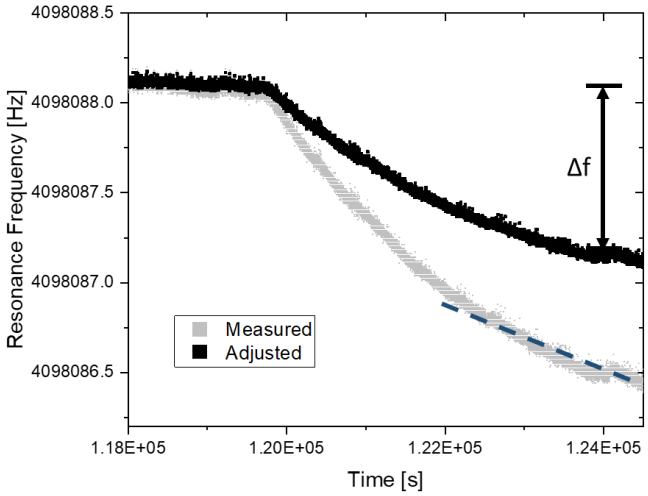

Figure 4.3-18 Frequency curve around the p(O_2) change from N_2 to O_2 at 393 °C, where the frequency drift is algorithmically eliminated. The changes are in the range of tenths of a Hz. The algorithmically eliminated frequency drift is indicated with a dashed line.

The experiment depicted in Figure 4.3-17 was performed with similar experimental parameters as in the experiment from the previous Section 4.3.3.2, see Figure 4.3-15. It was carried out in a temperature range from 380 to 410 °C with a step size of 10 °C. During each temperature, the atmosphere was changed from pure N_2 to pure O_2 twice. Before the temperature step, the atmosphere was changed from O_2 to N_2 again.

The mass change as well as the filled vacancies were calculated according to Schröder *et al.* [21], see Section 2.3.3. The investigated thin film $SrTi_{0.98}Fe_{0.02}O_{3-\delta}$ consists of STO with 2 % Fe doping relative to Ti. As described in Section 2, this amount of Fe creates to 1 % oxygen vacancies and a maximum δ of 0.01. Applying an oxygen-rich atmosphere results in filling of vacancies and a reduction of δ. Only gas jumps from N_2 to O_2 were considered for the calculations. This choice was made, because it takes longer for the oxygen partial pressure to decrease (O_2 (p(O_2)=1 bar) → N_2 p(O_2)= 8*10^{-5} bar)) than to increase (N_2 → O_2). Calculating a mass loss for the immediate frequency change from O_2 to N_2 would result in a distorted value. It would be necessary to derive the frequency change after a longer time than possible in the experiment to obtain the true value.

To exclude errors, the frequency jump was corrected by the drift in the respective atmospheres, as seen exemplarily in Figure 4.3-18 and summarized in Table 4.3-2. In comparison to Figure 4.2-16, the frequency shift is much less pronounced at the Fe:STO sample. This is in accord with the expectation, since iron-doped STO immanently contains less oxygen vacancies to be filled, and thus, cannot gain as much mass as the LSC sample.

Table 4.3-2 Results of the gas exchange experiment from Figure 4.3-17. Only jumps from N_2 to O_2 atmosphere were considered.

Jump	Δf [Hz]	Δm [ng]	Percentage of filled vacancies [%]	δ [10^{-3}]	Temperature [°C]
1	-1.16	8.5	30.8	6.92	381
2	-0.99	7.3	26.2	7.38	
3	-1.17	8.6	31.1	6.89	391
4	-0.87	6.4	23.0	7.70	
5	-1.09	8.0	28.8	7.12	401
6	-0.94	6.9	25.0	7.50	
7	-1.11	8.2	29.6	7.04	411
8	-1.07	7.9	28.5	7.15	

The results are summarized in Table 4.3-2. At each temperature, the first frequency jump is significantly higher than the second. A reason for this might be that after the first jump, some of the oxygen vacancies might have already been filled, so less oxygen can be incorporated. Furthermore, all the first jumps and the second jumps are within the same range.

The obtained frequency losses in the range of 0.87 to 1.17 Hz equal a mass gain in the range of 6.4 to 8.5 ng. Therefore, 23 to 31 % of the present vacancies in N_2 are filled by changing the atmosphere to pure O_2. The obtained values for the oxygen nonstoichiometry δ are in the range of 0.007 and appear to be in a reasonable magnitude.

4.3.3.4. Conclusion of the gas exchange experiments

To conclude, the following findings were made:

- The used microbalances are able to detect changes of applied gas atmospheres. This can either be determined by a change of frequency drift or a frequency shift.
- The flow rate of the applied gas atmosphere plays a major role in the frequency drift.
- The LSC gas exchange experiments leaded to reproducible results, which were all within one magnitude at each temperature. The gain of oxygen in the thin film of around 3.7 to 3.9 ‰ and the obtained resulting oxygen nonstoichiometry change in the range of 0.01 appear to be reasonable.
- Reasonable results of the determination of the oxygen nonstoichiometry in the gas exchange experiments of the Fe:STO thin film sample in the range of δ=0.007 were achieved.

4.3.4. Light illumination experiments

Due to reproducibility, all light illumination experiments were carried out on 0.3 mm thick microbalances. At first, it was investigated how gravely the heating due to illumination by the UV lamp would influence the measurements. Afterwards, the response of a microbalance with no ceramic thin film upon to UV light illumination was determined. The subsequent measurements were used to derive mass changes of a Fe:STO thin film caused by irradiation. In the subsequent figures, light illumination is indicated by a light blue area.

The temperature change during illumination was investigated in order to estimate the frequency change that is caused by temperature effects. It is crucial to distinguish between light and temperature effects. Consequently, a measurement was performed with a Pt100 resistance glued with Pt paste onto a pristine YSZ single crystal and placed at the spot of the sample from the measurement setup from Figure 3.3-2 opposing the quartz rod. The resistance was measured and used to calculate the resulting temperature ΔT_{result}. This value was then compared to the value obtained from the thermocouple. Illumination time and distance of the quartz rod to the sample were varied in the course of the experiments. The results are presented in Table 4.3-3.

Table 4.3-3 Results of the temperature determination via Pt100. The actual temperature differences differ from the displayed value by a factor of 1.5 and more.

Illumination time [s]	Distance [cm]	ΔT_{result} [°C]	$\Delta T_{thermocouple}$ [°C]	Relaxation to initial T [10^3 s]
840	1	6.7	1.8	1.0
2160	1	6.8	3.3	1.2
1620	2	4.4	1.7	1.0
2160	2	3.6	2.3	1.1

From the results as displayed in Table 4.3-3, it was observable that the temperature differences measured by the Pt100 resistance differ from the temperature increase measured by the thermocouple by the factor of 1.5 to 2. In the course of these experiments, the temperature did not rise significantly after an illumination time of 1200 s. After turning the lamp off, the temperature relaxed back to the value before turning on within 1.0 to 1.2 10^3 s. Despite the measurement, the temperature is still believed to have a higher heating effect than it could be observed in this experiment. To be on the save site, a factor of 2-2.5 of the measured ΔT_{result}, hence, an increase of 10 to 15 °C during an illumination cycle is assumed.

4.3.4.1. 0.3 mm thick $GaPO_4$ microbalance

The experiments of the 0.3 mm thick $GaPO_4$ microbalance were conducted to estimate the influence of the UV light on microbalances with no ceramic thin film upon. Like in previous experiments, a 200 nm thick Pt layer was sputter deposited on top of the $GaPO_4$ crystal to secure a sufficient electronic contact

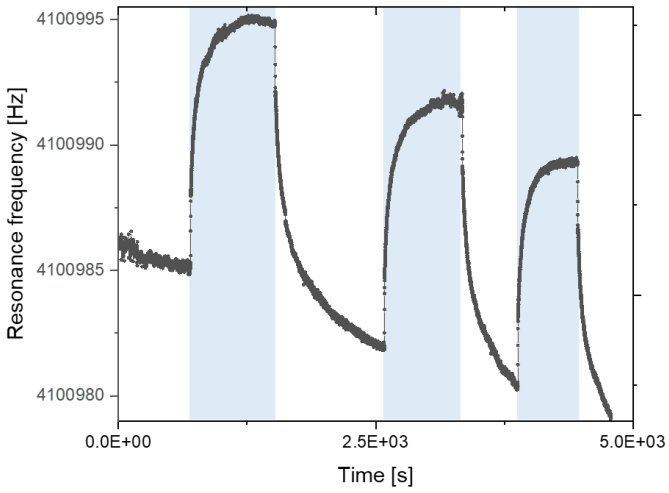

Figure 4.3-19 Results of the first illumination experiment of a pristine, 0.3 mm $GaPO_4$ at 380 °C in pure O_2 atmosphere.

In Figure 4.3-19, the results of the first light illumination experiment of a 0.3 mm thick microbalance at 380 °C in pure O_2 atmosphere are displayed. The frequency jumps up by roughly 10 Hz during each illumination, while the measured temperature increases by roughly 2.5 °C. Ideally, the frequency shifts only as a temperature effect due to heating of the sample. This experiment does not suggest else.

After turning off the UV light, the frequency is expected to decrease to the initial state. However, the frequency declines with declining temperature to a value lower than the initial value. Additionally, the drift appears to aggravate with each illumination cycle. Arguably, the relaxation time after the illumination is too short to let the sample fully relax and equilibrate.

4.3.4.2. $GaPO_4$ with Fe:STO thin film on top

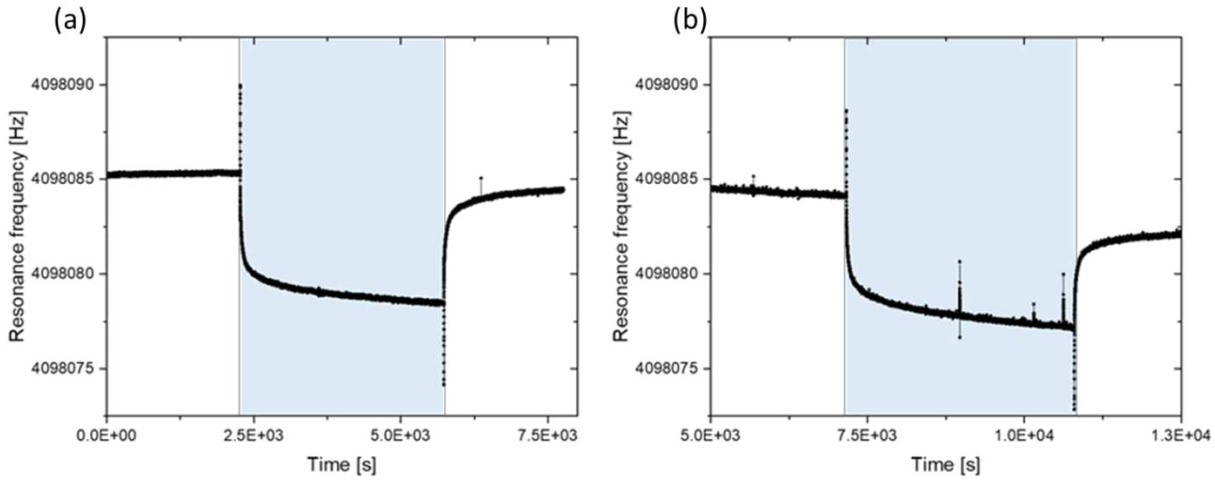

Figure 4.3-20 Results of the illumination experiment in a) pure N_2 atmosphere and b) pure O_2 atmosphere, conducted at a temperature of 380 °C. The curves resemble, the drift is higher in O_2.

In Figure 4.3-20, typical light illumination experiments in pure N_2 (a)) and O_2 (b)) atmosphere are displayed. At 380 °C, UV irradiation leads to a sharp frequency jump up about 5 Hz followed by a decline of the resonance frequency, which was not observed at samples with no ceramic thin film upon. Immediately after that, the frequency drops 10 Hz, to approximate an almost constant value and drift during 1 h of illumination. When turning the light off, the frequency drops by the same amount it increased when the UV was turned on.

At least two convoluted effects should be observable, namely the oxygen incorporation into the Fe:STO thin film and a temperature increase caused by the irradiation. At the current stage, they can hardly be separated since they take place on the same time scale. Assumedly, the heating took place only in the first one or two minutes after the UV LED was turned on, consequently after this first period and before the linear decline the change in the resonance frequency is contributed to the mass gain due to oxygen incorporation into the Fe:STO thin film.

To determine the mass loss, the frequencies before and after illumination are taken into calculation and not the frequency difference during illumination. The change in N_2 atmosphere adds up to -0.91 Hz, which equals a reasonable mass gain of roughly 7 ng and an oxygen nonstoichiometry of 0.0076. This underlines the expectation of a mass change caused by UV light illumination. The frequency jump due to illumination (5.3 Hz) would result in a mass gain of 39 ng, which is physically not probable.

In O_2 atmosphere, see Figure 4.3-20 (b), the frequency drops 2 Hz, gaining almost 16 ng, more than twice as much as in N_2 does. The resulting δ amounts to 0.0042. This finding can be explained by the abundance of oxygen in the atmosphere: more oxygen, more incorporation in respect to the N_2 measurement. This is the case, when the incorporation is surface-limited.

The sharp frequency change before and after illumination is reproducible and has occurred during every illumination step (in the measurement depicted Figure 4.3-21, it also occurs) with thin films upon. Up to this point of the work, its origin is still unclear and will therefore not be further discussed.

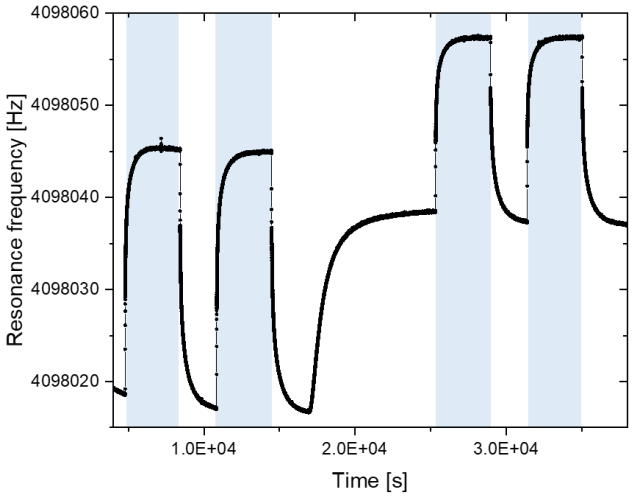

Figure 4.3-21 Results of the illumination experiments at temperatures of 360 and 370 °C in pure N_2 atmosphere. The UV light illumination leads to a higher frequency gain than the temperature increase by 10 °C.

In Figure 4.3-21, typical frequency measurements at lower temperature, roughly 360 to 370 °C, in pure N_2 atmosphere are displayed. In this experiment, the temperature was increased after the second illumination cycle by 10 °C to compare the frequency change caused by heating with the change due to UV light.

Apparently, the temperature step causes a gain of roughly 20 Hz, while the UV light causes a jump of about 28 Hz. Consequently, either the UV light heats the sample up more than expected or the oxygen exchange of the thin film with the surrounding atmosphere (light effect) is the reason for the discrepancy.

An argument against the frequency gain due to the light effect is that the additional jump of about 7 Hz can hardly be caused by an oxygen release, because this would correspond to a mass loss of approximately 50 ng. This beyond the possible range.

When turning the UV light on, the frequency jumps up. This stands in contrast to the measurements at higher temperatures, see Figure 4.3-20, where the frequency drops by 10 Hz. Consequently, the frequency change during illumination, and its direction, is temperature-dependent.

In this experiment, the sharp increase at the beginning and decrease at the end of the illumination were also present, however, they are hard to recognize in Figure 4.3-21.

As in the previous measurement in N_2, the frequency drops about 1 Hz after illumination compared to before. This corresponds to a reasonable mass gain of about 7.5 ng and a δ of about 0.0073, possibly caused by increased oxygen incorporation into the thin film. If the frequency jump were deducted from the value during UV light illumination, it would result in an obtained mass loss of ~200 ng (27 Hz, first illumination).

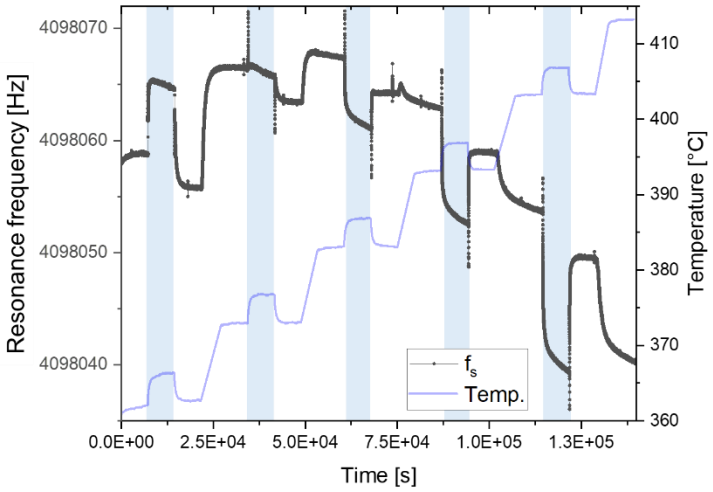

Figure 4.3-22 Results of the light illumination measurement with temperature steps. It was conducted at temperatures from 360 to 415 °C in 20 %O_2 atmosphere. As expected due to the previous experiments, the frequency response to UV light illumination differs at different temperatures.

In the experiment depicted in Figure 4.3-22, a temperature program was applied, with one UV light illumination at each temperature. The temperatures ranged from 360 to 415 °C in a gas atmosphere consisting of 80 % N_2 and 20 % O_2.

In accordance with the previous experiments, the resonance frequency increases at low temperatures when turning the light on, as seen at 360 °C. At temperatures above 370 °C, the illumination leads to a decrease in frequency. The tilting point seems to be at around 375 °C. Thus, the frequency behavior during illumination seems to be dependent on the measurement temperature.

At the temperature step between 380 and 390 °C, the frequency does not change gravely in contrast to the other temperature steps. Since at the steps before the frequency increases and after the frequency decreases, this can be considered the “temperature tilting point”. This is also reproducible and can be found in other experiments.

Independently from temperature, a sharp, reproducible increase when turning the light on, and decrease, respectively, when turning the light off occurs, as seen in the previous illumination experiments.

Interestingly, the frequency jumps of this experiment (deducted from the values before and after UV illumination) are all a factor 2.7 to 4 times higher than in all the previous measurements conducted on this sample, if the mass change is deducted from the values before and after turning off the UV light. The obtained values are summarized in Table 4.3-4.

Table 4.3-4 Results of the light illumination experiment from Figure 4.3-22 summarized.

Cycle	Δf [Hz]	Δm [ng]	Percentage of filled vacancies [%]	δ [10^{-3}]	Temperature [°C]
1	-2.98	22.0	79.1	2.09	361
2	-2.78	20.5	73.8	2.62	373
3	-3.34	24.6	88.7	1.13	383
4	-3.95	29.1	104.9	-0.49	393
5	-4.12	30.4	109.4	-0.94	403

Each illumination step leads to a frequency loss of 2.7 Hz or greater. The frequency changes are therefore too pronounced to just origin from an oxygen exchange reaction, but are probably caused by another temperature (and/or photovoltaic) effect (at the Pt|Fe:STO interface). If the change were just caused by a chemical reaction, more than 100 % of the oxygen vacancies would be filled due to irradiation at temperatures of 393 and 403 °C. This is physically not probable.

4.3.4.3. Conclusion of the light illumination experiments

To sum up, the light illumination experiments delivered results that were challenging to interpret.

- Contrarily to the gas exchange experiments or the conductivity experiments from Section 4.1., an increased oxygen incorporation, thus mass gain, could not be reasonably determined.
- The results of the measurement curves were reproducible at given temperature and gas atmosphere.
- The gas atmosphere does affect the course of the curve during light illumination on a larger scale. After illumination, the frequency seems to drop by a larger amount in pure O_2 atmosphere than in pure N_2 atmosphere, compare Figure 4.3-20. Arguably, this is caused by different oxygen content in the atmosphere.
- The shape of the curve during light illumination is temperature dependent, and seems to “tilt” in given temperature range. The experiment from Figure 4.3-22 stands exemplarily for that: from a frequency gain of 7 Hz at 360 °C to a frequency loss of ~15 Hz at 400 °C or put otherwise from a mass loss to a mass gain in this temperature interval.
- The first conducted experiments delivered physically reasonable results for the oxygen nonstoichiometry δ in the range of 0.007 to 0.004. The results of the experiment depicted in Figure 4.3-22 lead to mainly unreasonable results.
- The sharp frequency increase at the beginning and the end of each illumination could be observed at every microbalance with a thin film upon. The reason is yet still unclear.

5. Summary and Outlook

In all three segments of this thesis, oxygen nonstoichiometry plays the major role in the change of the properties of the investigated materials.

1. In-plane conductivity of STO single crystals

In this thesis, it could be shown that UV light illumination of STO single crystals causes an increase of the in-plane conductivity by three orders of magnitude, independent from deposited top layers. This change mainly originates from increased oxygen incorporation due to UV light illumination. Photovoltaic and temperature effects only play a negligible role. The relaxation behavior is crucially influenced by the oxygen partial pressure of the surrounding atmosphere. The lower the $p(O_2)$, the faster the conductivity relaxes to the initial value. Apart from that, a $1*10^{-3}$ S cm^{-1} (+/- half order of magnitude) threshold in conductivity could be observed during the illumination of the samples, almost independent from the deposited top layer and gas atmosphere. The investigated thin films, however, primarily influenced the relaxation behavior, which can be quantified by the τ value.

These findings could be used in future to further investigate the complex mechanism of the oxygen exchange reaction and thus, be useful in the application of strontium titanate, in SOFCs, SOPECs and other energy conversion systems.

2. Solid oxide photoelectrochemical cells

Solid oxide photoelectrochemical cells consisting of YSZ single crystals, (Fe:)STO thin films and Au or Pt current collectors exhibit well-defined, characteristic voltages, which, as literature [17, 18] also suggests, exhibit certain dependencies on temperature, oxygen partial pressure of the surrounding atmosphere, illumination time and current collector material.

Such investigated SOPEC systems seem to be promising in terms of generation of electric power by sunlight, if further investigations lead to enhanced photo and/or battery voltages. Different combinations of thin films, such as differently doped strontium titanate (Nb, Al) or LSCr, and current collector materials (Au, Pt, LSC) appeared to be promising candidates in these initial measurements. At the moment, their full potential is examined in the framework of the “Harvestore” project, which is a European project for the development of beyond-state-of-the-art technologies in the field of Internet of Things [57].

3. Monitoring oxygen nonstoichiometry *via* microbalance

By minimizing the temperature-, gas flow- and gas atmosphere-dependent frequency drift, the $GaPO_4$ setup could be improved. On top of that, it could be demonstrated that by changing the $p(O_2)$ of the surrounding atmosphere, the mass change of the oxygen exchange reaction of certain ceramic thin films could be monitored by $GaPO_4$ microbalances. Hence, the oxygen nonstoichiometry of such ceramic thin films can be determined by this method. In contrast to that, the enhanced oxygen incorporation due to UV light into strontium titanates [15] cannot be reasonably traced by $GaPO_4$ microbalances yet.

These results might help in finding ways to further optimize the microbalance setup to investigate the nonstoichiometry of different ceramic thin films or other chemical changes that result in a mass change in the ng range. However, this way to gravimetrically detect oxygen incorporation during UV light illumination has to be improved significantly, since $GaPO_4$ microbalances cannot be used for this purpose at the moment.

6. Danksagung

Nun geht auch dieses lange Kapitel zu Ende. Es war ein harter, steiniger Weg voller Höhen und Tiefen. Umso mehr ist es an der Zeit, meine Dankbarkeit auszudrücken.

Zuallererst will ich Prof. Jürgen Fleig, der mir die Möglichkeit gegeben hat, in dieser Arbeitsgruppe meine Diplomarbeit zu verfassen, meinen Dank aussprechen. Zu ganz besonderem Dank bin ich meinem Betreuer, Alexander Viernstein, verpflichtet, der immer beispiellos engagiert und hilfsbereit war, und nicht nur sachlich, sondern auch menschlich immer eine sehr wichtige Stütze im Verfassen meiner Diplomarbeit darstellte. Darüber hinaus, will ich natürlich der gesamten Arbeitsgruppe für eine tolle Zeit und sehr angenehme, reibungslose Zusammenarbeit danken.

Neben den letzten Semestern, die ich meiner Diplomarbeit gewidmet habe, habe ich im Verlauf des gesamten Studiums einige großartige Menschen kennengelernt, die mir sehr ans Herz gewachsen sind. Daher gilt mein Dank auch Andi, Cletzi, Timi, Anna, Martina und Vroni, sowie den Mitgliedern des Büros, Gerhard, Niklas und Georg, die vor allem zu Zeiten des Verfassens der Diplomarbeit eine große emotionale Unterstützung waren.

Zu guter Letzt, will ich mich bei meiner Familie bedanken und da vor allem meinen Eltern, Wolfgang und Maria, die mir das Studium überhaupt ermöglicht haben, und mir immer, wenn möglich, den Rücken freigehalten und gestärkt haben, auch wenn das aufgrund meiner vielen Eigenheiten auch nicht immer leicht war.

Bibliography

1. Kojima, A., K. Teshima, Y. Shirai, and T. Miyasaka, *Organometal halide perovskites as visible-light sensitizers for photovoltaic cells.* Journal of the American Chemical Society, 2009. **131**(17): p. 6050-6051.
2. Singhal, S.C., *Advances in solid oxide fuel cell technology.* Solid State Ionics, 2000. **135**(1-4): p. 305-313.
3. Shao, Z., W. Yang, Y. Cong, H. Dong, J. Tong, and G. Xiong, *Investigation of the permeation behavior and stability of a $Ba_{0.5}Sr_{0.5}Co_{0.8}Fe_{0.2}O_{3-\delta}$ oxygen membrane.* Journal of Membrane Science, 2000. **172**(1-2): p. 177-188.
4. Bouwmeester, H.J., *Dense ceramic membranes for methane conversion.* Catalysis today, 2003. **82**(1-4): p. 141-150.
5. Menesklou, W., H.-J. Schreiner, K.H. Härdtl, and E. Ivers-Tiffée, *High temperature oxygen sensors based on doped $SrTiO_3$.* Sensors and Actuators B: Chemical, 1999. **59**(2-3): p. 184-189.
6. Merkle, R. and J. Maier, *How is oxygen incorporated into oxides? A comprehensive kinetic study of a simple solid-state reaction with $SrTiO_3$ as a model material.* Angew Chem Int Ed Engl, 2008. **47**(21): p. 3874-94.
7. Moos, R., W. Menesklou, and K.H. Härdtl, *Hall mobility of undoped n-type conducting strontium titanate single crystals between 19 K and 1373 K.* Applied Physics A, 1995. **61**(4): p. 389-395.
8. Denk, I., W. Münch, and J. Maier, *Partial conductivities in $SrTiO_3$: bulk polarization experiments, oxygen concentration cell measurements, and defect-chemical modeling.* Journal of the American Ceramic Society, 1995. **78**(12): p. 3265-3272.
9. Drahus, M.D., P. Jakes, E. Erdem, and R.-A. Eichel, *Defect structure of the mixed ionic–electronic conducting Sr [Ti, Fe] Ox solid-solution system—Change in iron oxidation states and defect complexation.* Solid State Ionics, 2011. **184**(1): p. 47-51.
10. Steinsvik, S., R. Bugge, J. Gjönnes, J. Taftö, and T. Norby, *The defect structufe of $SrTi_{1-x}Fe_xO_{3-y}$ (x= 0–0.8) investigated by electrical conductivity measurements and electron energy loss spectroscopy (EELS).* Journal of Physics and Chemistry of Solids, 1997. **58**(6): p. 969-976.
11. Tilley, R.J., *Defects in solids*. Vol. 4. 2008: John Wiley & Sons.
12. Merkle, R. and J. Maier, *Oxygen incorporation into Fe-doped $SrTiO_3$: Mechanistic interpretation of the surface reaction.* Physical Chemistry Chemical Physics, 2002. **4**(17): p. 4140-4148.
13. Choi, G.M. and H.L. Tuller, *Defect Structure and Electrical Properties of Single-Crystal $Ba_{0.03}Sr_{0.97}TiO_3$.* Journal of the American Ceramic Society, 1988. **71**(4): p. 201-205.
14. Ye, X., J. Melas-Kyriazi, Z.A. Feng, N.A. Melosh, and W.C. Chueh, *A semiconductor/mixed ion and electron conductor heterojunction for elevated-temperature water splitting.* Physical Chemistry Chemical Physics, 2013. **15**(37): p. 15459-15469.
15. Merkle, R., R.A. De Souza, and J. Maier, *Optically Tuning the Rate of Stoichiometry Changes: Surface-Controlled Oxygen Incorporation into Oxides under UV Irradiation.* Angewandte Chemie International Edition, 2001. **40**(11): p. 2126-2129.
16. Viernstein, A., M. Kubicek, M. Morgenbesser, G. Walch, G.C. Brunauer, and J. Fleig, *High-Temperature Photochromism of Fe-Doped $SrTiO_3$ Caused by UV-Induced Bulk Stoichiometry Changes.* Advanced Functional Materials, 2019. **29**(23): p. 1900196.
17. Walch, G., B. Rotter, G.C. Brunauer, E. Esmaeili, A.K. Opitz, M. Kubicek, J. Summhammer, K. Ponweiser, and J. Fleig, *A solid oxide photoelectrochemical cell with UV light-driven oxygen storage in mixed conducting electrodes.* J Mater Chem A Mater, 2017. **5**(4): p. 1637-1649.
18. Brunauer, G.C., B. Rotter, G. Walch, E. Esmaeili, A.K. Opitz, K. Ponweiser, J. Summhammer, and J. Fleig, *UV-Light-Driven Oxygen Pumping in a High-Temperature Solid Oxide Photoelectrochemical Cell.* Advanced Functional Materials, 2016. **26**(1): p. 120-128.

19. Fritze, H., *High-temperature bulk acoustic wave sensors.* Measurement Science and Technology, 2011. **22**(1): p. 1-26.
20. Sauerbrey, G., *Verwendung von Schwingquarzen zur Wägung dünner Schichten und zur Mikrowägung.* Zeitschrift für Physik, 1959. **155**(2): p. 206-222.
21. Schröder, S., H. Fritze, S. Bishop, D. Chen, and H.L. Tuller, *Thin-film nano-thermogravimetry applied to praseodymium-cerium oxide films at high temperatures.* Applied Physics Letters, 2018. **112**(21): p. 213502.
22. Hammond, C., *The basics of cristallography and diffraction*. Vol. 214. 2001: Oxford.
23. Kröger, F. and H. Vink, *Relations between the concentrations of imperfections in crystalline solids*, in *Solid state physics*. 1956, Elsevier. p. 307-435.
24. Bruce, P.G., *Solid state electrochemistry*. Vol. 5. 1997: Cambridge university press.
25. Sze, S.M. and K.K. Ng, *Physics of semiconductor devices*. 2006: John Wiley & Sons.
26. De Souza, R., *Oxygen diffusion in $SrTiO_3$ and related perovskite oxides.* Advanced Functional Materials, 2015. **25**(40): p. 6326-6342.
27. Hensling, F.V.E., D.J. Keeble, J. Zhu, S. Brose, C. Xu, F. Gunkel, S. Danylyuk, S.S. Nonnenmann, W. Egger, and R. Dittmann, *UV radiation enhanced oxygen vacancy formation caused by the PLD plasma plume.* Sci Rep, 2018. **8**(1): p. 8846.
28. Tarun, M.C., F.A. Selim, and M.D. McCluskey, *Persistent photoconductivity in strontium titanate.* Physical Review Letters, 2013. **111**(18): p. 187403.
29. Baker, J.N., P.C. Bowes, D.M. Long, A. Moballegh, J.S. Harris, E.C. Dickey, and D.L. Irving, *Defect mechanisms of coloration in Fe-doped $SrTiO_3$ from first principles.* Applied Physics Letters, 2017. **110**(12): p. 122903-1 - 122903-5.
30. Van Benthem, K., C. Elsässer, and R. French, *Bulk electronic structure of $SrTiO_3$: Experiment and theory.* Journal of applied physics, 2001. **90**(12): p. 6156-6164.
31. Balachandran, U. and N. Eror, *Electrical conductivity in strontium titanate.* Journal of Solid State Chemistry, 1981. **39**(3): p. 351-359.
32. Chan, N.H., R. Sharma, and D.M. Smyth, *Nonstoichiometry in $SrTiO_3$.* Journal of the Electrochemical Society, 1981. **128**(8): p. 1762.
33. Sitte, W., E. Bucher, A. Benisek, and W. Preis, *Oxygen nonstoichiometry and ionic transport properties of $La_{0.4}Sr_{0.6}CoO_{3-\delta}$.* Spectrochimica Acta Part A: Molecular and Biomolecular Spectroscopy, 2001. **57**(10): p. 2071-2076.
34. Xiao, W., *Photovoltaic power system: modeling, design, and control*. 2017: John Wiley & Sons.
35. Jin, K.X., Y.F. Li, Z.L. Wang, H.Y. Peng, W.N. Lin, A.K.K. Kyaw, Y.L. Jin, K.J. Jin, X.W. Sun, C. Soci, and T. Wu, *Tunable photovoltaic effect and solar cell performance of self-doped perovskite $SrTiO_3$.* AIP Advances, 2012. **2**(4): p. 042131.
36. Nowotny, J., M.A. Alim, T. Bak, M.A. Idris, M. Ionescu, K. Prince, M.Z. Sahdan, K. Sopian, M.A.M. Teridi, and W. Sigmund, *Defect chemistry and defect engineering of TiO_2-based semiconductors for solar energy conversion.* Chemical Society Reviews, 2015. **44**(23): p. 8424-8442.
37. Eliaz, N. and E. Gileadi, *Physical Electrochemistry: Fundamentals, Techniques, and Applications*. 2019: John Wiley & Sons.
38. Elam, J. and M. Pellin, *$GaPO_4$ sensors for gravimetric monitoring during atomic layer deposition at high temperatures.* Analytical Chemistry, 2005. **77**(11): p. 3531-3535.
39. Reiter, C., P.W. Krempl, H. Thanner, W. Wallnöfer, and P.M. Worsch. *Material properties of $GaPO_4$ and their relevance for applications*. in *Annales de chimie science des matériaux*. 2001. Elsevier.
40. Thanner, H., P. Krempl, W. Wallnöfer, and P. Worsch, *$GaPO_4$ high temperature crystal microbalance with zero temperature coefficient.* Vacuum, 2002. **67**(3-4): p. 687-691.

41. Krempl, P., G. Schleinzer, and W. Wallnöfer, *Gallium phosphate, $GaPO_4$: a new piezoelectric crystal material for high-temperature sensorics.* Sensors and Actuators A: Physical, 1997. **61**(1-3): p. 361-363.
42. Sasaki, K. and J. Maier, *Low-temperature defect chemistry of oxides. I. General aspects and numerical calculations.* Journal of Applied Physics, 1999. **86**(10): p. 5422-5433.
43. GmbH, P.A.S., *High Temperature Microbalance Resonator (R-30).* 2019.
44. Fleig, J., R. Merkle, and J. Maier, *The $p(O_2)$ dependence of oxygen surface coverage and exchange current density of mixed conducting oxide electrodes: model considerations.* Phys Chem Chem Phys, 2007. **9**(21): p. 2713-23.
45. Yamakata, A., J.J.M. Vequizo, and M. Kawaguchi, *Behavior and Energy State of Photogenerated Charge Carriers in Single-Crystalline and Polycrystalline Powder $SrTiO_3$ Studied by Time-Resolved Absorption Spectroscopy in the Visible to Mid-Infrared Region.* The Journal of Physical Chemistry C, 2015. **119**(4): p. 1880-1885.
46. Fergus, J.W., *Lanthanum chromite-based materials for solid oxide fuel cell interconnects.* Solid State Ionics, 2004. **171**(1-2): p. 1-15.
47. Akashi, T., T. Maruyama, and T. Goto, *Transport of lanthanum ion and hole in $LaCrO_3$ determined by electrical conductivity measurements.* Solid State Ionics, 2003. **164**(3-4): p. 177-183.
48. Meadowcroft, D., *Some properties of strontium-doped lanthanum chromite.* Journal of Physics D: Applied Physics, 1969. **2**(9): p. 1225.
49. Yang, Y.-J., T.-L. Wen, H. Tu, D.-Q. Wang, and J. Yang, *Characteristics of lanthanum strontium chromite prepared by glycine nitrate process.* Solid State Ionics, 2000. **135**(1-4): p. 475-479.
50. Kawada, T., N. Sakai, H. Yokokawa, and M. Dokiya, *Electrical properties of transition-metal-doped YSZ.* Solid State Ionics, 1992. **53**: p. 418-425.
51. Koide, H., Y. Someya, T. Yoshida, and T. Maruyama, *Properties of Ni/YSZ cermet as anode for SOFC.* Solid State Ionics, 2000. **132**(3-4): p. 253-260.
52. Nicoloso, N., A. Löbert, and B. Leibold, *Optical absorption studies of tetragonal and cubic thin-film yttria-stabilized zirconia.* Sensors and Actuators B: Chemical, 1992. **8**(3): p. 253-256.
53. Badar, N., N.F. Chayed, R. Roshidah, N. Kamarudin, and N. Kamarulzaman. *Band gap energies of magnesium oxide nanomaterials synthesized by the sol-gel method*. in *Advanced Materials Research*. 2012. Trans Tech Publ.
54. Petrov, A., V. Cherepanov, O. Kononchuk, and L.Y. Gavrilova, *Oxygen Nonstoichiometry of $La_{1-x}Sr_xCoO_{3-\delta}$ ($0< x\leq 0.6$).* Journal of Solid State Chemistry, 1990. **87**(1): p. 69-76.
55. Mizusaki, J., Y. Mima, S. Yamauchi, K. Fueki, and H. Tagawa, *Nonstoichiometry of the perovskite-type oxides $La_{1-x}Sr_xCoO_{3-\delta}$.* Journal of Solid State Chemistry, 1989. **80**(1): p. 102-111.
56. Sitte, W., E. Bucher, and W. Preis, *Nonstoichiometry and transport properties of strontium-substituted lanthanum cobaltites.* Solid State Ionics, 2002. **154**: p. 517-522.
57. Harvestore. *Harvestore*. 2020; Available from: http://www.harvestore.eu/.